

Snow Depth on Arctic Sea Ice from Microwave Radiometers

Philip Rostosky

Supervisor: Dr. Gunnar Spreen

Prof. Dr. Monika Rhein

Institute of Environmental Physics

University of Bremen

This dissertation is submitted for the degree of

Doctor of natural Science

09.07.2020

Für meine Freundin und meine Familie

Declaration

I hereby declare that except where specific reference is made to the work of others, the contents of this dissertation are original and have not been submitted in whole or in part for consideration for any other degree or qualification in this, or any other university. This dissertation is my own work and contains nothing which is the outcome of work done in collaboration with others, except as specified in the text and Acknowledgements.

Philip Rostosky

09.07.2020

Acknowledgements

First of all, I would like to thank my supervisor Dr. Gunnar Spreen for his continuous support and excellent guidance throughout my whole time at the institute. Gunnar always had time to discuss newest results and gave helpful advice for problems occurring during my work. Furthermore, I would like to thank Prof. Dr. Monika Rhein, the second reviewer of my thesis, for her time and interest in my work.

I would like to thank all members of the "Remote Sensing of Polar Regions" group for all the helpful discussions and for the nice, enjoyable working climate. Special thanks go to Dr. Marcus Huntemann who shared his expertise in microwave emission modelling, to Dr. Christian Melsheimer with whom I had many fruitful discussions about various topics and to my former office mates and friends Valentin Ludvig and Dmitrii Murashkin for the nice time in the office.

I wish to express my gratitude to the members of my PhD committee, namely Dr. Sebastian Gerland, Dr. Christian Melsheimer, Dr. Annette Rinke and Dr. Gunnar Spreen, for their support and valuable comments and suggestions on my work. Special thanks go to Dr. Sebastian Gerland for his excellent support during my research stay at the Norwegian Polar Institute. In this context, I also want to thank the ERASMUS+ program for the financial support during the research stay.

I would like to thank Dr. Mario Mech for the two very intense training days on the atmospheric radiative transfer model PAMTRA, Dr. Polona Itkin and Dr. Anja Rösel for their support during my research stay in Norway and Dr. Nander Wever for the help with the snow evolution model SNOWPACK.

I want to thank the German Research Foundation (DFG) for funding this PhD position within the ArctiC Amplification: Climate Relevant Atmospheric and SurfaCe Processes, and Feedback Mechanisms (AC)³ project. In this context, I also want to express my gratitude to all organisers and members of the (AC)³ community for the great time during the project meetings and various workshops.

Emphatic thanks go to Dr. Georg Heygster, Dr. Christian Melsheimer, Valentin Ludvig and Dr. Raul Scarlat for proofreading my PhD thesis.

Last but not least, I want to thank my family, friends and life partner Ulrike Ullrich for their support and care during my PhD project.

Abstract

Snow depth on Arctic sea ice is a key parameter for understanding the Arctic climate system and yet, snow is only poorly implemented in state of the art climate models and an evaluation of the models remains difficult due to the lack of ground truth data.

So far, no routine method exist to monitor the snow depth on Arctic sea ice on a daily, Arctic-wide basis. Observations from passive microwave satellite sensors are independent of daylight and almost transparent to clouds and it has been shown that they can be used to estimate the snow depth on sea ice.

In this thesis, a new, empirical passive microwave snow depth retrieval is developed using an extensive set of airborne snow depth observations as training data. It could be shown that extending the retrieval to low frequency channels, it is, for the first time, possible to retrieve pan-Arctic snow depth during spring.

The uncertainty of the new retrieval was estimated using a Monte-Carlo approach based on state of the art microwave emission models for the snow-ice system and the atmosphere and an extensive set of in-situ snow-, ice and atmospheric measurements. The estimated uncertainty increases with increasing snow depth and is between 4 cm to 8 cm over first-year ice and 5 cm to 9 cm over multiyear ice.

An evaluation of the new retrieval showed that it performs well in most Arctic regions in spring and, compared to three other satellite snow depth retrievals, has the lowest RMSD to in-situ snow depth measurements. An exception is Atlantic sector of the Arctic for the year 2015, where strong flooding occurred and all retrievals strongly underestimate the measured snow depth. Comparing the retrieval with the results from SNOWPACK simulations showed that the retrieval is more sensitive to snowfall under warm than under cold conditions. This is due to stronger snow metamorphism under warm conditions leading to enhanced microwave scattering.

Table of contents

1	Introduction	1
1.1	The Arctic Climate System	1
1.2	Snow Depth on Arctic Sea Ice Retrievals	3
2	Theoretical Background	7
2.1	Planck's Law	7
2.2	Radiative Transfer	8
2.3	Microwave Properties of Snow	11
2.4	Applications of the Theory	19
2.5	Error Discussion	23
3	A New Snow Depth on Arctic Sea Ice Retrieval	27
3.1	Data	28
3.1.1	Satellite Data	28
3.1.2	Operation IceBrigde Snow Depth Measurements	28
3.1.3	Ice Type	29
3.1.4	Reanalysis Data	30
3.2	Regression Analysis	31
3.3	Uncertainty Estimation	37
3.4	Evaluation	39
3.4.1	Evaluation with SLF Measurements	39
3.4.2	Timeseries Analysis	42
3.5	Discussion	49
3.6	Conclusions	53
4	Uncertainty Estimation	57
4.1	Data and Models	58
4.1.1	N-ICE2015 data	58

4.1.2	Microwave Emission Model of Layered Snowpacks	60
4.1.3	The SNOWPACK Model	61
4.1.4	The PAMTRA Model	62
4.2	Results	63
4.2.1	Influence of the Ice Properties	63
4.2.2	Influence of the Atmosphere	66
4.2.3	Influence of the Snow Properties	67
4.3	Uncertainty of Potential Snow Depth Retrievals	72
4.4	Application to the AMSR-E/2 Snow Depth Retrieval	76
4.5	Conclusions	78
5	Evaluation and Inter-comparison of Existing Snow Depth on Arctic Sea Ice Retrievals	81
5.1	Satellite Retrievals	81
5.2	Evaluation with In-situ Data	83
5.3	Seasonal Cycle	92
5.4	Sensitivity to Snow Evolution	98
5.5	Discussion	108
5.6	Conclusions	109
6	Conclusions and Outlook	111
6.1	Conclusions	111
6.2	Outlook	115
	References	117
	Appendix A Gaussian Error Propagation	129
	Appendix B N-ICE2015 Snow Pit Data	131
	Appendix C SNOWPACK Initialisation Files	145
	Appendix D Snow Depth Dataset	149
	Appendix E Satellite Data	151

Chapter 1

Introduction

In recent decades, an enhanced Arctic climate change was observed and the Arctic air temperature has increased twice as much as on global average. This phenomena is called Arctic amplification (Serreze and Barry, 2011). It is linked with a strong decline in Arctic sea ice cover (Perovich et al., 2017a). In 2016, the German Research Council (Deutsche Forschungsgesellschaft, DFG) started the Transregional research centre ArctiC Amplification: Climate Relevant Atmospheric and SurfaCe Processes, and Feedback Mechanisms (AC)³ with the aim to improve the understanding of the rapid climate change in the Arctic. This thesis is part of the (AC)³ project with the aim to develop a new snow depth on Arctic sea ice retrieval from satellite observations which can be used to analyse the seasonal and inter-annual variability of snow depth and to evaluate snow depth simulations from coupled climate models. Parts of the content presented here are based on two published articles in peer reviewed journals. Parts of chapter 3 are published in Rostosky et al. (2018) and parts of chapter 4 are published in Rostosky et al. (2020). The study presented in chapter 5 exists as a paper draft, but has not been submitted by the time the thesis was written. Two "snow depth on Arctic sea ice datasets" were published (Rostosky et al., 2019a,b, see Appendix D). In addition to the two first-author publications, two co-author articles were published (Fritzner et al., 2019; Zhou et al., 2020) where the newly derived snow depth product was used to assimilated a coupled climate model (Fritzner et al., 2019) and inter compared with other existing snow depth retrievals (Zhou et al., 2020). These results are not included here.

1.1 The Arctic Climate System

In recent years, an enhanced increase in the tropospheric temperature in the Arctic was observed (Serreze and Barry, 2011). As a result of the rapid warming, a strong decline in the Arctic sea ice extend and sea ice thickness was observed in the last decades (Kumar et al.,

2010; Serreze et al., 2009). This decline is especially pronounced during the summer months when the sea ice extent reaches its minimum. From 1979 to 2016, the September sea ice extent has declined by -13.3% (Perovich et al., 2017b) and record minima occurred in 2007 and 2012.

Estimating the decline in sea ice thickness is difficult since long timeseries are only available from climate models which still have difficulties in accurately model Arctic sea ice parameters (Holmes et al., 2019; Turner et al., 2013). Maslowsky et al. (2012) found a decline in Arctic sea ice thickness of 44% from 1979 and 2002 based on model simulations. Arctic-wide sea ice thickness retrievals from satellites based on sea ice freeboard observations from ICESat and CryoSat-2 exist since 2003 (Ricker et al., 2014). Kwok and Rothrock (2009) compared ICESat derived sea ice thickness data from 2003 to 2008 with submarine ice thickness measurements (1958 to 2000) and found a decrease in the mean winter ice thickness of 1.75 m between 1980 and 2008. Laxon et al. (2013) compared sea ice thickness observations from CryoSat-2 (2010-2012) with sea ice thickness estimates from ICESat (2003-2008) and found a decline in autumn sea ice volume by 4291 km³.

State of the art coupled Arctic climate models have difficulties to reproduce the strong decline in sea ice extent (Kumar et al., 2010), revealing a gap in the representation and understanding of physical processes that are responsible for the rapid decline in Arctic sea ice cover (Turner et al., 2013).

Snow on Arctic sea ice is an important contributor to many of these processes. In comparison to the thermal conductivity of sea ice (~ 2 W/m; Trodahl et al., 2001), snow can have a very low thermal conductivity (0.2 W/m to 2 W/m; depending on the snow type; Riche and Schneebeli, 2013) and therefore, even a shallow snow layer strongly influences ocean-sea ice-atmosphere heat fluxes. This has a direct impact on the sea ice thickness. During winter, when the air temperature is low, snow dampens the negative heat flux to the ice and thus slows down the sea ice growth. During summer, this effect reverses since the snow now isolates the sea ice from the warm air and therefore slows down the ice melt. The albedo of snow is between 0.7 for melting snow and 0.9 for dry snow (Perovich et al., 2002), which is very high compared to the albedo of the open ocean (0.06) and therefore, snow strongly influences the Arctic energy budget. Wrong estimates of snow depth on Arctic sea ice from climate models directly impact the accuracy of the modelled sea ice thickness and surface energy fluxes (Castro-Morales et al., 2014).

Information about snow depth and density are important for sea ice thickness retrievals based on satellite altimetry. Kern et al. (2015) concluded that unknown snow depth and density are the major sources of uncertainties in ice thickness retrievals. In addition, snow is only poorly represented in climate models and consequently, the models fail to reproduce the

snow depth on Arctic sea ice distribution derived from airborne snow depth measurements (Castro-Morales et al., 2017a). Webster et al. (2018) concluded that in order to improve the representation of snow on sea ice in coupled climate models, it is crucial to have Arctic-wide snow depth observations with constrained uncertainties. A strong correlation between snow depth and under-ice light fields has been found (Arndt et al., 2017), the latter being important for biological and biochemical processes in the upper ocean, highlighting the interdisciplinary importance of snow on sea ice.

Due to the lack of consistent, long timeseries of snow depth on Arctic sea ice, estimating long term trends in Arctic snow depth is difficult. A comparison of the Warren climatology (W99) from 1954 to 1991 (Warren et al., 1999) to recent airborne snow depth measurements from the Operation IceBridge (OIB) campaign showed similar mean snow depths over multiyear ice (MYI, ice that survived at least one summer melt) but an, on average, 16.5 cm lower snow depth over first-year ice (FYI, ice that has formed since the last freeze up) (Kurtz and Farrell, 2011). Webster et al. (2014) analysed spring snow depth from airborne measurements, ice mass buoys and the W99 climatology and found a negative trend in spring snow depth of -0.29 cm/year from 1950 to 2013 which the authors linked to a decrease in the length of the accumulation period of snow due to a later onset of freezing and an earlier onset of melting in the recent years. A similar thinning of the Arctic snowpack was also observed in reconstructed snow depth data based on atmospheric reanalysis data (Blanchard-Wrigglesworth et al., 2018). However, no final conclusions about possible trends in snow depth can be drawn due to the limited spatial coverage of the W99 climatology and OIB snow depth observations and high uncertainties in reanalysis snowfall products (Boisvert et al., 2018).

1.2 Snow Depth on Arctic Sea Ice Retrievals

In principle, different methods exist to obtain snow depth on Arctic sea ice. However, so far, no routine method exists to derive estimates of snow depth on Arctic sea ice on a daily basis for the whole Arctic ocean. Existing products are limited to retrieve snow depth over FYI (Comiso et al., 2003). In-situ measurements of snow depth on sea ice are rare and most of them are obtained at the end of the winter season since field observations require daylight conditions. Drifting buoys may cover a whole winter season but their snow depth measurements are only representative for a small area around the buoy and are mainly located over MYI (e.g., Perovich and Richter-Menge, 2015).

Due to the spatial sampling of in-situ surveys, observations may not be representative of basin-wide conditions and airborne or satellite observations pose an opportunity to overcome this challenge (e.g., King et al., 2015). Airborne snow depth measurements as e.g., from the OIB campaign (Kurtz et al., 2013b) may cover hundreds to a thousand kilometres (although captured in one-dimensional, along-track profiles; Kurtz and Farrell, 2011) but are time- and cost-intensive and limited by weather conditions.

Given the vast area and temporal resolution requirements, satellites are, potentially, the best tool to derive snow depth estimates on an Arctic-wide scale with daily or weekly coverage. For snow on land, several snow retrievals from different satellite sensors have been developed in recent decades. They include passive microwave satellite retrievals of snow depth or snow water equivalent (e.g., Chang et al., 1987; Che et al., 2008; Josberger and Mognard, 2002; Pulliainen, 2006) and snow depth retrievals using interferometry (Leinss et al., 2015) or synthetic aperture radar observations (König et al., 2001). However, on sea ice, many of those retrievals are of limited use. For example, snow depth retrievals from interferometry are limited to landfast ice, since sea ice drift and its movement due to waves will cause errors. Guerreiro et al. (2016) developed an algorithm to retrieve snow depth on Arctic sea ice based on satellite altimetry from the CryoSat-2 and SARAL/AltiKa missions. Their results show a good agreement with OIB snow depth measurements but the area covered by the retrieval is limited to observations below 81.5°N , missing the central Arctic, due to the inclination of the SARAL/AltiKa orbit. Lawrence et al. (2018) further improved the method of Guerreiro et al. (2016) by calibrating the freeboard derived from SARAL/AltiKa and from CryoSat-2 to OIB freeboard observations. Zhou et al. (2018) combined measurements from CryoSat-2 and from the Soil Moisture and Ocean Salinity (SMOS) sensor to derive snow depth information. Maaß et al. (2013) developed a snow depth retrieval algorithm for sea ice based on passive microwave observations at 1.4 GHz from SMOS and found a reasonable agreement with OIB snow depth measurements. However, the product is limited to areas where the ice is thicker than 1–1.5 m, thereby restricting its field of use to mainly MYI. Based on backscatter observations at Ku-Band and C-Band, Yackel et al. (2019) presented a method to derive late winter to spring snow depth on landfast FYI.

The first snow depth on sea ice retrieval from passive microwave satellite observations was developed by Markus and Cavalieri (1998) and is based on the gradient ratio (GR) of vertically polarised brightness temperature observations at 19 GHz and 37 GHz. The retrieval was developed using an empirically derived linear fit between microwave satellite observations and Antarctic snow depth observations. The regression coefficients were updated to the latest passive microwave satellites (Comiso et al., 2003). However, the same regression coefficients were applied in the derivation of snow depth on Arctic sea ice. In a recent study, Brucker and

Markus (2013) reviewed the initial retrieval for the Arctic and concluded that it is necessary to derive new regression coefficients for the retrieval.

Currently, the retrieval is limited to dry snow, i.e. winter, and snow depths below 50 cm. At microwave frequencies (e.g., 19 GHz and 37 GHz) MYI influences the brightness temperatures in a similar way as snow (Comiso et al., 2003) and thus the retrieval is limited to FYI which is a concern, since a substantial area of the Arctic is covered by MYI. It has been shown that the retrieval performs worse over rough sea ice (e.g., Markus et al., 2006a; Stroeve et al., 2006).

In recent years, following the approach of Markus and Cavalieri (1998), several studies have been published on improving passive microwave snow depth retrievals using better training data (e.g., OIB snow depth observations) or more sophisticated methods (e.g., a neural-network). Rostosky et al. (2018) incorporated observations at lower frequency (i.e., 6.9 GHz) and showed that the addition of this frequency enables the retrieval of snow depth over MYI in spring. This retrieval is further presented in chapter 3. Kilic et al. (2019) trained a multilinear regression model using brightness temperatures at 7 GHz, 19 GHz and 37 GHz, and OIB snow depth observations. Braakmann-Folgmann and Donlon (2019) developed a neural network algorithm using the gradient ratio at GR(19/7), GR(37/19) (see equation 3.1) and the polarisation ratio PR(37) (see equation 3.2) as input data. The network was trained with OIB snow depth measurements. Liu et al. (2019) trained a deep neural-network to retrieve Arctic wide snow depth from brightness temperature observations.

Most of the newly derived retrievals are trained or evaluated with OIB snow depth observations (e.g., Braakmann-Folgmann and Donlon, 2019; Guerreiro et al., 2016; Kilic et al., 2019; Lawrence et al., 2018; Maaß et al., 2013; Shi et al., 2020). The OIB campaign is limited to spring and most of the measurements are obtained over sea ice in the Beaufort Sea, north of the Canadian Archipelago and in the central Arctic. Since snow- and ice conditions can vary in different Arctic regions and change in the course of the winter season (Willmes et al., 2014), it remains unclear, how well these snow depth on Arctic sea ice retrievals perform outside of the spatial and temporal coverage of their training data. Several studies investigated the performance of passive microwave snow depth retrievals (Brucker and Markus, 2013; Kern and Ozsoy, 2019; Markus et al., 2011; Rostosky et al., 2018; Worby et al., 2008), and concluded that further improvements of the retrieval algorithms are required. So far, no method exists to obtain the snow density or grain type from satellite observations, even though they are crucial for the Arctic energy budget (Webster et al., 2018). Besides satellite based snow depth retrievals, other methods to obtain Arctic-wide snow depth estimates are based on reanalysis data. In principle, reanalysis products provide information about snowfall which then can be converted into snow depth on sea ice. However, different reanalysis models

use different empirical parametrizations for the phase of the precipitation (i.e., whether the precipitation falls in liquid or solid form) and thus the estimated snowfall largely differs within different reanalysis products (Boisvert et al., 2018; Lindsay et al., 2013). In addition, assumptions have to be made about snow loss into leads or due to blowing events.

The most comprehensive models which use reanalysis data to derive pan-Arctic snow depth on sea ice are the NASA Eulerian Snow Model (NESOSIM; Petty et al., 2018) and the Distribution Snow-Evolution Model (SNowModel; Liston et al., 2018). Both models account for sea ice drift. In addition, parameterisations and tuning parameters for snow redistribution, snow loss into open water and wind packing are used in the models. Both models use a simplified snowpack without a detailed description of the snow-grain properties.

A more detailed snow model which uses reanalysis data and, in addition, simulates the whole snow- and sea ice system including physical-based snow metamorphism is the recently developed SNOWPACK model (Wever et al., 2019). SNOWPACK is a one-dimensional model and the simulations are cost expensive due to the detailed snow microphysics in the model.

The aim of this thesis is to develop a new passive microwave snow depth on Arctic sea ice product which can be used to evaluate seasonal and inter-annual variability in Arctic snow depth and which is suitable to be used for the evaluation of coupled climate models. This document is organised as following. In the second chapter, an overview of the theoretical background of microwave remote sensing of snow depth on Arctic sea ice is given. In the third chapter, a new passive microwave satellite snow depth on Arctic sea ice retrieval is developed, followed by a detailed uncertainty estimation of the retrieval in chapter four. In chapter five, the new snow depth retrieval is evaluated and compared to other passive microwave snow depth on Arctic sea ice retrievals. The document closes with a conclusion and outlook in chapter six.

Chapter 2

Theoretical Background

In this chapter, the theoretical background for passive microwave satellite observations of snow depth on Arctic sea ice is derived. In this thesis, satellite observations from the AMSR-E and AMSR2 sensors at different microwave frequencies are used (see Appendix E). This chapter is organised as follows. In the sections 2.1 and 2.2, basic theoretical concepts used in passive microwave remote sensing are derived and in section 2.3, these concepts are applied to passive microwave observations of snow. In section 2.4, simulations of the microwave emission of snow relevant for remote sensing are performed. These simulations are based on the theory derived above. In section 2.5, possible errors due to the simplifications used in the theoretical models are discussed.

2.1 Planck's Law

In this section, a comprehensive overview of the most important concepts used in microwave remote sensing is given closely following the theory described in Ulaby and Long (2014a,b). Passive microwave satellites measure the natural emission of the earth at top of the atmosphere. Planck's blackbody law is a fundamental concept in microwave remote sensing since it can be used to describe the thermal emission of a material (i.e., the earth surface).

$$B_f = \frac{2hf^3}{c^2} \frac{1}{\exp\left\{\frac{hf}{kT}\right\} - 1} \quad (2.1)$$

A blackbody is a theoretical material that absorbs all incoming radiation and thus reflects no radiation. In equation 2.1, B_f describes the spectral radiance ($\text{Wm}^{-2}\text{sr}^{-1}\text{Hz}^{-1}$) of a blackbody. h is Planck's constant ($6.63 \cdot 10^{-34}$ J), f the frequency (Hz), T the temperature (K), c the velocity of light ($\approx 3 \cdot 10^8$ ms^{-1}) and k the Boltzmann constant ($1.38 \cdot 10^{-23}$ JK^{-1}).

$\exp\{\}$ is the exponential function. In the microwave regime (low-frequency regime), Planck's law can be simplified using the following approximation:

$$\frac{hf}{kT} \ll 1 \quad (2.2)$$

In this case, the term in the exponential function of equation 2.1 is close to zero and using the approximation that $\exp(x)-1 \approx x$, for small x Planck's law can be simplified to the so called Rayleigh-Jeans approximation:

$$B_f = \frac{2kT}{\lambda^2} \quad (2.3)$$

Perfect absorbers do not exist in nature. Real materials (also called grey bodies) emit less than a blackbody and a part of the incoming radiation might be reflected at the surface. For grey bodies, the Rayleigh-Jeans approximation can be rewritten as in equation 2.4 where the physical temperature is replaced with the brightness temperature T_b .

$$B = \frac{2kT_b}{\lambda^2} \quad (2.4)$$

The brightness temperature of the material is linked to its physical temperature via the emissivity e :

$$T_b = eT \quad (2.5)$$

The emissivity is between 0 and 1 and thus the brightness temperature of a material is always smaller than or equal to its physical temperature. In general, e depends on the frequency and polarisation. The brightness temperature is directly linked to the power measured by satellite antennas (Ulaby and Long, 2014a) and thus is a fundamental quantity in microwave remote sensing.

2.2 Radiative Transfer

To derive information about surface properties from the brightness temperatures observed by satellites, the radiative transfer equation has to be solved. An antenna, deployed on a satellite system, receives radiation from several sources within the antenna's field of view. The received radiation is a mixture of the radiation emitted by the surface, radiation that might be scattered by the surface into the direction of the antenna and upward emission of the atmosphere. Similar to the definition of the brightness temperature (see equation 2.4), an apparent radiometric temperature distribution T_{AP} can be defined which relates the signal the

antenna receives to the radiation within its field of view (Ulaby and Long, 2014a, chapter2).

$$B_i = \frac{2kT_{AP}}{\lambda^2} \quad (2.6)$$

Here B_i is the incident brightness with respect to the antenna field of view. The derivation of the radiative transfer equation given below closely follows the description in Ulaby and Long (2014a) and Mätzler (2006).

The radiative transfer equation can be derived by integrating the differential form equation 2.6 (i.e., $dB/d\vec{r}$) along the path \vec{r} the radiation travels until it reaches the measuring antenna. In principle, the radiative transfer equation describes how radiation is modified when propagating through a medium (assuming incoherent interactions; Ulaby and Long, 2014a). Radiation may be modified due to absorption, emission and scattering within the medium. In addition, for a non-homogeneous medium, reflection may occur at the different interfaces (e.g., at the ice-snow and snow-atmosphere interfaces).

First, let's define absorption, scattering, emission and reflection. If a wave travels through a medium, it may lose energy due to absorption or scattering. In the case of absorption, the energy of the wave is transformed into heat and in the case of scattering, energy is scattered away outside the field of view of the measuring device. Absorption and scattering can be combined into extinction:

$$\gamma_e = \gamma_a + \gamma_s \quad (2.7)$$

Here, γ_e is the extinction coefficient and γ_a and γ_s are the absorption and scattering coefficients, respectively. The change in brightness B of the wave along the path r due to extinction can be expressed by:

$$dB_{ext} = -\gamma_e B dr. \quad (2.8)$$

Emission leads to an increase in energy and can be caused by thermal emission of the medium or by energy that is scattered into the travelling direction of the wave. Emission can be introduced as following:

$$\text{emission} = \gamma_a J_a + \gamma_s J_s \quad (2.9)$$

Since thermal equilibrium is assumed, emission has to be equal to absorption and J_a and J_s are the source functions for the emitted and scattered energy.

Similar to the extinction the change of brightness due to emission can be defined as:

$$dB_{emit} = \gamma_e [(1 - a)J_a + aJ_s]. \quad (2.10)$$

Here, a is the so called single scattering albedo with $a = \frac{\gamma_s}{\gamma_e}$.

Reflection at interfaces occurs due to differences in the refractive indices of the medium a wave travels through. It can be described with the complex Fresnel equations for r_v , the reflection at vertical polarisation (equation 2.11) and r_h , the reflection at horizontal polarisation:

$$r_v = \frac{n_2 \cos \theta_1 - n_1 \sqrt{n_2^2 - n_1^2 \sin^2 \theta_1}}{n_2 \cos \theta_1 + n_1 \sqrt{n_2^2 - n_1^2 \sin^2 \theta_1}} \quad (2.11)$$

$$r_h = \frac{n_1 \cos \theta_1 - n_2 \sqrt{n_2^2 - n_1^2 \sin^2 \theta_1}}{n_1 \cos \theta_1 + n_2 \sqrt{n_2^2 - n_1^2 \sin^2 \theta_1}} \quad (2.12)$$

Here, n_1 and n_2 are the complex refractive indices of medium 1 and medium 2 and θ_1 the incident angle of the incoming wave. Here, Snell's law ($n_1 \sin \theta_1 = n_2 \sin \theta_2$) was used to relate the reflection angle θ_2 to θ_1 .

The general form of the radiative transfer equation can be then written as in (for a detailed derivation, see Ulaby and Long, 2014a):

$$T_{AP}(r) = T_{AP}(0) \exp\{-\tau(0, r)\} + \int_0^r \gamma_e(r') [(1 - a(r))T(r') + a(r)T_{SC}(r')] \exp\{-\tau(r', r)\} dr' \quad (2.13)$$

In equation 2.13, T_{AP} is the apparent temperature (see equation 2.6) at point \vec{r} . $\exp\{-\tau(0, r)\}$ is the extinction of radiation along the path $(0, r)$ with τ being the optical thickness of the medium:

$$\tau(0, r) = \int_0^r \gamma_e(r') dr' \quad (2.14)$$

The integral term in equation 2.13 describes the change in radiation due to absorption ($(1 - a(r))T(r')$) and scattering ($a(r)T_{SC}(r')$) with $a(r)$ being the single scattering albedo and T_{SC} the temperature, which is scattered into the antenna's field of view. The equation is based on the approximation that for an infinitesimal thin layer thickness dr' , it can be assumed that the medium is in thermal equilibrium and therefore Kirchoff's law can be applied.

Solving the radiative transfer equation for the general case is highly complex due to the nature of the integral. The solution at point r_1 in a medium generally depends on interactions between all other points in the medium. In the next section, solutions of the radiative transfer equation with respect to remote sensing of snow are discussed.

2.3 Microwave Properties of Snow

Snow is a granular medium consisting of roughly 70% air and 30% ice. A natural snow cover often consists of several layers with different physical properties. It has been shown that models for describing the microwave emission of snow can be derived from the radiative transfer equation (Mätzler, 1987). In order to derive methods to estimate the microwave emission of snow, several assumptions have to be made. In the following, it is assumed that the snowpack can be divided into several sub-layers and that each layer is isotropic. The interface between the single layers is a radiometrically smooth surface (i.e., the roughness of the interface is much smaller than the wavelength of interest) and the single layers are thick enough so that coherent effects can be neglected. In Section 2.5, possible errors due to these simplifications are discussed.

Dielectric Properties of Snow

Dielectric properties of snow strongly influence its microwave emission and are thus fundamental for the remote sensing of snow on sea ice. In general, the dielectric constant ϵ of a material (also called permittivity) is a complex number, i.e., $\epsilon = \epsilon' - i\epsilon''$ (hereafter ϵ'' is understood as an imaginary number and the notation i is dropped). A valid approximation for snow is that the real part of the dielectric constant can be related to volume scattering while the imaginary part of the dielectric constant can be associated with absorption (Mätzler, 1987). In Mätzler (2006), a detailed review of the dielectric properties of snow is given and the concepts described below closely follow the theory described there.

The real part of the permittivity of snow depends on the snow density (i.e., on the volume fraction of ice) and the shape of the snow grains. Snow is a granular medium consisting of a host material with dielectric constant ϵ_e (air) and an inclusion material with dielectric constant ϵ_i (ice) and therefore, mixing theory can be used to describe the real part of snow permittivity (Mätzler, 2006).

Using mixing theory, the permittivity of snow can be calculated from the following equation:

$$\epsilon = \epsilon_e + \frac{f(\epsilon_i - \epsilon_e) \sum_{k=1}^3 \epsilon_a / (\epsilon_a + A_k(\epsilon_i - \epsilon_e))}{3 - f(\epsilon_i - \epsilon_e) \sum_{k=1}^3 A_k / (\epsilon_a + A_k(\epsilon_i - \epsilon_e))} \quad (2.15)$$

Here, f is the ice volume fraction and A_k the depolarisation factor for the three dimensions with $A_1 + A_2 + A_3 = 1$. ϵ_a is the apparent permittivity, i.e., the permittivity in the surroundings of the grains. From experimental studies, the Polder Van Santen model was found to be the best description of ϵ_a (Mätzler, 2006). In this case, $\epsilon_a = 1 - A_k$.

Snow grains can have various shapes ranging from spheroidal particles to plates depending

on the state of snow metamorphism and thus, estimating the depolarisation factor A_k can be highly complex. Under the assumption of spheroidal grains (i.e., $A_1 = A_2 \equiv A$), only one shape parameter has to be determined. In Mätzler (2006), an empirical model to estimate A is presented, which is based on permittivity measurements over various snow types giving A as a function of ice volume fraction:

$$A = \begin{cases} 0.1 + 0.5f & 0 < f \leq 0.32, \\ 0.18 * \exp\{-10(f - 0.32)\} & 0.32 < f < 0.5 \\ 0.33 & f \geq 0.5 \end{cases} \quad (2.16)$$

Equation 2.16 shows an empirical function to determine A , based on the ice volume fraction f . The range between $0 < f \leq 0.32$ describes the initial snow metamorphism from fresh snow ($f \approx 0.1$) with oblate snow flakes to wind slab snow with nearly spherical grains. In this step, A increases with f . For $0.32 < f < 0.5$, A drops which is related to an increased connection between single snow grains once snow metamorphism continues. For $f > 0.5$, the medium is assumed to be ice with spherical air inclusions and for those, $A = 1/3$.

In his formulation of the Improved Born Approximation, Mätzler (1998) showed that the following approximation for ε'' can be used:

$$\varepsilon'' = \sqrt{\varepsilon'} K^2 f \varepsilon_i'' \quad (2.17)$$

In equation 2.17, K^2 is the mean squared ratio of the electrical field of the particles (≈ 0.5 for dry snow). ε_i'' can be computed from equation 2.15 inserting $\varepsilon_i = \varepsilon_i' + \varepsilon_i''$.

Figure 2.1 shows the real (left) and imaginary (right) part of the snow permittivity as a function of the ice volume fraction calculated from equation 2.15 and equation 2.17. Both, ε' and ε'' increase with f . In snow, ε' is about two to three orders of magnitude larger than ε'' . Therefore, dry snow can be called a weakly absorbing medium and thus, microwaves can travel long distances through snow before their energy gets absorbed (this, however, is only true if volume scattering is neglected). The permittivity of wet snow is higher than for dry snow due to the high permittivity of water ($\varepsilon' > 35$; Stiles and Ulaby, 1980).

In principle, wet snow can be considered a mixture of dry snow and water inclusions and thus equation 2.15 can be used (Mätzler, 2006) by substituting f with the volume fraction of liquid water W , ε_i with ε_w (dielectric constant of water) and ε_e with ε_d (dielectric constant of dry snow). A_k now refers to the shape parameter of the water inclusions.

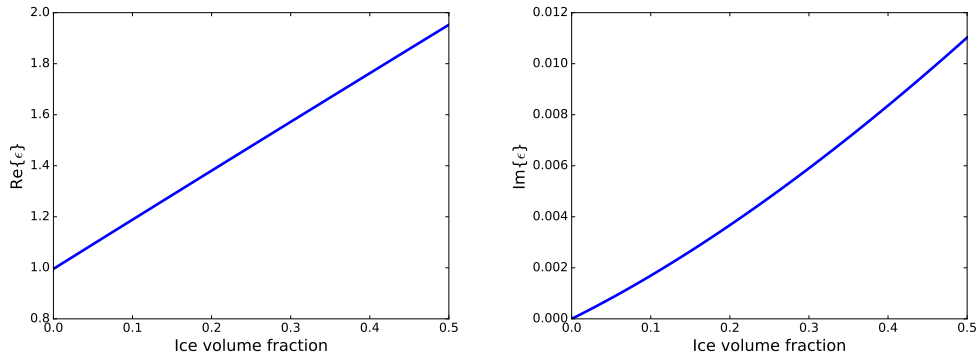


Figure 2.1: Real (left) and imaginary (right) part of the complex dielectric constant of snow as a function of the ice volume fraction. Note the different orders of magnitude.

So far, no analytical model exists that describes how the water droplets are arranged within the snow (Mätzler, 2006). Based on a comparison with measurement data, it was found that the shape parameters: $A_1 = A_2 = 0.4975$ and $A_3 = 0.005$ results in the best fit to the measurements (Mätzler, 2006).

Figure 2.2 shows the absorption coefficient γ_a for dry (left) and wet (right) snow for microwave frequencies at 6.9 GHz, 18.7 GHz and 36.5 GHz. γ_a is generally controlled by ϵ'' and it was calculated using equations 24 and 28 from Mätzler (1998) assuming spherical snow grains. For dry snow (Figure 2.2, left), the absorption coefficient increases with increasing ice volume fraction and is higher for higher frequencies. In Figure 2.2 (right) an ice volume fraction of 0.38 (corresponding to a snow density of $\approx 350 \text{ kgm}^{-3}$) is used.

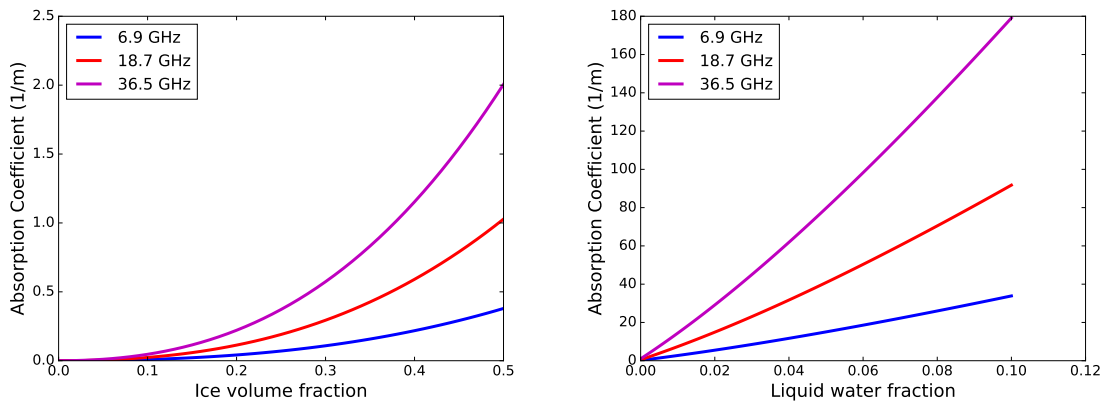


Figure 2.2: Left: Absorption coefficient for dry snow for microwaves at 6.9 GHz, 18.7 GHz and 36.5 GHz as a function of the ice volume fraction. Right: Absorption coefficient for wet snow for microwaves at 6.9 GHz, 18.7 GHz and 36.5 GHz as a function of the liquid water content. Note the different orders of magnitude.

With increasing liquid water fraction, the absorption coefficient of snow strongly increases for all frequencies. At a liquid water fraction of 0.1, the absorption coefficient is already more than two orders of magnitude higher than in the case of dry snow.

Volume Scattering in Snow

Because of the low absorption, microwaves can travel several decimeters to meters (depending on the frequency) through snow. In this case, volume scattering at snow grains can have a strong effect. In the case of wet snow, the absorptivity strongly increases (see Figure 2.2) and thus, volume scattering can usually be neglected. This, however, is not the case for cold, dry snow at microwave frequencies above 10 GHz (Mätzler, 2006). The most common approaches to describe volume scattering of microwaves are the so called strong fluctuation theory (SFT) and the dense media radiative transfer theory (DMRT) (Mätzler, 1998). Both theories lead to highly complex equations and thus, approximations have to be applied in order to obtain a practical description of the volume scattering in snow (Löwe and Picard, 2015).

Based on these theories, two microwave emission models have been developed in recent years. The DMRT model (Picard et al., 2013) and the microwave emission model of layered snowpacks (MEMLS; Wiesmann and Mätzler, 1999), which is based on the SFT theory. Recently Picard et al. (2018) developed the model framework SMRT in which both theories can be applied. MEMLS is used for various studies within this thesis and therefore, the theoretical concepts used in MEMLS are described here in some detail. By reformulating the model equations, Löwe and Picard (2015) have shown that the theory of both models can be transferred to the other model and that the resulting volume scattering described by these models only differs by a small factor.

A common approximation of the SFT is the so called Born approximation. In the Born approximation, the medium is treated as a weakly scattering medium which means that its dielectric function can be written as $\varepsilon(r) = \varepsilon_a + \varepsilon_f(r)$. ε_a is the average dielectric constant of the medium and $\varepsilon_f(r)$ the fluctuation. In the Born approximation it is assumed that $\frac{\varepsilon_f(r)}{\varepsilon_a} \ll 1$. In the following, the scattering coefficient in the Born approximation is derived, closely following the derivation proposed in Mätzer (1987).

Lets assume an incident plane wave which fulfils equation:

$$\vec{E}_i(\vec{r}) = \vec{E}_0 \exp\{i\vec{k}_i\vec{r}\} \quad (2.18)$$

Here, k_i is the wave vector of the incident field and E_0 is the amplitude of the incident wave being perpendicular to k_i . If the wave is scattered by a particle with volume V , its scattering

amplitude f can be described by equation 2.19 (Mätzer, 1987).

$$f(\vec{k}_i, \vec{k}_s) = \frac{1}{4\pi E_0} \int_V \vec{k}_s \times [\vec{k}_s \times \vec{E}_s(\vec{r})] \delta(\vec{r}) \exp\{-i\vec{k}_s \vec{r}\} dV \quad (2.19)$$

Here, \vec{k}_s is the wave number of the scattered wave, and the $\delta(\vec{r})$ describes dielectric function of the medium (i.e., $\delta(\vec{r}) = \epsilon_a + \epsilon_f(r)$). $E_s(\vec{r})$ is the electric field in the scattering volume. Under the Born approximation, the electric field in the scattering volume is similar to the incident field and $E_s(\vec{r})$ can be approximated with equation 2.18. Equation 2.19 then simplifies to:

$$f(\vec{k}_i, \vec{k}_s) = -\frac{1}{4\pi} [\vec{k}_s \times [\vec{k}_s \times \frac{E_0}{|E_0|}]] \int_V \delta(\vec{r}) \exp\{-i[\vec{k}_a - \vec{k}_s] \vec{r}\} dV \quad (2.20)$$

The bistatic scattering coefficient γ_{ij}^{bi} can be calculated from equation 2.20 if the volume of the scatterer V and the dielectric function $\delta(\vec{r})$ are known. Instead of using $\delta(\vec{r})$, it is more practical to describe the dielectric function of the medium by an auto-correlation function $R(\vec{r}' - \vec{r}'')$ of the fluctuating permittivity. $\vec{r}' - \vec{r}''$ describes the three-dimensional lag distance of the fluctuating permittivity, i.e., in the case of snow, it is related to the minimum distance between two scatterers (snow grains). The advantage of using an auto-correlation function is that it represents a continuous function in a granular medium like snow. Also, single scattering events need to be averaged to obtain a representative description of the volume scattering in snow (Mätzer, 1987). Thus the average scattering coefficient is of more interest than single scattering events and it can be described by an auto-correlation function of the single scatterers:

$$R(\vec{r}' - \vec{r}'') = \frac{1}{V \langle \delta^2 \rangle} \langle \int_V \delta(\vec{r}') \delta(\vec{r}' - \vec{r}'') dV \rangle \quad (2.21)$$

Here, $\langle \rangle$ is the volume average of the quantity inside the brackets, δ^2 is the variance of the dielectric function of the medium.

From equation 2.20 and 2.21, the effective volume scattering coefficient of the Born approximation can be derived (see Mätzer, 1987, for a detailed derivation).

$$\gamma_{ij}^{bi} = \frac{k_0^4 |\langle \epsilon \rangle|^2 \langle \epsilon^2 \rangle d \sin^2(\chi)}{4\pi \cos \theta} \int_V R(\vec{r}' - \vec{r}'') \exp\{i(\vec{k}_i - \vec{k}_s) \cdot \vec{r}\} dV \quad (2.22)$$

In equation 2.22, γ_{ij}^{bi} is the effective volume scattering coefficient. K_0 is the vacuum wave number and χ the angle between E_0 and k_s d is the snow depth.

As discussed, the Born approximation plays a fundamental role in modelling the microwave emission of snow and the most advanced model (MEMLS) is based on this approach. The

auto-correlation function of a snowpack can be found from X-ray microtomography images (e.g., Krol and Löwe, 2016) These images are, however, costly to obtain and thus are only rarely measured during field campaigns. Therefore, it is more practical to approximate the auto-correlation function of snow by an exponential function (Mätzler, 1987):

$$R(\vec{r} - \vec{r}') = \exp\left\{-|\vec{r} - \vec{r}'|/p_c\right\} \quad (2.23)$$

Here, p_c is the exponential correlation length and this parameter controls the strength of the scattering in a snowpack. It is possible to estimate p_c from specific surface area (SSA) measurements (Mätzler, 2002).

In the case of snow, the assumption of a weakly scattering medium is not valid due to the large differences in the permittivity of air ($\epsilon' = 1$) and ice ($\epsilon' = 3.18$) and thus the Born approximation is not valid. However, Mätzler (1998) further improved the Born approximation (Improved Born Approximation; IBA in the following) for the application in snow. Based on the IBA one of the most comprehensive microwave emission model for layered snowpacks (MEMLS, Wiesmann and Mätzler, 1999) was developed.

The advantage of the IBA is, that most concepts of the classical Born approximation can still be used after some modifications. In the IBA, the electric field in the scattering volume is similar to equation 2.18, including a factor \vec{K} which relates the internal field in the scatterer to the electric field of the incident wave:

$$\vec{E}(\vec{r}) = \vec{K}\vec{E}_i(\vec{r}) \quad (2.24)$$

For small ellipsoidal scatterers, an analytical solution for \vec{K} can be found:

$$K_{ii} = \frac{\epsilon_a}{\epsilon_a + (\epsilon_e - \epsilon_i)A} \quad (2.25)$$

The effective scattering coefficient γ_{ij}^{bi} in the IBA can be calculated from equation 2.20 with the addition of the factor \vec{K} . An application of the IBA to a granular medium is given in Mätzler (1998). The author shows that in the IBA, the scattering coefficient γ_s (assuming spherical grains), which is the directional average of γ_{ij}^{bi} can be computed as:

$$\gamma_s = \frac{3p_c^3 k^4}{32} f(1-f) \left| \frac{(\epsilon_i - \epsilon_e)(2\epsilon_{eff} + \epsilon_e)}{2\epsilon_{eff} + \epsilon_i} \right|^2 \quad (2.26)$$

Here, ϵ_{eff} is the effective emissivity of snow which can be obtained from mixing theory (e.g., equation 2.15. with $\epsilon = \epsilon_{eff}$). k is the wave number and f the ice volume fraction. ϵ_e is the permittivity of the host (air) and ϵ_i the permittivity of the inclusion (ice).

Figure 2.3 shows the scattering coefficient at 6.9 GHz, 18.7 GHz and 36.5 GHz (which are the main frequencies used this thesis) calculated from equation 2.26 for a snowpack with a density of 250 kgm^{-3} (left) and 350 kgm^{-3} (right). The exponential correlation length p_c ranges from 0.05 mm to 0.2 mm which is the typical range found for different snow types (Mätzler, 2002). For all frequencies, the scattering coefficient increases with increasing p_c . Overall scattering is roughly one magnitude larger for 36.5 GHz compared to 18.7 GHz and 2 orders of magnitude larger compared to 6.9 GHz. And influence of the density on the strength of the scattering is only visible at 36.5 GHz. Here, the scattering is slightly higher in the dense snowpack (Figure 2.3, right). For the snowpack investigated here, the scattering coefficient is as large as the absorption coefficient when the exponential correlation length is around 0.14 mm.

Using the absorption and scattering coefficients, the penetration depth d can be calculated from equation 2.27 (Mätzler, 1987):

$$d = \frac{1}{\sqrt{\gamma_a \gamma_s}} \quad (2.27)$$

The penetration depth is a commonly used concept in microwave remote sensing (Ulaby and Long, 2014b) and it describes the depth at which the energy of microwaves has decayed to $1/e$ of its original energy due to extinction in the medium. In a weakly absorbing medium (e.g, dry snow), d is controlled by volume scattering while in a strongly absorbing medium (e.g, wet snow), d is controlled by absorption.

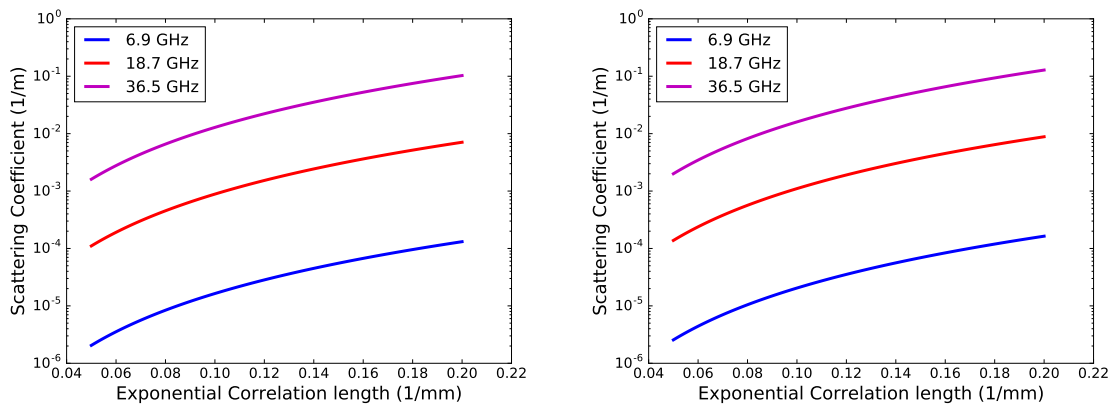


Figure 2.3: Scattering coefficient of snow as a function of the exponential correlation length for a snowpack with a density of 250 kgm^{-3} (left) and 350 kgm^{-3} (right).

Figure 2.4 shows the penetration depth for dry (left) and wet (right) snow for microwave frequencies at 6.9 GHz, 18.7 GHz and 36.5 GHz as a function of the exponential correlation length. The penetration depth decreases with increasing p_c due to an increased loss of energy through volume scattering. In the case of dry snow (Figure 2.4, left) the penetration depth at 6.9 GHz decreases from roughly 60 m for low p_c to about 20 m for high p_c . At 18.7 GHz, the penetration depth decreases from 10 m to 2 m and at 36.5 GHz it decreases from 2.5 m to 0.9 m. In wet snow (Figure 2.4, right), the penetration depth of the microwaves is strongly reduced to a few centimetres for 6.9 GHz and less than a cm for 36.5 GHz (here, a liquid water fraction of 0.1 was assumed). This has consequences for passive microwave based snow depth retrievals since for wet snow, no information about snow depth can be derived. Differences in the microwave emission of wet snow at different frequencies are then solely due to surface scattering.

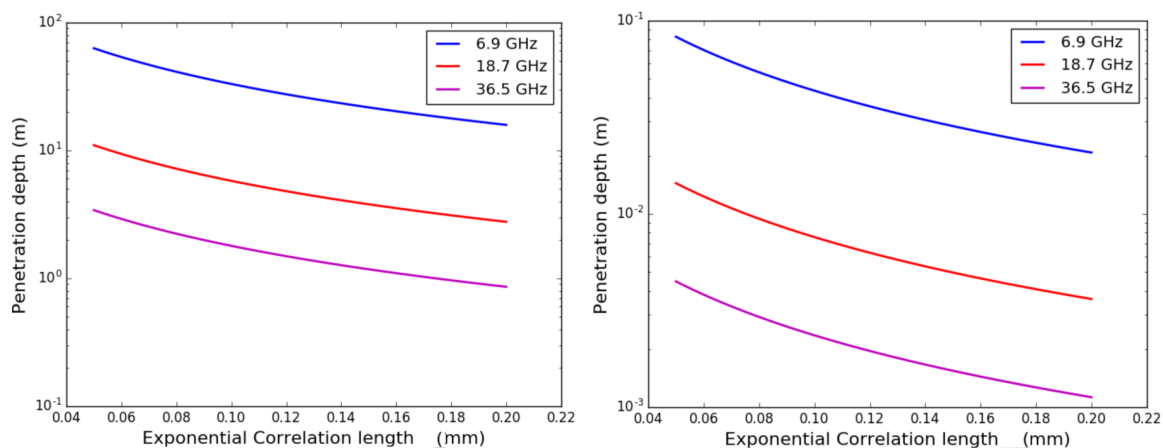


Figure 2.4: Penetration depth of microwaves at 6.9 GHz, 18.7 GHz and 36.5 GHz for dry (left) and wet (right) snow as a function of the exponential correlation length. Note the different orders of magnitude.

Reflection at Interfaces

A snowpack may consist of several layers with different refractive properties (i.e, different dielectric constants). In addition, reflection occurs at the snow-air interface due to the high contrast in the dielectric constants of air ($\epsilon = 1$) and snow ($\epsilon \approx 1.3$). In the case of a radiometrically smooth surface, reflection at each layer can be calculated from the Fresnel equations (see equations 2.11 and 2.12). Note that reflectivity (r) and emissivity (e) are linked via $r + e + t = 1$, where t is the transmissivity. For snow and air, the permeability is roughly one and can therefore be neglected. The refractive index n in equations 2.11 and 2.12 is then directly proportional to the square root of the dielectric constant.

In general, the reflectivity of snow is higher at horizontal polarisation than at vertical polarisation. For example, solving equations 2.11 and 2.12 for an incident wave with an incident angle of 50° and the dielectric constants for air and snow mentioned above, the reflectivity is 0.073 at vertical polarisation and 0.202 at horizontal polarisation. For a rough interface, reflection becomes diffuse leading to a depolarisation of the microwaves and the reflectivity at the snow-ice interface becomes lower.

So far, it has been assumed that the internal layers of the snowpack are thick enough so that coherent scattering can be neglected (this assumption is true if wavelength is less than half the layer thickness; Mätzler, 2006). In the case of e.g., thin ice layers in the snow, coherent scattering effects have to be considered. The reflection coefficient of layer $n, n-1$ can then be calculated in an iterative process (Mätzer, 1987):

$$r_n = \frac{F_n + r_{n-1} \exp\{2iP_n - 1\}}{1 + F_n r_{n-1} \exp\{2iP_n - 1\}} \quad (2.28)$$

In equation 2.28 r_n is the reflection coefficient of layer n , F_n the Fresnel reflection of the interface between layer $n-1$ and n . P_n is the phase of the wave from layer $n-1$. For a medium with low absorption (i.e., $\epsilon'' \ll \epsilon'$). P_n can be calculated using Snells law:

$$P_n = \frac{2\pi d}{\lambda_0} (n' \cos \theta'_n + in'' \cos \theta) \quad (2.29)$$

Here, d_n is the thickness of layer n and λ_0 the vacuum wavelength. n' and n'' are the real (n') and imaginary (n'') part of the complex refractive index.

2.4 Applications of the Theory

In this section, results for the microwave emission of snow based on the theory described above are presented. For simulating the microwave emission of snow, a sea ice version of MEMLS is used (Tonboe, 2005). This model is based on the IBA described in the section above. For absorption and refraction, solutions based on slightly different approximations are used in the model but the principal ideas behind these solutions are similar to the ones described above.

Figure 2.5 (left) shows the brightness temperature at three selected microwave frequencies (6.9 GHz, 18.7 GHz and 36.5 GHz) at vertical and horizontal polarisation as a function of the snow depth for a snowpack with a density of 250 kgm^{-3} and a temperature of 260 K. The exponential correlation length is set to 0.137 mm, which is the average correlation length for fragmented snow (Mätzler, 2002). The simulated brightness temperature at 6.9 GHz

barely changes with increasing snow depth for both polarisations since volume scattering is low at 6.9 GHz (see Figure 2.3). At 36.5 GHz, the influence of the snow depth is obvious. Unlike 6.9 GHz and 18.7 GHz, the brightness temperatures at 36.5 GHz shows a nonlinear dependency to the snow depth. The reason is that at 36.5 GHz, the signal saturates for deep snow due to the low penetration depth (see Figure 2.4; note that the penetration depth shown in Figure 2.4 is higher than in real snowpacks since reflection at the snow-air interface was neglected).

Overall, the influence of the snow depth is stronger at vertical polarisation. The results shown here highlight the possibility to relate passive microwave satellite observations to changes in the snow depth.

Figure 2.5 (right) shows the same as Figure 2.5 (left) but for the gradient ratio GR . The gradient ratio is the most common quantity used in passive microwave snow depth retrievals (e.g., Markus and Cavalieri, 1998; Rostosky et al., 2018) and is defined as following:

$$GR(T_{bv1}/T_{bv2}) = \frac{T_{bv1} - T_{bv2}}{T_{bv1} + T_{bv2}} \quad (2.30)$$

Here, $GR(T_{bv1}/T_{bv2})$ is the gradient ratio of brightness temperatures at frequencies ν_1 and ν_2 . The GR is used to minimise the influence of the physical temperature on the observations. A clear relation between all GR and the snow depth is visible in Figure 2.5 (right). The sensitivity of the GR to changes in snow depth is stronger at vertical polarisation and higher frequencies (i.e., $GR(37/19)$). However, $GR(37/19)$ shows a nonlinear dependency to snow deeper than 40 cm due to the saturation of the signal from T_{b37} (see Figure 2.5, left).

The strength of the scattering and thus the relation between GR and snow depth is strongly modified by the grain type within the snowpack. The most frequently occurring snow types for Arctic snow are described below.

Different snow types form under different environmental conditions. An overview of snow metamorphism is given in Colbeck (1986) and Sommerfeld and LaChapelle (1970). Colbeck (1986) describes four types of snow metamorphism: (i) metamorphism under small temperature gradients, (ii) metamorphism under high temperature gradients, (iii) wet snow metamorphism and (iv) surface-generated metamorphism.

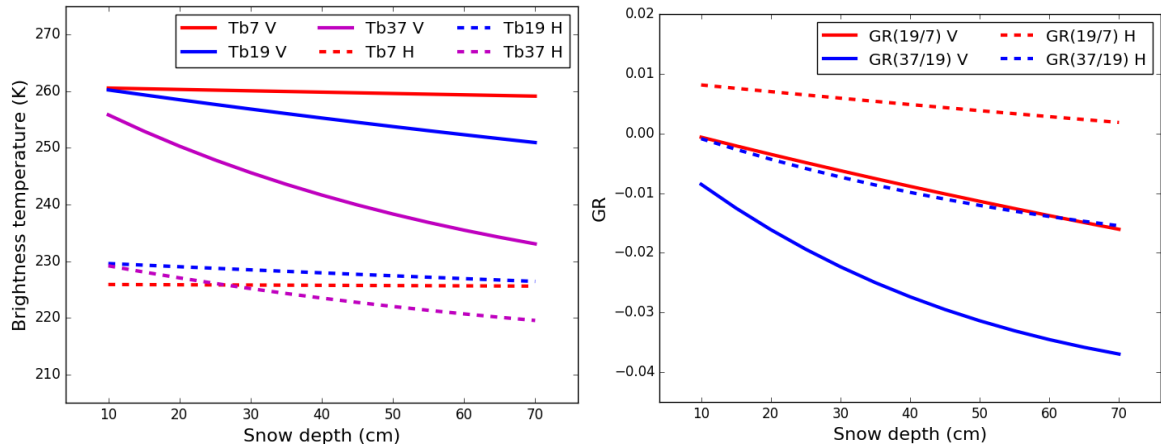


Figure 2.5: Simulated brightness temperature (left) and GR (right) for different snow depths over Arctic first-year ice.

(i) Under small temperature gradients (i.e., slow snow metamorphism), the snow transforms into large, rounded grains. This type of snow leads to strong volume scattering of microwaves (see table 1 in Mätzler, 2002).

(ii) Under high temperature gradients (i.e., rapid snow metamorphism), the transformation of snow grains is governed by surface kinetics and as a result, fragmented grains or depth hoar develop, the latter has large snow crystals resulting in enhanced microwave scattering (Wiesmann and Mätzler, 1999).

(iii) under wet conditions, snow metamorphism happens much faster than under dry conditions (e.g., Colbeck, 1986; Lehning et al., 2002b) and snow grains form large clusters of ice crystals. Once the snow refreezes (also called melt-refreeze events), it forms several mm thick ice layers which strongly influence the microwaves penetrating through the snow due to coherent scattering effects (Mätzer, 1987).

(iv) Under high wind conditions, so called wind slab can form with small, broken grain crystals. Wind slab snow has moderate scattering effects (see table 1 in Mätzler, 2002).

If the snow has not undergone metamorphism yet, it is called new snow. New snow has very small crystals and is almost transparent for microwaves (see table 1 in Mätzler, 2002). During the N-ICE2015 (Merkouriadi et al., 2017b) and SHEBA (Sturm et al., 2002) campaigns, new snow, wind slab snow, fragmented snow and depth hoar were the most observed snow types.

Figure 2.6 shows the dependency of the brightness temperatures at 6.9 GHz, 18.7 GHz and 36.5 GHz on different snow types for a 50 cm thick snowpack with a temperature of 260 K. At both polarisations, depth hoar (DH) has the strongest impact on the brightness temperature, especially at 18.7 GHz and 36.5 GHz. At vertical polarisation, $T_{b36.5}$ is strongly influenced by the snow types while $T_{b18.7}$ is only moderately influenced. At 6.9 GHz, only depth hoar

(DH) has a strong influence on the brightness temperature. At horizontal polarisation, a strong influence is only visible for strong scatterers like rounded grains (RG) or depth hoar (DH). Figure 2.6 (right) shows the same as Figure 2.6, (left) but for the GR . The influence of the snow type is stronger on $GR(37/19)$ than on $GR(19/7)$ for both polarisation. Real snowpacks often consists of several layers with a wind slab on top, fragmented snow in the middle and a layer of depth hoar at the bottom of the snowpack and thus are a mixture of the theoretical results presented here. These results show the importance of the snow grain type for passive microwave snow depth retrievals.

Figure 2.7 shows the sensitivity of the simulated brightness temperature (left) and GR (right) to the temperature gradient in the snowpack. Here, a linear temperature gradient is assumed such that the temperature at the snow-ice interface is always 260 K. Thus for a temperature gradient of -10 K, the temperature at top of the snowpack is 250 K. Differences in the brightness temperatures at different frequencies can be expected due to different penetration depths and thus a different temperature in the main emitting layers. However, overall, the sensitivity of the brightness temperatures or the GR s to changes in the temperature gradient are small compared to the influence of the snow grain type.

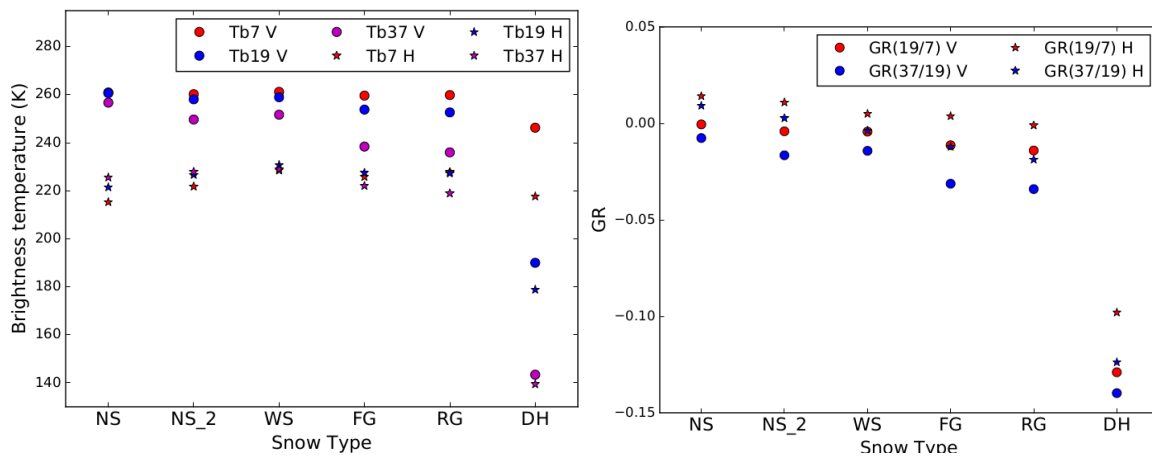


Figure 2.6: Simulated brightness temperature (left) and GR (right) for different snow types and microwave frequencies for a 50 cm deep snowpack over Arctic first-year ice. The snow types are: new snow (NS), nearly new snow (NS_2), wind slab (WS), fragmented snow (FG), rounded grains (RG) and depth hoar (DH).

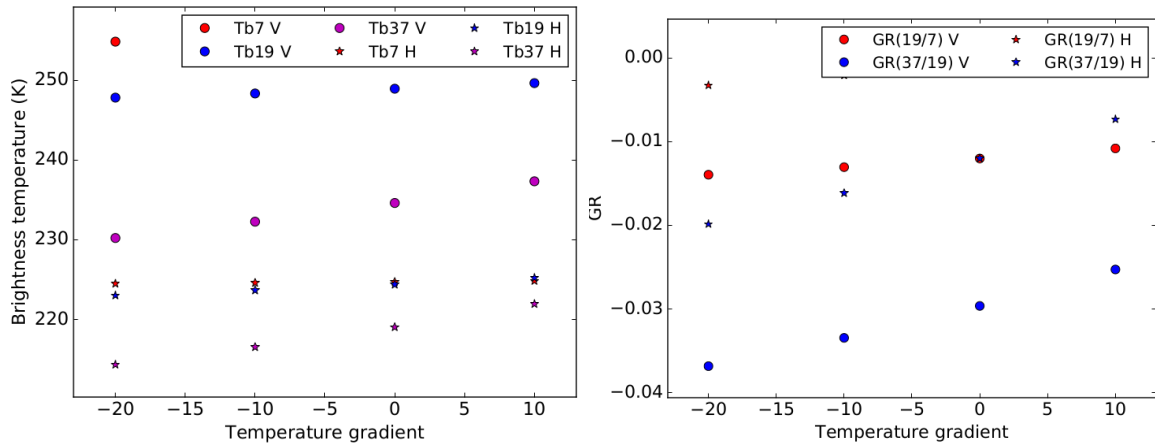


Figure 2.7: Simulated brightness temperature (left) and GR (right) for a 50 cm deep snowpack with different temperature gradients in the snow. Note the different scale compared to figure 2.6.

As described earlier, wet snow has highly different dielectric properties resulting in much higher absorption compared to dry snow (Figure 2.2). In fact, since water is almost opaque for microwaves, the relation between snow depth and brightness temperature diminishes if the snow becomes wet.

Figure 2.8 shows the simulated brightness temperatures (Figure 2.8, left) and GR (Figure 2.8, right) for a 50 cm deep snowpack with different liquid water content (LWC). Even a LWC of 0.1% strongly influences the simulated brightness temperatures at both polarisations. At a LWC of 1% the differences between the brightness temperatures at different frequencies are almost zero (Figure 2.8, left). As a consequence, the GR approaches zero (Figure 2.8, right). For the horizontal polarisation, a strong increase in brightness temperatures is found for a LWC of 10%. This increase is stronger for the lower frequencies and is associated with a strong increase of surface reflectivity due to an increase of the snow permittivity. These results show that potential snow depth retrievals from satellite microwave observations only work under dry snow conditions.

2.5 Error Discussion

In the theory described above, several simplifications were made. Since MEMLS is used for several studies in this thesis, it is important to discuss the potential errors in the model caused by these simplifications.

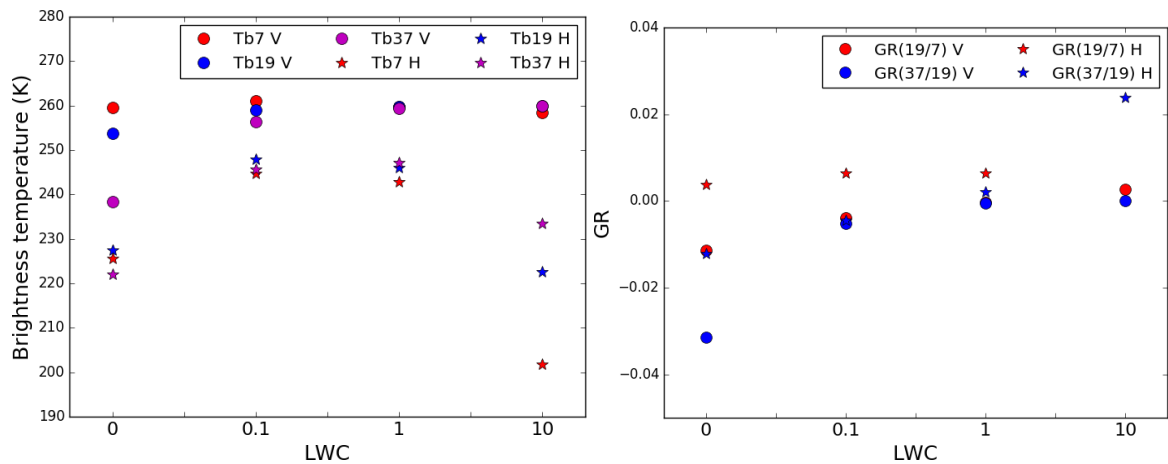


Figure 2.8: Simulated brightness temperatures (left) and GR (right) for a 50 cm deep snowpack with different liquid water contents.

So far, it was assumed that the snow is isotropic in each layer, which is not necessarily true for real snowpacks. Löwe et al. (2013) discussed the influence of the anisotropy in snow and concluded that the influence of anisotropy on the dielectric properties of snow is small. In order to describe the volume scattering in snow, an exponential length scale is used which is a zero order approximation of the auto-correlation function of the snow grains. Löwe et al. (2011) showed that under isothermal snow metamorphism, the use of a single length scale leads to inaccurate results. The authors suggest to add second order parameters (e.g., curvature) to improve the approximation. These parameters can, however, only be derived from tomographic measurements which are difficult and time-consuming to obtain and are thus rarely available from field campaigns. In the ongoing MOSAiC campaign, a large number of tomographic measurements are performed which can help to further develop a more complex theory.

In MEMLS, coherent reflection is not considered. While coherent reflection effects in snow can usually be neglected in the case of passive microwave satellite observations (Mätzler, 1987), thin ice layers may lead to coherent reflections and thus have a strong impact on the microwave emission of snow.

In general, the reflectivity of snow is given by the absolute value of the Fresnel reflection coefficients from all layers (Mätzler, 1987, see equation 2.28). If there are no coherent layers, the reflectivity of snow is dominated by the reflection coefficient from the snow-air interface. In Mätzler (1987) the effect of coherent reflection is demonstrated for the case of an ice lens (i.e., the refractive index of pure ice can be assumed) embedded in a thin snowpack. In this case, absorption can be neglected (imaginary part of the permittivity can be set to zero) and

the reflectivity due to the ice layer can be calculated by:

$$r = 2r_1 \frac{1 - 2\cos(P_1)}{1 + r_1^2 - 2r_1\cos(2P_1)} \quad (2.31)$$

Here, r is the reflectivity and r_1 is the reflection coefficient of the ice lens. P_1 can be calculated from equation 2.29. Assuming an ice layer with thickness $d = 0.5$ cm and a sensor that observes at 18.7 GHz with an incident angle of 50° , the reflectivity of the above described snowpack is 0.089 at vertical polarisation and 0.82 at horizontal polarisation and thus strongly modifies the measured signal. These results show that an ice lens strongly influences the emissivity of a snowpack, especially at horizontal polarisation.

An additional shortcoming of the model is the assumption of radiometrically smooth interfaces. While this might be a good approximation for the internal interfaces within the snowpack, at the ice-snow and snow-air interface, neglecting surface scattering may lead to large uncertainties. In order to estimate the influence of rough surfaces at the microwave frequencies used here, knowledge about the nature of the roughness elements at the ice-snow and snow-air interfaces is needed. These features are, however, hard to obtain due to the destructive nature of measurements.

Figure 2.9 shows the influence of surface roughness on the simulated brightness temperatures (left) and GR (right). Here the roughness height model proposed by Choudhury et al. (1979) was used. In this model, the reflection coefficient is modified by a roughness length (rmsh; see equations 11 and 12 in Choudhury et al., 1979). In Figure 2.9, the rmsh was varied between 0 mm and 10 mm, which is an arbitrary range, since no constrained measurements of the rmsh for the ice-snow and snow-air interface exist.

At vertical polarisation, only a weak influence of the rmsh on the brightness temperatures is found (Figure 2.9, left). This is expected since the rmshs model used here directly influences (lowers) the Fresnel reflection coefficients which are low at vertical polarisation (see section 2.3). A stronger influence of the rmshs is found at horizontal polarisation (due to the generally higher reflectivity). Since the influence is different for different frequencies, also a strong influence on the GR at horizontal polarisation is found (see Figure 2.9, right). Note that this analysis only considers small scale (i.e., wavelength scale) roughness. In addition, large scale roughness due to e.g., deformed ice can have a strong impact on the signal observed by satellites (e.g., Stroeve et al., 2006).

In this thesis, the sea ice version of MEMLS (Tonboe, 2005) is used since the underlying ice can have a strong influence on passive microwave satellite observations (Ulaby and Long, 2014b). A detailed description of the sea ice version of MEMLS is given in Mätzler (2006). In order to calculate volume scattering in the sea ice, Tonboe (2005) used the same approach

as implemented for snow, i.e., the IBA. In the case of sea ice, fresh ice is the host medium and spherical air-bubbles or brine are the inclusion media. However, the IBA is only valid under the assumption of a two-phase medium. In the sea ice version of MEMLS, it is assumed that FYI consists of ice and brine (i.e., no air bubbles) and MYI of ice and air bubbles (i.e., no brine). For MYI, this assumption holds for the top layers where superimposed ice may exist, which is almost saltfree. The depth of this superimposed ice can vary between a few centimetres and up to 40 cm (i.e., Fung and Eom, 1982; Grenfell, 2015; Shokr and Sinha, 1999). Also below this layer, MYI usually contains less salt than FYI.

In the case of FYI, the penetration of the microwaves is limited to a few cm (36 GHz) to one decimetre (7 GHz) (Ulaby and Long, 2014b) and therefore, volume scattering of microwaves only plays a minor role.

Due to the MYI properties (lower density, almost salt-free) microwaves can penetrate several decimeters (20 GHz) up to one meter (7 GHz) into the ice (Ulaby and Long, 2014b). Typical air bubbles in the MYI lead to a scattering of microwaves and thus influences the GR in a similar way as deep snow. In their study, Shokr and Sinha (1999) found a mean circularity of 0.68 for air bubbles in MYI, which means that the air bubble inclusions in the ice are not perfectly spherical. Therefore, the assumption of spherical air bubbles introduces an error and the calculated volume scattering might be inaccurate.

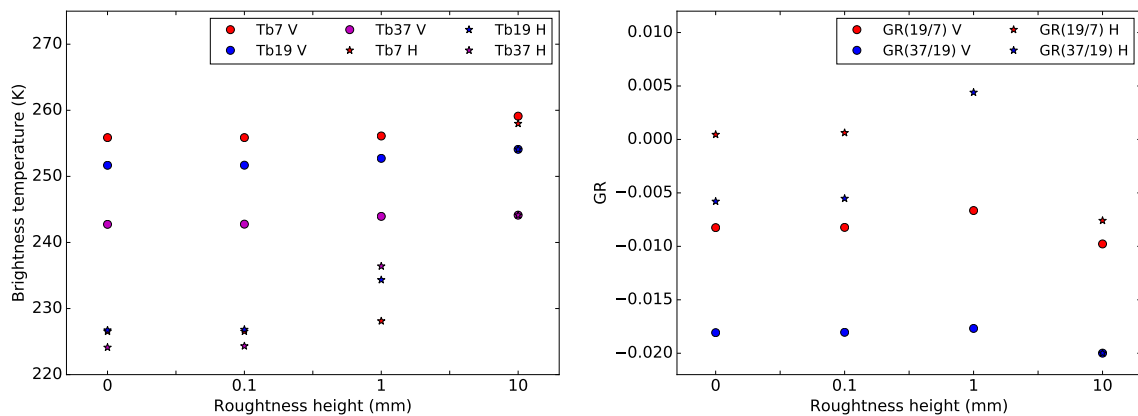


Figure 2.9: Simulated brightness temperatures (left) and GR (right) for a 50 cm deep snowpack assuming different roughness heights of the ice-snow and snow-air interface.

Chapter 3

A New Snow Depth on Arctic Sea Ice Retrieval

In this chapter, a new passive microwave snow depth on Arctic sea ice retrieval is developed. Parts of the results shown here are published in Rostosky et al. (2018). With the launch of the SMMR (Scanning Multi-channel Microwave Radiometer) sensor in 1978 and its successor SSM/I (Special Sensor Microwave/Imager) continuous passive microwave satellite observations became available. Since 2002, observations from the AMSR-E sensor on board of the NASA satellite Aqua (Comiso et al., 2003, 2002 to 2011) and AMSR2 sensor on the JAXA satellite GW-COM (Maeda et al., 2016, 2012 -now) are available, providing higher spatial resolution and observations at additional microwave frequencies. The focus in this chapter will be on the observations from the AMSR-E and AMSR2 sensors. Technical details about the satellite data are given in the Appendix E. As discussed in chapter 1, in-situ observations of snow on Arctic sea ice are rare and cover usually a much smaller area than the spatial resolution of satellite observations (≈ 10 km). Therefore, the in-situ snow depth measurements might not be representative for the average snow depth within the satellite pixel.

Since 2009, the NASA Operation IceBridge campaign (OIB) started (Kurtz et al., 2013a). In this campaign, among other measurements, airborne snow depth measurements were taken in spring (March to April/May) in each of the years from 2009 to now. When this study was performed, data were available for the years 2009, 2010, 2011, 2014 and 2015. The advantage of the airborne snow depth measurements is that they cover a relatively large fraction of several km within a satellite pixel and thus are more likely to be representative for the satellite observations than other in-situ measurements.

Details about the data used in this chapter are given in section 3.1. In section 3.2, a new retrieval is developed based on a regression analysis followed by a first uncertainty estimation

in section 3.3. Then, first results are presented in section 3.4. The chapter closes with a discussion in section 3.5 and a summary in section 3.6.

3.1 Data

The following sections describe the data needed for the development of the new snow depth retrieval. Besides the satellite observations (section 3.1.1) and training dataset (section 3.1.2), also information about the ice type (section 3.1.3) are needed since MYI and FYI have different radiometric properties. In addition, the air temperature is used in order to exclude observations under melting conditions (section 3.1.4).

3.1.1 Satellite Data

The data used here are resampled and regridded passive microwave satellite observations from the AMSR-E and AMSR2 sensors (Cavalieri et al., 2014; Maeda et al., 2016). The instrument description of AMSR-E and AMSR2 can be found in Appendix E. Here, the vertically and horizontally polarised brightness temperature observations at 6.9 GHz, 10.7 GHz, 18.7 GHz and 36.5 GHz (7 GHz, 10 GHz, 19 GHz and 37 GHz hereafter) are used. Although the AMSR-E and AMSR2 instruments are similar, their observations have to be inter-calibrated to guarantee a consistent timeseries. In this study the AMSR2 observations are inter-calibrated to the AMSR-E observations following Du et al. (2014). However, the inter-calibrations was performed in tropical regions over rain forest and ocean (Du et al., 2014) and therefore might not be suited for Arctic regions, especially for sea ice with its very high emissivity.

3.1.2 Operation IceBridge Snow Depth Measurements

In order to train the new retrieval, airborne snow depth measurements from the Operation IceBridge (OIB) campaign are used. The OIB campaign started in 2009 measuring, among other parameters, the radar backscatter of snow on Arctic sea ice. In each year in March and April, several flights are performed. Figure 3.1, left shows the flight tracks in 2015. Most of the flights are performed in the Beaufort Sea, north to the Canadian Archipelago and in the Arctic Ocean. In these areas, predominantly MYI exists and thus, roughly 70% of the flights are performed over MYI.

The measurements are done with a frequency-modulated continuous waveform snow radar (Kanagaratnam et al., 2007; Yan et al., 2017), measuring between 2 GHz and 8 GHz and a footprint of around 1 m, depending on the flight height and observation angle (Newman

et al., 2014). From the measured signal, the snow depth is estimated taking advantage of the different backscatter signals from the snow/ice and atmosphere/snow interfaces. Different methods exist deriving the snow depth from these signals (e.g., Kurtz et al., 2013b; Newman et al., 2014).

The official, published OIB snow depth product is the NSIDC OIB snow depth (Kurtz et al., 2013b). Kwok et al. (2017) compared existing retrievals with in-situ surveys and found that the Newman et al. (2014) product performs best. The Newman et al. (2014) algorithm has recently been improved through the inclusion of two filters to remove erroneous measurements due to specular radar returns arising from leads, and measurements of snow depth below the snow radar resolution (S. L. Farrell, personal communication, October 14-19, 2017). Figure 3.1, right shows the distributions of the NSIDC (blue) and the improved Newman et al. (2014) (red; SLF hereafter) algorithm. While the shape of the distribution is similar for both retrievals, the NSIDC product has a lower mean and modal snow depth. In the following regression study, the main results are obtained using the SLF algorithm and the results using the NSIDC product are shown for comparison.

3.1.3 Ice Type

Since FYI and MYI have different radiometric signatures (Aaboe et al., 2016), it is important to separately train the retrieval over FYI and MYI. The FYI/MYI flag provided with the SLF OIB snow depth is only valid for the flight tracks and the average ice type in the corresponding satellite grid cell could be different. Therefore, an external, pan-Arctic ice type data product is used. When the training was performed, the UB MYI concentration (which was used for later analysis) was not yet available. Therefore, here, the OSI-SAF ice type classification is used.

This product uses AMSR-E/2 GR(37/19) (see equation 3.1) and ASCAT backscatter observations at C-band (5.3 GHz) to distinguish between MYI and FYI. In addition, a confidence level is provided ranging from 1 (unreliable) to 5 (excellent). In the following analysis, only datapoints with confidence level 4 or higher are used. Figure 3.1, left shows an example of the ice type distribution of MYI and FYI in the Arctic for March 2015. Most of the MYI is located in the Central Arctic and north to the Canadian Archipelago.

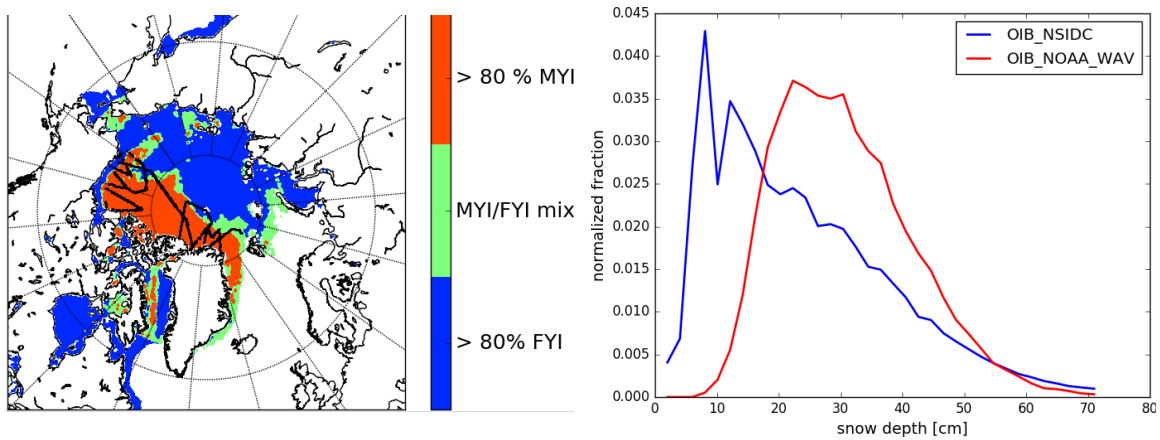


Figure 3.1: Left: Monthly averaged ice type for March 2015 according to the OSI-SAF ice type product (Aaboe et al., 2016). Black lines show the flight tracks of all OIB flights during that period. Right: Distribution of the snow depth from the NSIDC (red) and SLF (blue) retrievals for 2015.

3.1.4 Reanalysis Data

Cavalieri et al. (2012) have demonstrated that the satellite observations used for retrieving snow depth are influenced by weather effects such as warm air intrusions. As described in chapter 2, if the temperature is close to the freezing point or above, the theoretical relation between snow depth and GR or PR (see equation 3.2) diminishes due to the presence of liquid water in the snow. In order to exclude potentially contaminated datapoints from the analysis, a temperature filter is applied over all data using ERA-interim reanalysis 2 m air temperature data (Dee et al., 2011). Only datapoints where the 2 m air temperature are below 275 K (i.e., 2°C) are used for the regression analysis. This threshold is chosen since several studies revealed a positive bias in the reanalysis 2 m temperature over Arctic sea ice of around 1.5 K (e.g., Lüpkes et al., 2010; Pithan et al., 2014). Figure 3.2 shows an example of the 2 m temperature collocated with OIB datapoints from March and April 2014. Roughly 15% of the collocated OIB measurements are about the threshold.

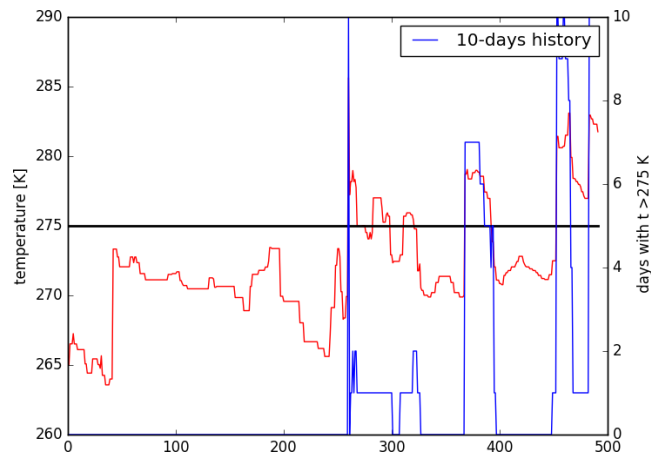


Figure 3.2: 2 m air temperature from ERA5 reanalysis data for the grid cells covered by OIB measurements in 2014. The horizontal black line indicates the 2°C border.

3.2 Regression Analysis

For the training of the retrieval, a robust linear regression model is used (Huber, 1981). The advantage of this model over normal least square methods is that it is less sensitive to outliers in the dataset. As shown in chapter 2, a linear relation between satellite observations and snow can be expected for typical snow depth on Arctic sea ice conditions (see Figure 2.5). The first snow depth on Arctic sea ice retrieval used passive microwave observations at 19 GHz and 37 GHz (Markus and Cavalieri, 1998). However, since 2002, with the AMSR-E and AMSR2 sensors, additional observations are available. Lower frequencies are in general less sensitive to snow depth (see Figure 2.5) but also less sensitive to weather influences (Markus et al., 2006b). The disadvantage of lower frequencies is their coarser spatial resolution (see Table E.1 and Table E.2).

Here, the performance of all microwave frequencies and their combinations in comparison to the SLF and NSIDC snow depth measurements is analysed.

In order to minimise the influence of a small sampling area within the satellite grid cell, only grid cells are used which are covered by at least 10 km of OIB snow depth measurements. This number is a trade of between datapoints which can be used for the training and the sample error. In theory, a larger number of measurements/pixel increases the likelihood, that the average of the sample is representative for the average of the whole pixel and therefore a high coverage would improve the retrieval results (i.e., increase the correlation and decrease the RMSD). However, the number of available datapoints strongly decreases with the required minimum pixel coverage. Less datapoints decrease the robustness of the regression.

Tables 3.1 and 3.2 show the results of the regression analysis using the NSDIC and SLF snow depth products and different channel combinations of the AMSR-E/2 brightness temperature observations. In the first column, the different brightness temperature combinations are shown. GR is the gradient ratio of brightness temperature observations at two different frequencies Tb_{v1} and Tb_{v2} at the same polarisation (equation 3.1) and PR is the polarisation ratio, i.e., the ratio of the vertically (Tb_V) and horizontally (Tb_H) polarised brightness temperature observations at the same frequency (equation 3.2). The advantages of using GR or PR over single brightness temperature observations is that they are (almost) independent of the physical temperature (see chapter 2).

$$GR(Tb_{v1}/Tb_{v2}) = \frac{Tb_{v1} - Tb_{v2}}{Tb_{v1} + Tb_{v2}} \quad (3.1)$$

$$PR(Tb) = \frac{Tb_V - Tb_H}{Tb_V + Tb_H} \quad (3.2)$$

The results for the GR using horizontally polarised brightness temperatures are shown in brackets. In addition, the correlation R and the RMSD (cm) are shown for FYI and MYI, separately. Over FYI the highest correlation and lowest RMSD was found for $GR(19/10)$ and $GR(19/7)$ using the vertically polarised brightness temperatures. For the SLF product (Table 3.2), the correlation and RMSD are -0.74 and 3.69 cm for $GR(19/10)$ and -0.73 and 3.71 cm for $GR(19/7)$ which is better in comparison to the results using the NSDIC product (Table 3.1; for $GR(19/10)$, $R = -0.63$ and $RMSD = 4.21$ cm). Using the horizontally polarised brightness temperatures (values in brackets), the results over FYI are slightly worse. For example, the correlation for $GR(19/7)$ drops to -0.71 and the RMSD increases to 3.81 cm. Very low correlations to the snow depth observations are found for the low frequencies, i.e., for $GR(10/7)$, $PR(7)$ and $PR(10)$. This is expected since low frequency observations are not influenced by volume scattering in snow (see chapter 2).

Over MYI, $GR(19/7)$ performs clearly best ($R = -0.57$ and $RMSD = 5.48$ cm; Table 3.2), while the differences between the results using vertically and horizontally polarised brightness temperatures are small. Similar to FYI, the best results are obtained using the SLF product (compare Table 3.1 and Table 3.2). Based on these results and on the findings of Kwok et al. (2017), the SLF product is used for the development of the new retrieval.

Table 3.1: Regression results of AMSRE/2 observations to OIB NSIDC snow depth for vertically (horizontally) polarised brightness temperatures over FYI and MYI. Here, the results of the gradient ratio (GR(v1/v2)) and polarisation ratio PR(v1) are shown.

	R_{fyi}	R_{myi}	$RMSD_{fyi}$ (cm)	$RMSD_{myi}$ (cm)
GR(10/7)	-0.29 (-0.29)	-0.40 (-0.38)	11.18 (12.27)	11.64 (12.01)
GR(19/7)	-0.60 (-0.57)	-0.55 (-0.52)	4.32 (4.68)	6.50 (6.60)
GR(19/10)	-0.63 (-0.61)	-0.47 (-0.44)	4.21 (4.43)	6.87 (7.04)
GR(37/7)	-0.48 (-0.36)	-0.32 (-0.33)	8.17 (8.66)	6.62 (6.61)
GR(37/10)	-0.50 (-0.44)	-0.31 (-0.34)	5.02 (5.44)	6.51 (5.49)
GR(37/19)	-0.48 (-0.42)	-0.29 (-0.34)	5.43 (5.68)	6.94 (6.88)
PR(7)	-0.00	-0.21	6.09	6.25
PR(10)	-0.05	-0.18	5.95	6.30
PR(19)	0.23	0.01	5.93	6.20
PR(37)	0.17	0.02	6.00	6.4

Table 3.2: Same as Table 3.1 but using the SLF snow depth product.

	R_{fyi}	R_{myi}	$RMSD_{fyi}$ (cm)	$RMSD_{myi}$ (cm)
GR(10/7)	-0.28 (-0.25)	-0.42 (-0.42)	10.12 (10.02)	12.08 (11.96)
GR(19/7)	-0.73 (-0.71)	-0.57 (-0.57)	3.71 (3.81)	5.48 (5.49)
GR(19/10)	-0.74 (-0.71)	-0.51 (-0.50)	3.69 (3.83)	5.75 (5.77)
GR(37/7)	-0.48 (-0.25)	-0.46 (-0.42)	7.23 (8.51)	6.41 (6.50)
GR(37/10)	-0.51 (-0.45)	-0.46 (-0.44)	5.02 (5.52)	6.06 (6.08)
GR(37/19)	-0.52 (-0.49)	-0.37 (-0.38)	4.64(4.82)	6.19 (6.18)
PR(7)	-0.06	-0.21	5.05	6.25
PR(10)	-0.13	-0.03	5.00	6.12
PR(19)	0.22	0.00	4.93	6.20
PR(37)	0.18	0.05	4.97	6.19

An additional test is performed to analyse, if similar results are obtained using only the AMSR-E or AMSR2 sensor for the regression analysis. Table 3.3 and 3.4 show the comparison between the regression results using only AMSR-E or AMSR2 data or the whole dataset for GR(19/7) and GR(37/19) for FYI (Table 3.3) and for MYI (Table 3.4). Over FYI, all regression coefficients are similar which underlines that the inter-calibration between AMSR-E and AMSR2 observations is also valid for Arctic conditions. A slight variability is expected due to different coverage of the snow depth measurements and different snow condition in

each year. Over MYI, the variability of the regression results is higher than over FYI but stable for GR(19/7). For GR(37/19) large differences between the results using the AMSR-E and using the AMSR2 observations are found.

Since GR(19/7) and GR(19/10) perform similarly well over FYI but GR(19/7) performs clearly best over MYI, it is convenient to only use GR(19/7) for both, FYI and MYI.

In the following analysis, the performance of GR(19/7) is further evaluated and compared to the performance of GR(37/19) which has been used in past studies (e.g., Markus and Cavalieri, 1998).

Figure 3.3 shows a scatter plot between SLF snow depth and GR(19/7) (left) and GR(37/19) (right) for FYI, as well as the regression coefficients slope and intercept, the correlation R , the RMSD (cm) and the number of points, N . In addition to the higher correlation, the RMSD is also lower for GR(19/7). The dynamical range of the GR , here defined from the 5th to the 95th percentile of the given snow depth observations (i.e. from 15 cm to 35 cm) is 0.021 for GR(19/7) and 0.028 for GR(37/19). This shows that GR(37/19) is more sensitive to changes in snow depth.

Table 3.3: Regression results using AMSR-E and AMSR2 observations for FYI. In addition, the results using both sensors (AMSRX) are shown.

	AMSR-E		AMSR2		AMSRX	
	GR(19/7)	GR(37/19)	GR(19/7)	GR(37/19)	GR(19/7)	GR(37/19)
R	-0.70	-0.61	-0.60	-0.57	-0.73	-0.52
RMSD (cm)	4.32	4.89	3.72	4.44	3.71	4.64
slope (cm)	-519	-372	-504	-291	-553	-279
intercept (cm)	20.37	18.17	18.27	15.18	19.26	17.82

Table 3.4: Same as Table 3.3 but for MYI.

	AMSR-E		AMSR2		both	
	GR(19/7)	GR(37/19)	GR(19/7)	GR(37/19)	GR(19/7)	GR(37/19)
R	-0.47	-0.22	-0.51	-0.45	-0.57	-0.37
RMSD (cm)	5.50	6.08	6.55	7.34	5.48	6.19
slope (cm)	-406	-98	-278	-277	-368	-152
intercept (cm)	18.23	26.52	20.54	12.99	19.34	23.58

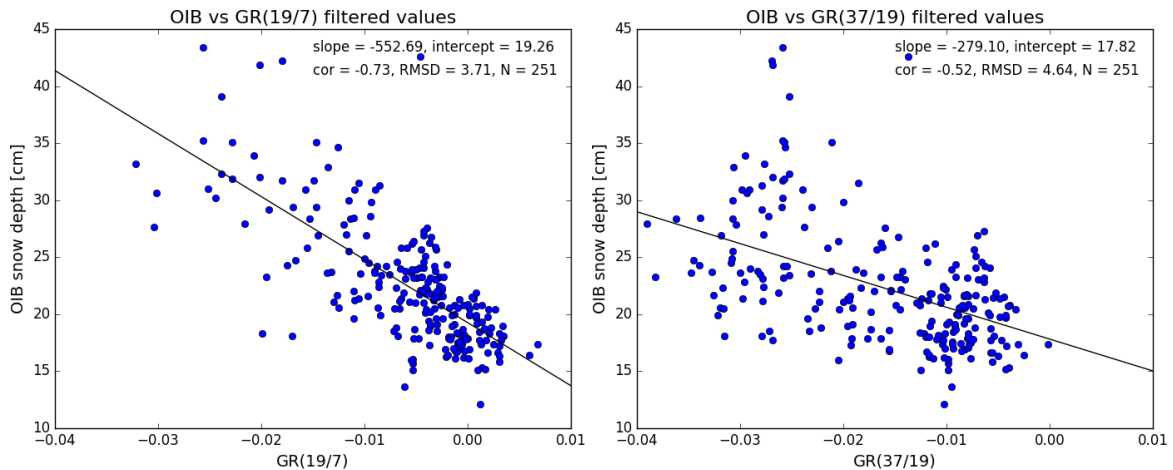


Figure 3.3: Scatter plot between OIB snow depth and GR(19/7) (left) and GR(37/19) (right) over FYI. The slope, intercept and RMSD are provided in cm.

The advantages of the lower frequencies are that they are less influenced by weather effects and snow metamorphism (Powell et al., 2006; Willmes et al., 2014) and are potentially more sensitive to deeper snow. The fact that the snowpack in March and April has undergone metamorphism can explain, why GR(19/7) performs much better than GR(37/19). This might also explain why the correlation between GR(37/19) and SLF snow depth measurements ($R = -0.52$) is lower than the correlation ($R = -0.60$) found by Markus and Cavalieri (1998). On the other hand, these frequencies are less sensitive to fresh-fallen snow with small grains. In addition, in shallow snow layers, the effect of scattering would be much smaller for GR(19/7) than for GR(37/19). Powell et al. (2006) suggested that a combination of GR(19/10) and GR(37/19) might be best to derive snow depth on Arctic sea ice. The theoretical suggestion was tested here but did not yield to an improvement. Most likely, the reason is similar as described before and is due to the old and transformed snow pack.

Figure 3.4 shows a scatter plot between the SLF snow depth and GR(19/7), left and GR(37/19), right over MYI. In comparison GR(19/7) performs better over MYI ($R = -0.57$) than GR(37/19). For the latter, the correlation is only -0.37 and the slope is less than half of the GR(19/7) one, confirming previous studies (e.g., Brucker and Markus, 2013) that it is not possible to derive reliable snow depth from GR(37/19) over MYI.

As described in chapter 2, this is mostly due to the influence of the MYI properties on the emission at 37 GHz. Due to the low salinity in the top layers of the MYI, the microwave signal can penetrate several tens of centimetres (depending on the wavelength and temperature) into the ice (Ulaby and Long, 2014b). Air bubbles, which frequently occur in the top layers of MYI, scatter microwaves. Therefore, it is difficult to distinguish between the effects of snow and MYI at 37 GHz. This scattering, however, is frequency dependent and

for typical air bubble sizes decreases with frequency (Stogryn, 1987). Therefore, MYI has a substantially lower emissivity than FYI at the higher microwave frequencies considered in this study, that is, 37 GHz and 19 GHz, but its emissivity approaches that of FYI at the lower frequencies, that is, at 7 GHz. The correlation between GR(19/7) and SLF snow depth is significant better than of GR(37/19), which is due to the lower influence of the air bubbles in MYI at 19 GHz.

Still, the RMSD over MYI (5.48 cm) is higher relative to FYI (3.87 cm). This might be due to the fact that the snow depth over MYI is in general much more variable, due to the higher amount of deformed ice, than over FYI. In addition, it was found that OIB measurements are less accurate over deformed ice (e.g., Yan et al., 2017). This results in a generally lower representatives of the few OIB snow depth measurements within one large satellite grid cell of 25 km². In addition, large-scale surface roughness is usually much higher over MYI and indeed Stroeve et al. (2006) found that that surface roughness has a large impact on the microwave emission of sea ice with snow on top.

Even though the RMSD being larger for MYI than for FYI, the reasonably good performance of GR(19/7) enables the derivation of snow depth over Arctic MYI, at least during spring. In summary, based on all available SLF snow depth data the conclusion is that GR(19/7) is best suited for snow depth retrieval over FYI and MYI. The respective regression equations are given below as equations 3.3 (FYI) and 3.4 (MYI). GR(19/7) was corrected for open water contributions using open water tie-points derived by Ivanova et al. (2015).

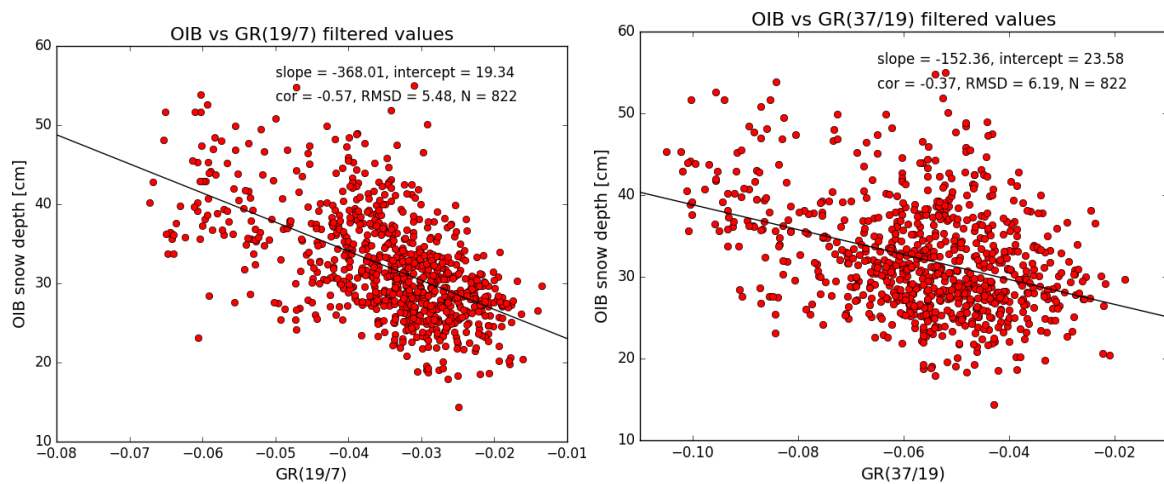


Figure 3.4: Scatter plot between OIB snow depth and GR(19/7) (left) and GR(37/19) (right) over MYI. The slope, intercept and RMSD are provided in cm.

$$Sd_{FYI}(cm) = 19.26 - 553 * GR(19/7) \quad (3.3)$$

$$sd_{MYI}(cm) = 19.34 - 368 * GR(19/7) \quad (3.4)$$

3.3 Uncertainty Estimation

In this section the uncertainty of the snow depth retrieval is estimated. Based on the data available, two types of uncertainties can be investigated:

- (a) the uncertainty due to the limited spatial and temporal sample size (i.e., the statistical uncertainty in the fit parameters)
- (b) the uncertainty of the retrieval due to the uncertainty of the satellite measurements itself

(a) In order to address the uncertainty introduced by the limited sample size, a sensitivity analysis is performed to account for the interannual variability of the regression coefficients in equations 3.3 and 3.4. The regression is performed for every possible 4-year combination between 2009 and 2015 (no satellite observations for 2012 due to a gap between AMSR-E and AMSR2 and no SLF snow depth for 2013), that is, for 2009, 2010, 2011, 2014 or 2009, 2010, 2011, 2015, etc. With this method, five different regression coefficients are obtained using a slightly different training data set including the results using all years. They can be compared with each other to quantify how stable the regression coefficients are over time. This also gives an indication for the expected retrieval uncertainty for future years. The different regression coefficients for the retrieval are summarised in Table 3.5. In addition, the numbers of available datapoints are given.

Over FYI, the slope varies between -474 cm and -649 cm, the slope using all years is -553 cm. The intercept varies between 18.7 cm and 20.0 cm, the intercept using all years is 19.3 cm. Over MYI the variability of the coefficients is higher. The slope varies between -227 cm and -413 cm (all years = -347 cm) and the intercept between 17.3 cm and 22.3 cm (all years = 19.3 cm). The uncertainties due to the limited sample size are then calculated from the standard deviation of the regression coefficients over the five results shown in table 3.5. Those are ± 0.6 cm for intercept and ± 58 for slope over FYI and ± 1.8 cm for intercept and ± 60 for slope over MYI.

(b) The uncertainty due to the contributing parameters to the retrieval can be obtained from Gaussian error propagation (see appendix A) and is calculated from equation A.11.

Table 3.5: Regression coefficients and number of available measurements for the different samples over FYI and MYI and for all samples (last row). In addition, the number of available data points is shown for FYI and MYI.

Excluded years	FYI			MYI		
	Intercept (cm)	slope	Number	Intercept (cm)	slope	Number
2009	18.7	-474	157	18.1	-335	733
2010	18.5	-649	209	18.0	-355	806
2011	19.6	-562	232	19.0	-343	780
2014	20.0	-524	200	22.3	-227	531
2015	19.7	-579	206	17.3	-413	692
All years	19.3	-553	251	19.3	-368	822

The uncertainty of the observed brightness temperatures of AMSR-E/2 is 1 K (see Table E.1 and Table E.2), and the uncertainty of the retrieved ice concentration is set to 5%. σ_a and σ_b are the uncertainties of the regression coefficients themselves (standard output of the regression model used here). Using all years they are 0.035 cm (σ_a) and 26.6 cm (σ_b) for FYI and 0.550 cm (σ_a) and 15.0 cm (σ_b) for MYI. The standard deviation of the Gaussian uncertainty of the GR is 0.0043 for the data used in this analysis (calculated from equation A.7).

To obtain an estimate of the retrieval uncertainty, equations 3.3 and 3.4 are solved for GR values between 0.01 and -0.06 for FYI and -0.01 and -0.08 for MYI, respectively. Those values are based on the range found in the AMSR-E/2 data set used for training (see Figure 3.3 and Figure 3.4). In addition, the retrieval uncertainty is computed using equation A.11 and the uncertainties found in (a) and (b). Figure 3.5 shows the results for FYI (left) and for MYI (right). The uncertainty increases with snow depth and is higher over MYI. Over FYI the uncertainty varies between 0.1 cm and 6.0 cm, while over MYI it varies between 3.4 cm and 9.4 cm. The uncertainty is dominated by the year to year variability of the regression coefficients discussed under (a). The errors of the input parameters have only a small contribution of 0.1 cm to 1.7 cm over FYI and 0.7 cm to 2 cm over MYI.

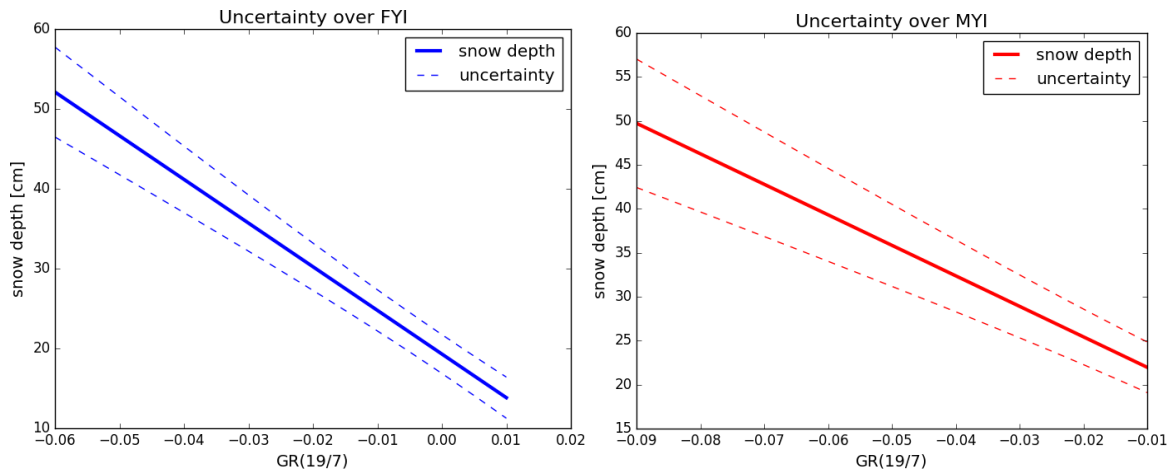


Figure 3.5: Regression models including uncertainty (dashed lines) for the AMSR-E/2 snow depth for FYI (left) and MYI (right) using the range of GR(19/7) values found in section 3.2.

3.4 Evaluation

To evaluate the performance of the new developed snow depth retrieval (AMSR-E/2 retrieval hereafter) it is compared to independent SLF measurements and to the existing NSIDC snow depth product (Comiso et al., 2003). In order to have an independent data set for the evaluation, SLF snow depth measurements obtained during the 2015 flight surveys were excluded from the following calculations, that is, the coefficients from Table 3.5, column five were used to calculate the snow depth over FYI and MYI, respectively. It can be assumed that the snow depth measurements are independent from year to year. The choice of the evaluation year is somewhat arbitrary, but 2015 is suitable, since it contains sufficient measurements over FYI. The SLF product is limited to the months March and April and therefore, the evaluation of the retrieval will first focus on spring. Thereafter, the performance during early winter will be discussed.

3.4.1 Evaluation with SLF Measurements

The monthly average of the AMSR-E/2 snow depth for March 2015 is shown in Figure 3.6, left and provides a first overview of the retrieval. The black contour marks the approximate border between FYI and MYI based on the OSI SAF ice type product. In order to minimise the influence of ice concentration, only grid cells with an ice concentration greater than 80% are considered. The snow depth is calculated from daily averaged brightness temperature observations. Then either equation 3.3 or 3.4 is used based on the ice type classified by the OSI SAF product.

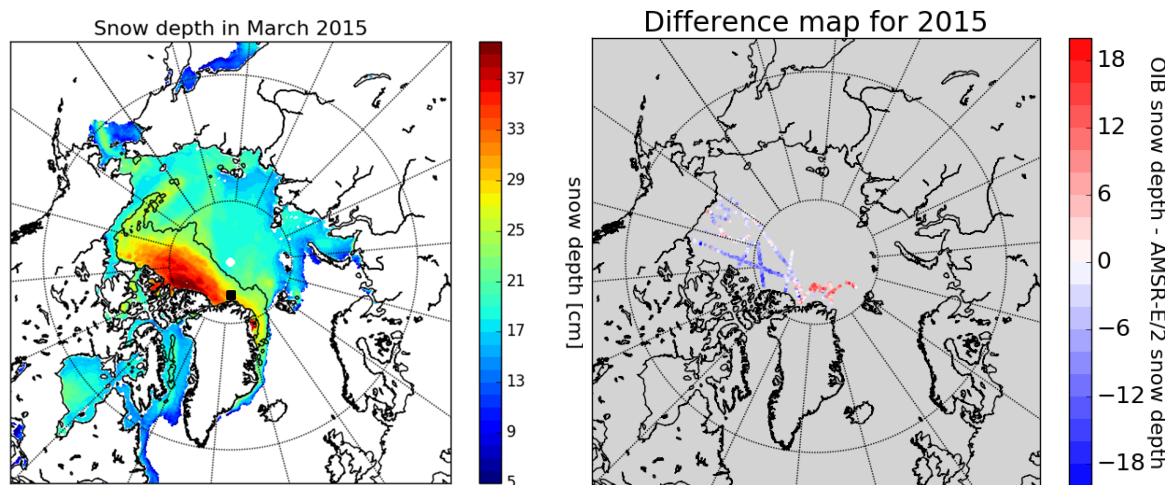


Figure 3.6: left: Monthly averaged snow depth in March 2015. The black box shows the MYI region used for Figure 3.9. Right: Difference between the OIB and AMSR-E/2 snow depth for March and April 2015.

However, in the transition zone between FYI and MYI, the confidence level of the OSI SAF ice type product is low. Here only grid cells with confidence level 4 or higher are used. This approach results in some gaps in the transition zone on individual days, but these gaps disappear in the monthly average. The deepest snow depth is retrieved on sea ice north of Greenland and the Canadian Archipelago and is between 32 cm and 45 cm deep. The lowest values are found in the Kara and Laptev seas, where the snow depth is between 10 cm and 25 cm. In general, snow is deeper on MYI than on FYI, which is in agreement with model results (Blanchard-Wrigglesworth et al., 2015; Castro-Morales et al., 2017a).

The differences between the AMSR-E/2 snow depth and the SLF snow depth measurements for March and April 2015 are shown in Figure 3.6, right. The AMSR-E/2 retrieval slightly overestimates the SLF snow depth in the Beaufort Sea, where mainly FYI exists. Over sea ice north to the Canadian Arctic Archipelago the overestimation can be up to 10 cm. Underestimations up to 15 cm are found north of Greenland and of the Fram Strait.

To quantify the AMSR-E/2 retrieval performance the histogram of the differences of OIB minus AMSR-E/2 snow depth in March and April 2015 is shown in Figure 3.7, left for FYI (blue) and MYI (red). In Figure 3.7, right the differences of SLF minus AMSR-E/2 snow depth based on (i) GR(19/7) (blue bars) are shown together with the retrieved snow depth based on (ii) GR(37/19) using the regression coefficients found in this study (magenta bars, see Figure 3.7, left) and (iii) the traditional NSIDC GR(37/19) regression coefficients (Comiso et al., 2003) for FYI (green bars).

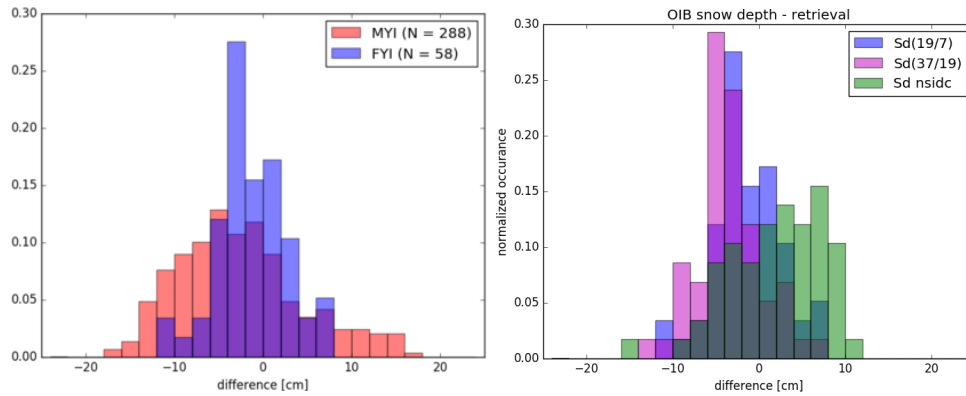


Figure 3.7: Left: Distribution of the differences of SLF minus AMSR-E/2 snow depth over FYI and MYI. Right: Distribution of the differences of SLF minus AMSR-E/2 snow depth for FYI based on GR(19/7) (blue bars), based on GR(37/19) using the new coefficients (magenta bars), and using the NSIDC coefficients (green bars). Both histograms are normalised to 1. The bin width is 2 cm.

Overall, the differences are much smaller over FYI than over MYI (Figure 3.7, left), which is expected since the correlation and the RMSD are generally better over FYI (see section 3.2). The mean difference is -2.1 cm for snow on FYI and -4.0 cm for snow on MYI. Over FYI, 93% of the differences are smaller than 5 cm and 95% are smaller than 10 cm. Over MYI, 56% of the differences are smaller than 5 cm and 87% are smaller than 10 cm.

Comparing the OIB snow depth with the snow depth derived from the AMSR-E/2 retrieval based on GR(19/7) (i) the AMSR-E/2 retrieval based on GR(37/19) (ii) and the NSIDC retrieval based on GR(37/19) (iii), it is demonstrated that the new retrieval (i) performs better. The mean difference of SLF minus AMSR-E/2 snow depth based on GR(37/19) is -3.9 cm when using the regression coefficients derived in this study (ii) and -0.3 cm when using the NSIDC coefficients (iii), that is, the NSIDC retrieval has a smaller bias. However, the spread of the differences is much larger for the NSIDC data (RMSD = 5.2 cm) and only 55% differences are below 5 cm. For the AMSR-E/2 product based on GR(37/19) (ii) 74% of the differences are below 5 cm and the RMSD drops to 3.5 cm. For the GR(19/7) retrieval the differences to SLF is -2.1 cm and with 93% of the differences smaller than 5 cm the performance is best. Thus, based on the comparison to the SLF data and the existing NSIDC snow depth it is concluded that the new retrieval developed in this study, which is based on GR(19/7), shows improved performance over FYI, and reasonable results over MYI.

The probability density function of the AMSR-E/2 snow depth (blue) and the OIB snow depth (red) is shown in Figure 3.8 for FYI (left) and MYI (right) based on all available SLF measurements. In addition, for FYI the corresponding probability density function derived using the NSIDC snow depth retrieval (Comiso et al., 2003) is shown in green. As

with the previous results, the OIB snow depth observations are averaged over 25 km x 25 km satellite grid cells. Over FYI, a clear mode is found at a snow depth of 20 cm in the AMSR-E/2 and SLF distributions, while the NSIDC product has its mode at 8 cm. The snow depth distributions derived from the AMSR-E/2 and SLF retrievals are generally in close agreements, although the AMSR-E/2 distribution is slightly narrower. Snow depth values between 12 cm and 16 cm in particular are underrepresented in the AMSR-E/2 product. Also, snow depths greater than 40 cm are not retrieved in the AMSR-E/2 product.

Over MYI a mode is found at 25 cm in both snow depth distributions, and again, the AMSR-E/2 retrieval cover a smaller range than the SLF results. In particular, thin snow on MYI (< 20 cm) is not resolved by the satellite retrieval. This is consistent with the results shown earlier in figure 3.4, where low snow depths are not reproduced by the linear fit. Also snow deeper than 42 cm is underrepresented in the AMSR-E/2 snow depth product. A quadratic instead of a linear fit might be able to better reproduce the lower snow depths over MYI. However, a brief investigation of this approach (not shown) revealed that a quadratic regression model (i.e., $Sd = a + bx + cx^2$) leads to large uncertainties in the regression coefficients and therefore is not further investigated.

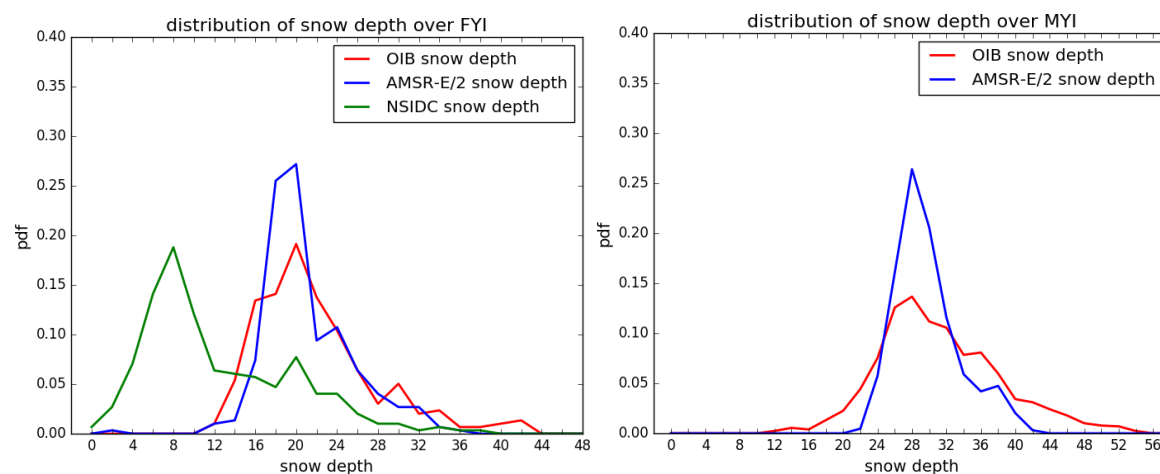


Figure 3.8: Distribution of the AMSR-E/2 snow depth (blue) and the OIB snow depth (red) over FYI (left) and MYI (right). The distribution using the coefficients of the NSIDC retrieval over FYI is shown in green. The bin width is 2 cm.

3.4.2 Timeseries Analysis

Since the SLF snow depth measurements are only available for March and April, the evaluation of the retrieval is limited to these months. Based on the analysis the retrieval performance is reasonable over MYI (Figure 3.7, left) in these months. However, in early winter, it is important to note that the MYI has a strong impact on the microwave emission, even at lower

frequencies. This influences the AMSR-E/2 retrieval over MYI. Figure 3.9 shows the time series of retrieved snow depth over MYI (5×5 grid cells, i.e., 125 km^2 , black square in figure 3.6, left) for winter 2013 to spring 2016 (the summer months are flagged out). The black lines are the AMSR-E/2 snow depths for the 25 single grid cells and the red line shows the average. From the beginning of the freezing season, high snow depths of around 30 cm to 35 cm are retrieved. Except for winter 2014/2015, the snow depth remains around this value until spring. Then it slightly increases again until late spring when potentially melting starts. In comparison, for this region, the Warren climatology (Warren et al., 1999, W99 in the following) suggests an increase of the snow depth from 20 cm in September to 38 cm in April. MYI has a similar contribution to GR as deep snow, although its influence is lower at 7 GHz and 19 GHz than at 37 GHz. Considering the outcome shown in Figure 3.9, the influence of the MYI on the microwave emission seems to dominate the signal of the snow during the winter season. However, the results found in this study and especially the reasonable correlation of GR(19/7) to SLF snow depth observations over MYI indicate that in spring the contribution of snow on the GR dominates the signal of MYI (Figure 3.4). This would, within a higher error range, allow the retrieval of snow depth over Arctic MYI from March to the onset of the melt. One possible explanation for this behaviour could be that snow properties such as snow grain size and density change over the season. For example, freshly fallen snow is almost transparent in the microwave region.

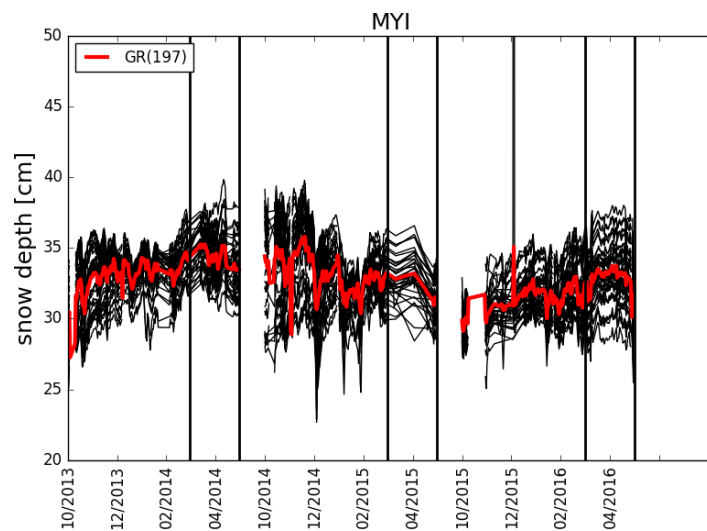


Figure 3.9: Retrieved snow depth over MYI from 2013 to 2016. Black lines show the snow depth for the 25 single grid cells and the red line the average. The vertical lines frame the months March and April.

In late winter/spring the snow contributes much more to microwave scattering than the underlying MYI. Without additional quantitative information about the influence of MYI on the GR it is not possible to estimate when the influence of MYI is low enough to reliably use GR(19/7) for snow depth retrieval.

The main advantage of a satellite-borne snow depth retrieval over existing snow depth climatologies is that it also retrieves the interannual variability of the snow depth. Figures 3.10 and 3.11 show the seasonal evolution of the AMSR-E/2 snow depth over FYI for the period 2005 to 2016 in the Beaufort Sea (Figure 3.10) and in the East Siberian Sea (Figure 3.11). As in Figure 3.9, the snow depth is averaged over 25 grid cells. Snow depth based on the Warren climatology (Warren et al., 1999) is shown in the last column (W99) of the graph. On average, the AMSR-E/2 monthly averaged snow depth is lower than the W99 snow depth in both areas. This is expected because the Warren climatology contains data back to the 1950s when the MYI area and thus the snow depth was larger. In single winters, the AMSR-E/2 snow depth can differ strongly from W99 climatology in both regions. For example, in winter 2014/2015 the maximum snow depth is 32 cm in the Beaufort Sea (Figure 3.10), which is comparable to the W99 climatology of 34 cm, while the maximum snow depth in winter 2012/2013 is with 17 cm about 18 cm lower. Overall, the interannual and seasonal variability is higher in the Beaufort Sea (Figure 3.10) than in the East Siberian Sea (Figure 3.11). In both regions, the seasonal evolution of the AMSR-E/2 snow depth provides good results with an expected increase of the snow depth from October to March. These two examples demonstrate the advantage of the satellite retrieved snow depth product compared to the Warren climatology which does not include interannual variability.

In Figure 3.12, the monthly averaged March and April AMSR-E/2 and SLF snow depths over FYI (left) and MYI (right) are shown for the whole SLF measurement period (2009 to 2015). For each year and month, all available collocated SLF snow depth measurements and AMSR-E/2 derived snow depths are averaged. The exact positions of the OIB flights can differ from month to month and year to year, but the regions they cover are similar. The error bars display the uncertainty of both products. For the SLF snow depth an uncertainty of 5 cm is assumed. The uncertainty of the AMSR-E/2 snow depth is based on the results from section 3.3.

Over FYI (Figure 3.12, left) the mean SLF and AMSR-E/2 snow depths in March and April are very similar. They agree within ± 2 cm in most of the years (note that there are no collocated measurements over FYI in April 2011 and 2014). Over MYI (Figure 3.12, right), large differences between SLF and AMSR-E/2 snow depths are found in single months (e.g., in April 2011 and 2015) while some years are in good agreement (e.g., March and April 2010).

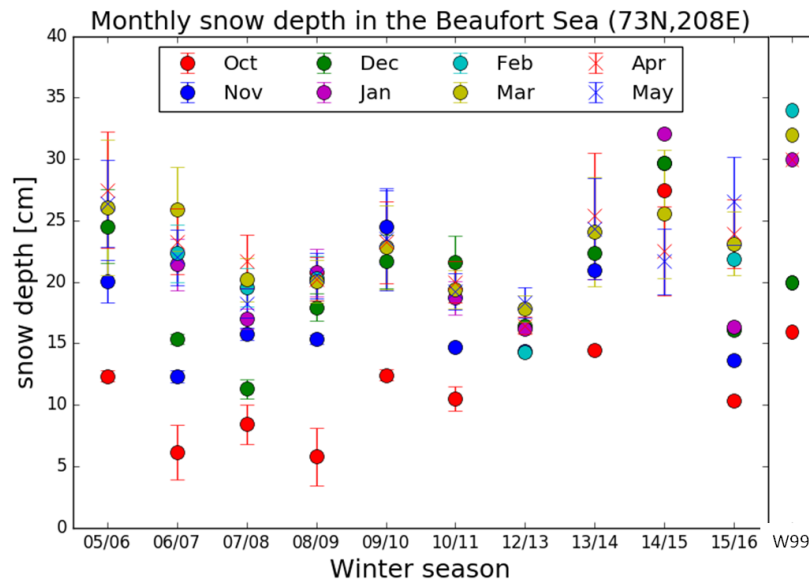


Figure 3.10: Monthly averaged AMSR-E/2 snow depth in the Beaufort Sea from winter 2005/2006 to winter 2015/2016. In addition the snow depth based on Warren climatology (W99) is shown on the far right outside the main plot region. The error bars are calculated from the standard deviation of the surrounding five grid cells.

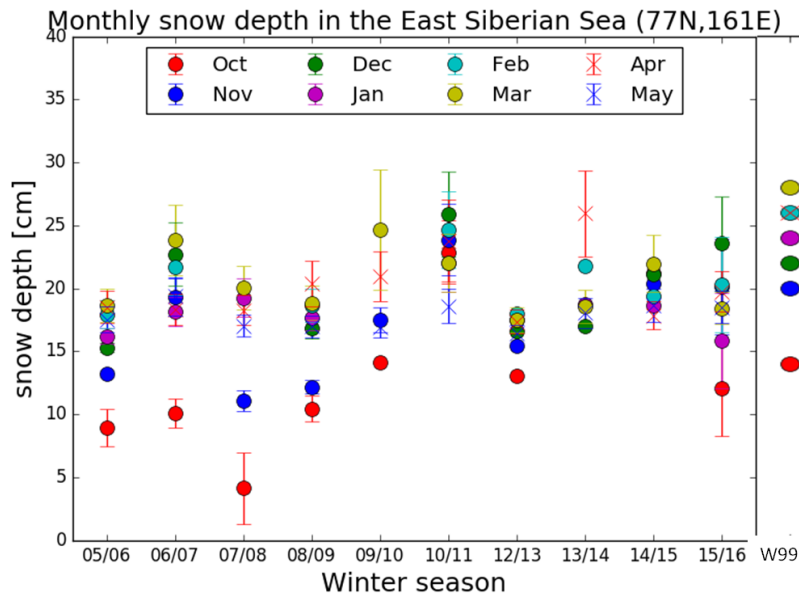


Figure 3.11: Same as Figure 3.10 but for the East Siberian Sea.

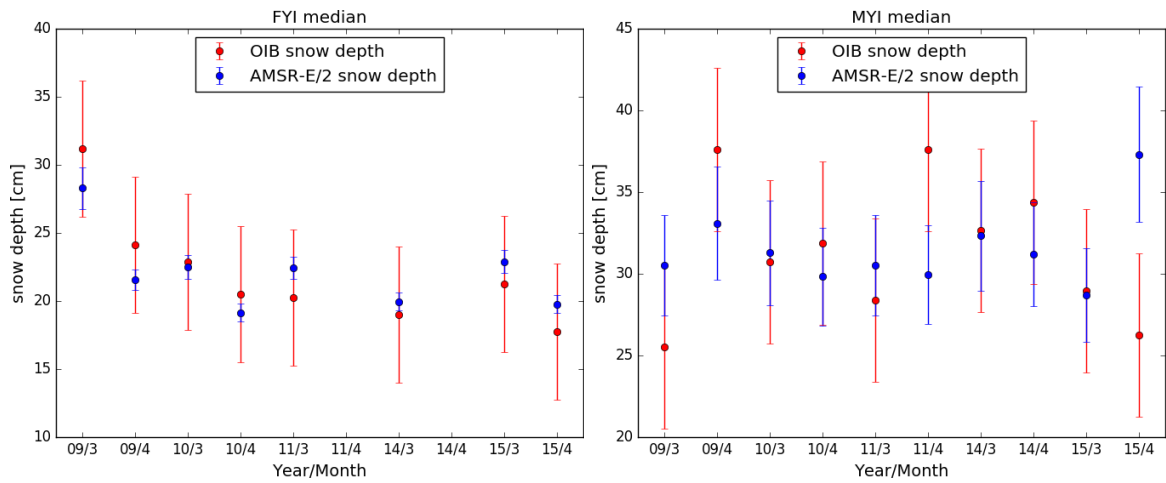


Figure 3.12: Monthly averaged March and April AMSR-E/2 and SLF snow depth over FYI (left) and MYI (right) from 2009 to 2015 (no data for 2012 and 2013). The error bars display the uncertainty of the products.

These results demonstrate that over FYI the AMSR-E/2 snow depth retrieval, using a constant set of regression coefficients, is able to reproduce the interannual variability found in the SLF snow depth measurements. Over MYI the AMSR-E/2 snow depth retrieval has problems to reproduce the interannual variability of the SLF measurements in some years.

Based on all available satellite observations (status April 2019), a timeseries of 16 years of snow depth on Arctic sea ice (no data for winter 2011/2012) can be produced to analyse possible trends. Figure 3.13 shows the monthly averaged snow depth in November (left; note that in November, snow depth is only retrieved over FYI) and March (right) for the whole 2002 to 2019 period. In April possible melt events could cause errors in the calculated snow depth since the retrieval does not work over wet snow.

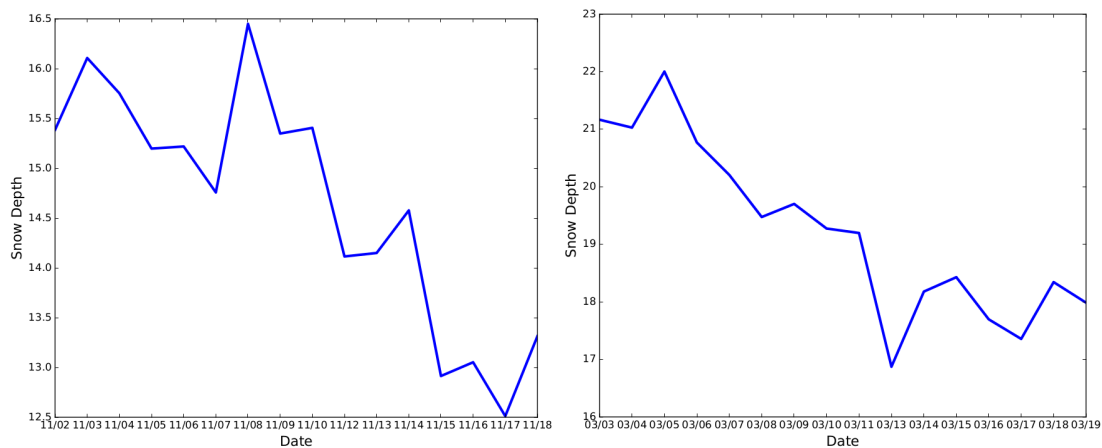


Figure 3.13: Timeseries of the monthly averaged snow depth in November (left) and March (right) from 2002 to 2019.

In both, early winter and Spring, a decline in snow depth is visible. If not stated differently, all trends shown below reach significance level (p value < 0.001). The trend is slightly more pronounced in spring ($= -0.27$ cm/year) than in November ($= -0.2$ cm/year). The trend in March snow depth is similar to the trend Webster et al. (2014) found ($= -0.29$ cm/year) for the time period from 1950 to 2013.

Figure 3.14 shows the monthly averaged snow depth for March for FYI only (left) and MYI only (right). Here, a threshold of $< 20\%$ MYI concentration is chosen for the snow depth on FYI and a threshold of $> 80\%$ MYI concentration is chosen for the snow depth on MYI. A negative trend is found over both, FYI ($= -0.21$ cm/year) and MYI ($= -0.27$ cm/year). Over MYI, the interannual variability of the snow depth is much more pronounced than over FYI. Based on this data, March 2015 had exceptional high snow depth compared to the years before and after. Indeed, during the N-ICE2015 campaign, an exceptional deep spring snowpack was observed in the Atlantic sector north of Svalbard (Rösel et al., 2018a).

Figure 3.15 shows the same as Figure 3.13 but for six different Arctic regions (see Figure 5.9). The regions are chosen such that they cover different snow and ice conditions (see chapter 5 for more details). In November (Figure 3.15, left) no snow depth is retrieved in the Arctic Ocean since in this region, mainly MYI exists. A high interannual variability in November is found in most regions (3.15, left) but it is especially pronounced in the Atlantic Sector and Beaufort Sea. Significant trends are only found in the Kara Sea ($= -0.24$ cm/year) and Labrador Sea ($= -0.18$ cm/year).

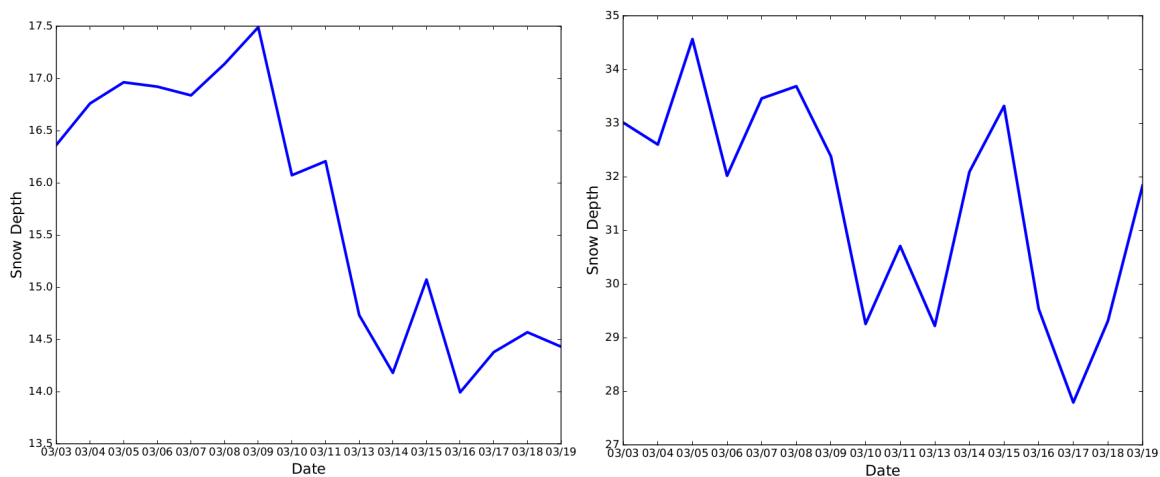


Figure 3.14: Timeseries of the monthly averaged snow depth in March over FYI (left) and MYI (right) from 2002 to 2019.

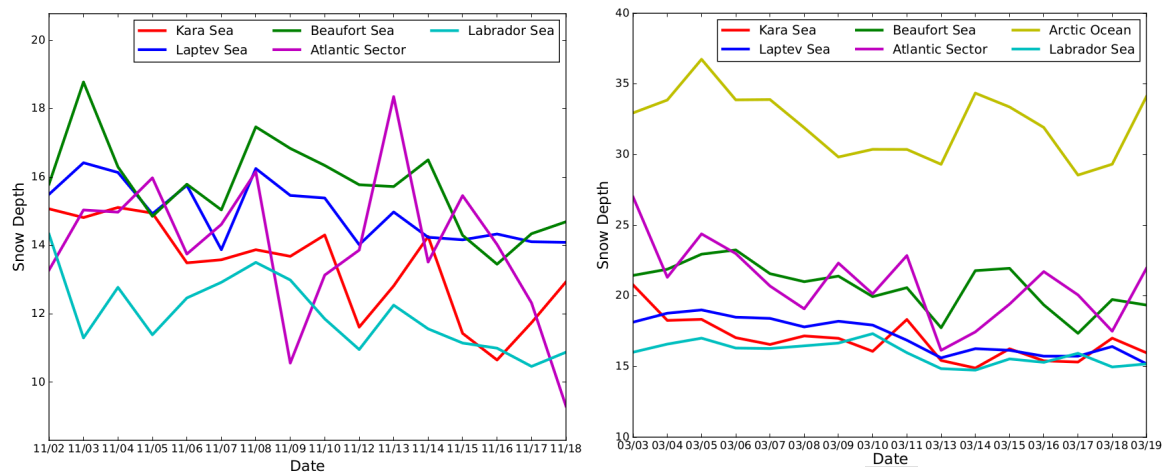


Figure 3.15: Timeseries of the monthly averaged snow depth in November (left) and March (right) from 2002 to 2019 for six different Arctic regions (see Figure 5.9).

In March (Figure 3.15, right), the strongest negative trend is found in the Atlantic Sector ($= -0.28$ cm/year). In the Laptev Sea, the trend is around -0.20 cm/year and in the Kara Sea -0.14 cm/year. In the other regions, the trend is below 0.1 cm/year or does not reach significance level (p value > 0.05). The seasonal development of the spatial distribution of the snow depth is analysed below for the winter season 2005/2006 and 2018/2019. Figure 3.16 shows the monthly averaged snow depth for the winter season November 2005 (a) to April 2006 (f). Here, instead of the OSI-SAF ice type, the MYI concentration product from Ye et al. (2016) was used. The data is available on a daily basis from <https://seaice.uni-bremen.de/multiyear-ice-concentration/> (accessed, 10 march 2020). The advantages of this product is that it provides a MYI concentration instead of a binary ice type. Overall, the snow depth increases over the course of the season. In November (Figure 3.16 (a)), the highest snow depth (20 cm) is retrieved close to the FYI/MYI transition zone while in the marginal ice zone, the snow depth is between 5 cm (e.g., in the East Siberian Sea and Chukchi Sea) and 15 cm (e.g., Kara Sea). From December to March (Figure 3.16 (a) to (e)), the snow depth slightly increases in most regions of the Arctic and is highest in the MYI area north of Greenland and north of the Canadian Archipelago. In April (Figure 3.16 (f)) the snow depth decreases in parts of the Atlantic Sector, which is most likely due to the onset of melt. Overall, especially in March and April, the spatial variability of the retrieved snow depth over FYI is low. In most of the areas, snow depth over FYI in March and April is between 15 cm and 25 cm. Only in the marginal ice zones, low snow depths are retrieved.

Figure 3.17 shows the same as Figure 3.16 but for the winter season November 2018 to April 2019. In all months, the retrieved snow depth is lower compared to season 2005/2006. Especially in November (Figure 3.16 (a)) and December (Figure 3.16 (b)) the retrieved

snow depth in 2018 is, in some regions, much lower than in 2005. This can be related to a later freezeup in 2018 in the Laptev and East Siberian Seas. Based on a quick assess of sea ice concentration maps (not shown here) provided by <https://seaice.uni-bremen.de/databrowser/#p=sic> (accessed 19 March 2020), these regions were not fully ice covered until 06 November, which was roughly two weeks later compared 2005. Since the majority of the Arctic snowpack builds in Autumn (Webster et al., 2014), a later freezeup can strongly reduce the overall snow depth, depending on the meteorological situation in each year. Indeed, Webster et al. (2014) related the thinning of the Arctic snowpack to a shorter accumulation period in recent years which was, according to their analysis, most pronounced in the Beaufort Sea and Chukchi sea.

In March and April 2019 (Figure 3.16 (e) and (f)), the Arctic averaged snow depth is around 3 cm lower than in 2006 (see Figure 3.13, left) which is mainly due to lower snow depths retrieved in the Central Arctic, Laptev Sea and Beaufort Sea (see Figure 3.15).

3.5 Discussion

The empirical regression coefficients derived here depend on the training data set. This results in potential limitations of the retrieval since the SLF snow depth observations used here as the training data set are limited in space and time and are therefore unlikely to be representative of the whole Arctic and the complete winter season. However, the sensitivity analysis in section 3.4 confirms that at least the regression is stable in time from year to year. Depending on the used training period, over FYI slope and intercept of the regression cover a range between -474 and 18.7 cm and -649 and 20.0 cm, respectively. Over MYI slope and intercept vary over a range between -227 and 17.3 cm and -413 and 22.3 cm, respectively. This variability in the regression coefficients leads to an estimated uncertainty of the AMSR-E/2 snow depth up to 6 cm over FYI and up to 9.4 cm over MYI. Willmes et al. (2014) investigated the spatial and seasonal variations of the snow emissivity in the Arctic and Antarctic due to snow metamorphism. They found that spatial differences are rather small and only of importance at the onset of melt. However, the seasonal evolution of the snowpack, for example, the densification or grain size growth, influences the observed signal (e.g., Markus and Cavalieri, 1998; Willmes et al., 2014).

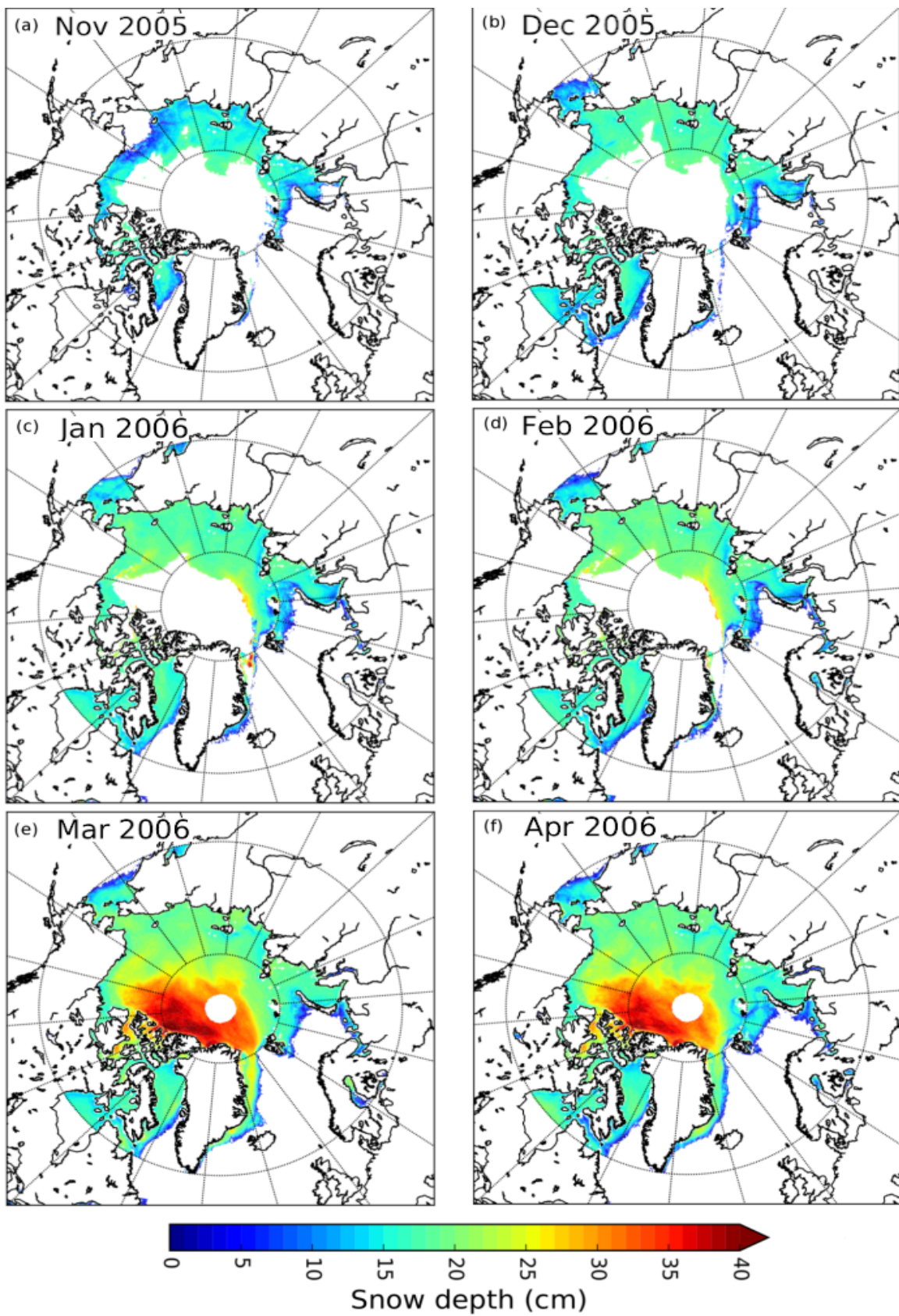


Figure 3.16: Monthly averaged snow depth from November (a) to April (f) for winter season 2005/2006.

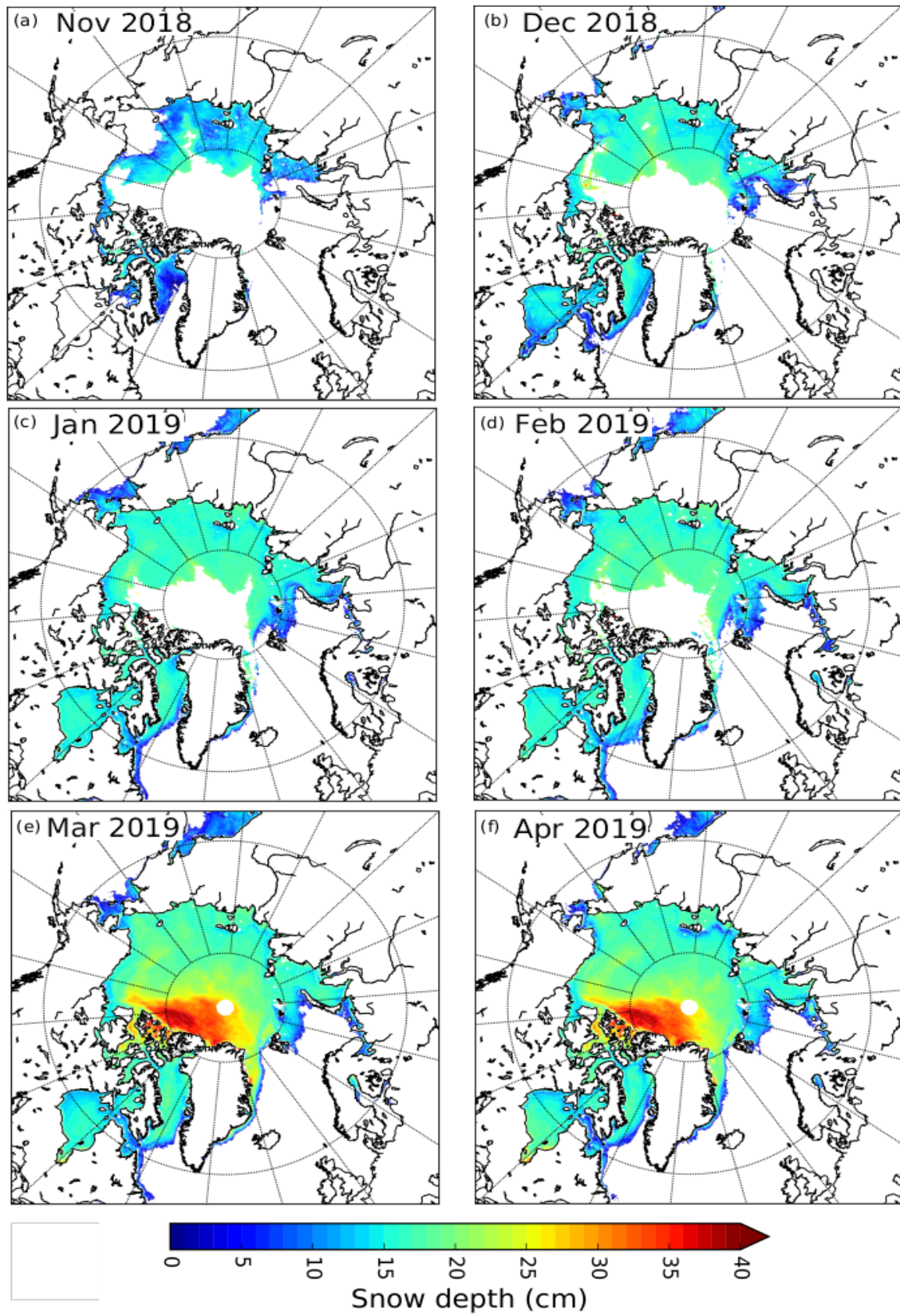


Figure 3.17: Monthly averaged snow depth from November (a) to April (f) for winter season 2018/2019.

Especially in late winter/spring the grain size of the Arctic snowpack increases (Willmes et al., 2014). This leads to a stronger scattering of radiation and thus to a reduced brightness temperature (Markus and Cavalieri, 1998). The effect is stronger for higher frequencies decreasing the GR and hence increases the retrieved snow depth. For the 6.9 GHz channel it is expected that snow metamorphism has a small influence since its emitting layer is at the snow/ice interface over FYI and the snow grains are too small to cause significant scattering (see Figure 2.6). The 19 GHz channel is, however, influenced by the snow and snow grain growth will lead to a reduction of the observed brightness temperature at this frequency. This implies that the regression coefficients derived here, which are based on snow depth measurements in March and April, could lead to an overestimation of snow depth over FYI in early winter with smaller grain sizes due to the influence of the grain size on the microwave emission. This is also partly reflected in the regression coefficients found here: the new AMSR-E/2 retrieval intersects the 0 cm snow depth line at a GR(19/7) value of 0.035. However, the typical emissivity of bare FYI in winter is 0.92 at 7 GHz and 0.95 at 19 GHz (Onstott et al., 1987). The resulting GR(19/7) is 0.017, which, using the derived regression coefficients (equation 3.3), would result in a snow depth of 9 cm instead of 0 cm. In order to validate the retrieval for the whole season, large-scale in-situ measurements from early winter are crucially needed.

For snow on land it has been suggested to use the temperature gradient between the snow surface and the snow/ground interface as a proxy for snow metamorphism in the retrieval (Josberger and Mognard, 2002). This could be part of further research in order to improve the algorithm developed here and to deal with the limitations discussed above. Since large-scale in-situ measurements of snow on Arctic sea ice are rare in early winter, thermodynamic snow models could be used to investigate the seasonal evolution of the snow cover. Recent improvements in snow modelling and reanalysis data (Liston et al., 2018) show promising results when modelling the snow (and its metamorphism) on Arctic sea ice. In addition, state-of-the-art thermodynamic snow model SNOWPACK for snow on land applications (Bartelt and Lehning, 2002) was recently adapted to sea ice, but further development is still needed before it can be fully evaluated (Wever et al., 2019).

Over MYI, the situation is more complicated. The properties of MYI (almost salt free, lower density, more porous) allow microwaves to penetrate through the upper decimeters of the ice (Ulaby and Long, 2014b). The position of the emitting layer depends on the ice properties and the frequencies. Assuming a temperature of -10°C the penetration depth for 7 GHz in MYI is about 1 m. For 18.7 GHz the penetration depth is several tens of centimeters (Ulaby and Long, 2014b). As shown in chapter 2, at 7 GHz dry snow is transparent. Thus, in the case of MYI with dry snow on top, the observed brightness temperature at 7 GHz will only depend

on the MYI properties. However, when the snow becomes wet or thick depth hoar forms at the snow ice interface, the 7 GHz signal will be influenced (see Figure 2.6). At 19 GHz fresh snow with small grains is almost transparent. However, when the snow ages and the grains grow, scattering in the snow becomes an important contributor to the observed signal. The observed brightness temperature over snow on MYI at 19 GHz is a mixture of contributions from MYI and snow. This could indicate why GR(19/7) shows a reasonable correlation to snow depth measurements in spring, after the snow has undergone some metamorphism. At this time of the year the signal of snow seems to dominate the signal of the underling MYI. Only if this is the case, a reliable relationship between GR(19/7) and snow depth on MYI can be expected.

Although the results (Figure 3.7, left and Figure 3.8, right) show that the AMSR-E/2 retrieval based on GR(19/7) over MYI performs not as reliable as over FYI, it still has capability in retrieving the expected snow depth distribution over MYI, at least in March and April and with larger uncertainty. In order to fully retrieve snow depth over MYI the results suggest that more research is required to investigate the influence of MYI on GR(19/7), and detailed measurements of MYI properties and knowledge about its influence on the snow/ice emissivity are needed. The latter could be obtained from microwave emission models (e.g., Dupont et al., 2014; Picard et al., 2018; Tonboe et al., 2006) if they can be used in conjunction with ice core measurements that include measurements of MYI density and salinity as well as the size distribution of the included air bubbles in MYI and coincident snow property measurements. While a lot of MYI ice core data exist for late winter and spring (Shokr and Sinha, 1999), MYI samples from early winter season are rare. However, the latter are critical in order to understand how the microwave emission of MYI evolves in time. Additionally, large-scale in-situ (or airborne) snow depth measurements over MYI are also needed from early winter in order to evaluate the retrieval results. The ongoing year-long MOSAiC campaign (<http://www.mosaic-expedition.org>, accessed 15 May 2017) provides an opportunity to fill this gap.

3.6 Conclusions

Based on five years of SLF snow depth observations, a new empirical passive microwave snow depth retrieval was developed (equations 3.3 and 3.4). For the retrieval, a similar method was applied as developed by Markus and Cavalieri (1998), but using lower frequency channels (6.9 GHz and 18.7 GHz). Over FYI and MYI the results of the regression analysis (section 3.2) show that GR(19/7) works best to derive snow depth (Figure 3.3). The corre-

lation between GR(19/7) and SLF snow depth is -0.73 for FYI and -0.57 for MYI. The RMSD is lower for FYI (3.71 cm) than for MYI (5.48 cm).

An uncertainty analysis based on the uncertainty due to the limited sample size and a Gaussian error propagation of the uncertainties of parameters contributing to GR(19/7) was performed (see section 3.3). The average uncertainty of the AMSR-E/2 retrieval over FYI is between 0.1 and 6 cm, depending on the snow depth. Over MYI the uncertainty ranges between 3.4 cm and 9.4 cm. It is, however, important to note that for individual grid cells uncertainty can be higher, for example, due to ice surface roughness (Stroeve et al., 2006) or strong snow metamorphism.

An evaluation of the retrieved snow depth with SLF measurements from 2015 (section 3.4) shows good results for FYI. A mean difference between retrieval and measurements of -2.1 cm was found, with 93% of the differences being smaller than 5 cm (Figure 3.7, left). For comparison, using the coefficients of the snow depth retrieval from NSIDC only 55% of the differences are below 5 cm. This is slightly worse than what Brucker and Markus (2013) found. They compared the traditional snow depth satellite retrieval based on GR(37/19) to SLF snow depth measurements between 2009 and 2011. They found an agreement of the mean SLF snow depth and satellite retrieved snow depth with 64% of the retrieved values being within ± 5 cm and 89% within ± 10 cm. For single grid cells they found differences up to 21 cm and -35 cm. For the new AMSR-E/2 retrieval, the differences of single grid cells do not exceed 8 cm and -12 cm. Compared to their result, a remarkable improvement was found in this study (see above) using the newly derived regression coefficients and an updated SLF product.

When this study was published (Rostosky et al., 2018), it was the first time to derive Arctic wide snow depths from passive microwave including observations over MYI in March and April. 56% of the differences between the satellite-retrieved MYI snow depth and SLF snow depth are smaller than 5 cm (Figure 3.7). However, over MYI the current version of the AMSR-E/2 snow depth retrieval is limited to spring. The influence of the MYI signal on the observed brightness temperatures is visible in the seasonal evolution of the snow depth, which hampers the MYI snow retrieval for the complete season (Figure 3.9). Considering these results, the retrieval of snow depth over MYI throughout the winter growth season requires additional evaluation. It is therefore recommend that the application of the AMSR-E/2 retrieval over MYI is limited to the months of March and April when the SLF snow depth measurements used for the algorithm development are available and a clear benefit of the retrieval over MYI can be demonstrated.

Besides the improved performance, there are several additional advantages and some disadvantages to using lower frequencies for snow depth retrievals from passive microwave

measurements. Measurements at lower frequencies are less influenced by thaw/refreeze cycles or snow metamorphism such as the development of depth hoar or by weather effects (Powell et al., 2006). On the other hand, lower frequencies are less sensitive to fresh, shallow snow, which leads to disadvantages of the here derived AMSR-E/2 retrieval in early winter where mainly freshly fallen snow with small grains is present. In addition, at lower frequencies also the spatial resolution of the satellite sensor decreases. For example, the mean spatial resolution is 21 km for the 19 GHz channel and 56 km for the 7 GHz channel for AMSR-E. The coarser resolution can be a disadvantage in case of the need of snow depth values at small scales (e.g., for field studies). However, one major aim is to provide a snow on sea ice product, which can be used for climate studies, for the comparison to coupled Arctic climate models, and for ice thickness retrieval from altimeters. For these applications the lower spatial resolution of the new retrieval is less of an issue.

With this new retrieval it is possible to provide a time series of snow depth for the complete Arctic from 2002 until today, limited to March and April over MYI. It can, for example, be used to assess interannual variability of Arctic snow depth, which is not possible with the Warren snow depth climatology (Warren et al., 1999). Figure 3.10 and 3.11 demonstrate that on average, the climatology values are higher than the snow depth retrieved by the AMSR-E/2 product. In single years, the differences between the climatology and the AMSR-E/2 snow depth can be greater than 10 cm. The additional information provided by the satellite retrieval can be helpful for the evaluation of reanalysis data from climate models. In addition, the snow depth can be used for sea ice thickness retrieval based on altimetry, where snow depth is one of the major uncertainties (Kern et al., 2015).

Based on a timeseries of 16 years (2002 to 2019), a negative trend in monthly averaged snow depth is found in both, November (-0.2 cm/year) and March (-0.27 cm/year).

Chapter 4

Uncertainty Estimation

In the previous chapter, a new passive microwave snow depth on Arctic sea ice retrieval was presented including a first uncertainty estimation based on a Gaussian Error Propagation (GEP) model. This model, however, assumes that the covariance of the individual uncertainties of the contributing parameters is zero. This is not necessarily the case for the satellite observations used in this study. Furthermore, satellite observations are not only influenced by the parameters investigated in the GEP but also other parameters like ice- and snow properties, atmospheric properties and clouds influence the observed signal. Therefore, a more detailed uncertainty estimation of the new retrieval is needed.

In the following study, a Monte-Carlo model is used to estimate the uncertainty in the snow depth retrieval introduced by the influence of the above mentioned parameters. The advantage of the Monte-Carlo model over the GEP model is that it allows an error covariance different from zero (Christos and Hoi, 2001). In addition, for Arctic conditions, the above mentioned parameters are often not known. In contrast to the GEP model, the Monte-Carlo method only needs statistical information about the distribution of the influencing parameters. These can be derived from in-situ measurements or climatologies. Most of the results presented in this chapter are already published in Rostosky et al. (2020).

This chapter is organised as follows. In section 4.1, an overview about the models and datasets used in this study is given. In section 4.2, the experimental setups and the most important results are provided. In section 4.3, the application of the results on passive microwave snow depth retrievals is discussed and applied to the retrieval developed in chapter 3 in section 4.4. The paper closes with a conclusion in section 4.5.

4.1 Data and Models

In this section, the models and the datasets are described which are used in this study. The Microwave Emission Model for Layered Snowpack (MEMLS; Wiesmann and Mätzler, 1999), adapted to sea ice (Tonboe et al., 2006) is used to simulate the surface microwave emission of snow on sea ice in dependence of the ice and snow properties (see Section 4.1.2). For estimating the influence of the Arctic atmosphere and Arctic clouds on the GR signal, the Passive and Active Microwave TRANSfer model (PAMTRA) is used (see Section 4.1.4). Besides snow depth, other snow properties like grain size or grain type influence the GR, the grain type cannot be measured from space. In order to evaluate the complex relation between snow metamorphism and changes in the microwave emission of the snowpack, the thermodynamic snow evolution model SNOWPACK is used (Bartelt and Lehning, 2002; Lehning et al., 2002a,b; Wever et al., 2019). All models need geophysical parameters as input data. In this study, snow, ice and atmospheric measurements obtained during the N-ICE2015 campaign (Cohen et al., 2017; Granskog et al., 2016; Rösel et al., 2018b) are used as reference and input data for the models (section 4.1.1). The following sections provide an overview about the models and the N-ICE2015 datasets.

4.1.1 N-ICE2015 data

The Norwegian Young ice cruise (N-ICE2015) took place from January to June 2015 north of Svalbard and in the Fram Strait, led by the Norwegian Polar Institute (Granskog et al., 2016, 2017). During the campaign, the ship was attached to four different ice floes and drifted along with them. Figure 4.1 shows an ice concentration map with the drift trajectories of the first three floes for time periods used in this study. In this study the focus will be on the measurements from the first two floes and parts of the third floe, which cover the time period from 20 January 2015 to 18 March 2015 (floe one and two) and from 19 April 2015 to 13 May 2015 (first part of floe three). During later measurements on the third and fourth flow, the air temperature was often close to the freezing point and the snowpack became wet and slushy. Under this conditions, the relation between GR and the snow depth diminishes (see chapter 2).

During the first and second floe, a winter regime with cold temperatures and moderate winds dominated. However, several storms crossed the measurement site advecting warm and moist air (Cohen et al., 2017; Graham et al., 2017, 2019). During these storms, the air temperature rose close to the freezing point and even above, which likely led to strong snow metamorphism. Figure 4.2 shows the timeseries of the 2 m air temperature and 10 m wind speed measured during the first two sections of the cruise from 22 January 2015 to 18 March

2015. The storm events (e.g., 05 or 15 February) are clearly visible in an rapid increase in wind speed and high temperatures.

The N-ICE2015 snow conditions are described in Merkouriadi et al. (2017a). Snow pits were taken on FYI and SYI (second year ice) floes, however, the snow properties were similar on both floes. The snow pit measurements include snow temperature, density, grain size (maximum and minimum grain diameter) and grain type observations (based on Sommerfeld and LaChapelle, 1970). For some snow pits also specific surface area (SSA) derived from the IceCube instrument are available. All snow measurements were taken in the vicinity of the atmospheric measurements. Overall, for the time-period considered here, 28 snowpits can be used as input data for MEMLS. Table 4.1 shows the average snow properties of these snow pits, relevant for microwave scattering. One important property used in MEMLS is the exponential correlation length (e_{corr} , see chapter 2), which is related to the snow microphysics and controls the amount of microwave scattering in the snowpack. If SSA measurements are available, e_{corr} is calculated using the following equation (adapted from Mätzler, 2002):

$$e_{corr} = 0.75 * \frac{4 * (1 - \phi)}{\rho_i * SSA} \quad (4.1)$$

In equation 4.1, ρ_i is the ice density and ϕ is the ratio between the measured snow density and ice density. Overall, SSA measurements were available for 4 snow pits. If no SSA measurements are available, it is possible to relate e_{corr} to the optical grain size (Grenfell and Warren, 1999; Mätzler, 2002). However, the grain size measured during N-ICE2015 is related to the maximum grain size (D_{max}) and can only be linked to e_{corr} in case of spherical grains. Mätzler (2002) provided a look up Table for estimating e_{corr} from snow grain type, density and D_{max} observations. This Table, however, was compiled for alpine snow and therefore the combination of the relevant parameter obtained from the N-ICE2015 snow pits could not always be related to a specific e_{corr} .

Table 4.1: Mean snow Temperature (T), depth (Sd) density (ρ) and exponential correlation length (e_{corr}) and their standard deviation of the 28 snow pits used from the N-ICE2015 campaign between the 22 January and 13 May 2015 (Merkouriadi et al., 2017b).

T (°C)	-11.15 ± 5
Sd (m)	0.45 ± 13
ρ (kg/m ³)	324 ± 43
e_{corr}	0.139 ± 0.03

4.1.2 Microwave Emission Model of Layered Snowpacks

The Microwave Emission Model for Layered Snowpacks (MEMLS) was developed by Wiesmann and Mätzler (1999). The main objective of this model is to simulate the emissivity, transmissivity and brightness temperature of a given snowpack for horizontally and vertically polarized microwaves. The scattering of microwaves in the snowpack is calculated using the improved Born approximation (IBA). In the IBA, the scattering in the snow is related to an exponential correlation length e_{corr} (Mätzler, 1997, 1998; Mätzler and Wiesmann, 1999). A detailed description of the theory is given in Chapter 2.

The basic idea of the IBA is to treat the snow as a two phase medium consisting of air and ice. Due to the different permittivity of air and ice, microwaves will be scattered during the propagation through the snow. The strength of the scattering depends on the wavelength and on the snow microstructure, the latter can be represented by an auto-correlation function (e.g. Proksch et al., 2015; Wiesmann et al., 1998). The exponential correlation length describes the length scale which is obtained by approximating the auto-correlation function by an exponential fit (adapted from Proksch et al., 2015):

$$C(\vec{r}) = C_0 * \exp\left(\frac{-|\vec{r}|}{e_{corr}}\right) \quad (4.2)$$

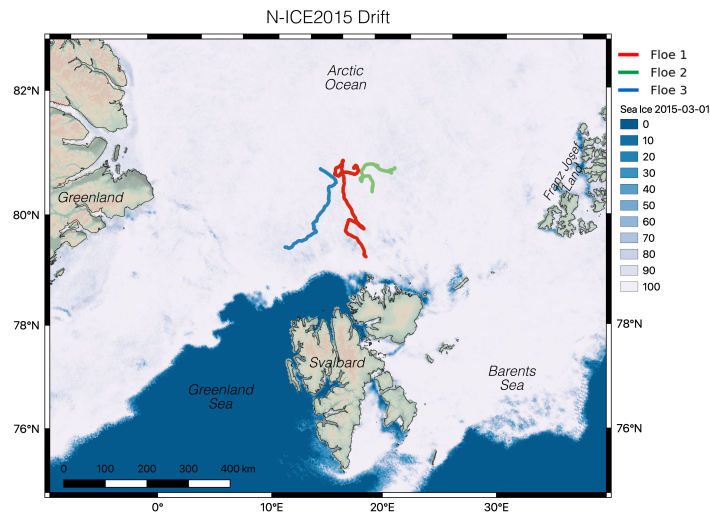


Figure 4.1: Sea ice concentration from 01 March 2015 derived from the ASI sea ice retrieval (Spreen et al., 2008). The colored lines show the drift trajectories of the N-ICE2015 campaign for the first floe (red; 20 January to 21 February 2015), the second floe (green; 24 February to 18 March 2015) and the third floe (blue; 19 April to 13 May 2015). This Graphic was provided by G. Spreen.

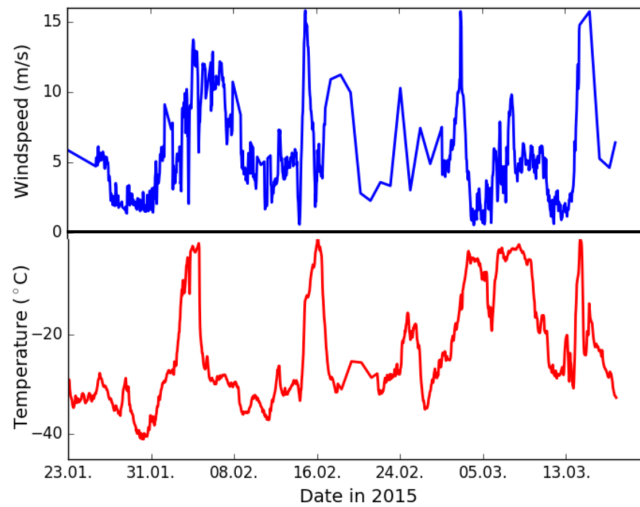


Figure 4.2: 2 m air temperature (bottom) and 10 m wind speed (top) measured during the first part of N-ICE2015 campaign.

In equation 4.2, $C(\vec{r})$ is the auto-correlation function of the lack distance \vec{r} , representing the snow microstructure. The IBA was found to be an accurate approximation for scattering in snow when the optical grain size is large compared to the wavelength of the microwaves (Wiesmann and Mätzler, 1999) and is valid for microwave ranges from 5 GHz to 100 GHz (Mätzler and Wiesmann, 1999). The traditional method to estimate e_{corr} from a snowpack is an empirical derived relation between e_{corr} , the density of snow and pure ice and the SSA (equation 4.1). MEMLS was developed for snow on land and was later adapted to sea ice (Tonboe et al., 2006). A detailed description of the physical background of MEMLS is given in Chapter 2. In the sea ice version of MEMLS, the model in addition calculates the permittivity of sea ice as a function of brine and the microwave scattering in the sea ice based on the IBA. In the version used here, a differentiation between FYI and MYI is implemented. In FYI, the scattering is controlled by brine pockets, while for MYI air bubbles are the main scatterers, since the volume of air in MYI is much higher than the volume of brine. For both ice types, e_{corr} is, together with the inclusion volume, the most important parameter relevant for microwave scattering.

4.1.3 The SNOWPACK Model

The SNOWPACK model was developed to simulate the thermodynamic evolution of snow (Bartelt and Lehning, 2002). The model relates thermodynamic processes in the snow, introduced by e.g., temperature gradient driven metamorphism or wind driven densification to changes in the snow microstructure. The model is driven by external forcings and can calculate snow accumulation, melting and metamorphism from atmospheric measurements

(Lehning et al., 2002a). The model has a very detailed and complex snow microstructure scheme (Lehning et al., 2002b) using grain parameters like dendricity, sphericity, bond radius, grain size and a so called marker which links previous snow metamorphism to a given snowpack. These parameters, however, cannot be easily determined from field measurements. In Lehning et al. (2002b) an overview of the relation between the above mentioned grain parameters and classical grain size and grain type observations is provided. The dendricity of the snow grains is strongly linked to the snow age and state of metamorphism. New fallen snow has a dendricity close to one while strongly metamorphed snow with faceted snow grains or depth hoar has a dendricity close to zero. The sphericity of new snow is 0.5 and can increase or decrease depending on the environmental conditions within the snowpack (e.g., temperature gradients or snow wetness).

In their paper, the authors provide a look up table to estimate the dendricity and sphericity of a given snowpack from traditional grain type and grain size observations. So far no routine method exists to estimate the bond radius from traditional snow pit observations. Here the lookup table provided by the SNOWPACK developers (see <https://models.slf.ch/p/snowpack/page/Starting-from-profiles/>, accessed 15 December 2018) is used. With the additional use of the lookup table, the N-ICE2015 snow pit measurements contain sufficient information so that the measured snow properties can be converted to the parameters relevant for SNOWPACK. Recently, SNOWPACK was adapted to sea ice (Wever et al., 2019) including sea ice relevant processes such as thermodynamic ice growth, flooding and heat transport between the ocean/ice and snow. The model is still in the development phase. The version used here is the latest SNOWPACK sea ice release (status 10 December 2019).

4.1.4 The PAMTRA Model

In this study the Passive and Active Microwave TRAnsfer model (PAMTRA, from <https://github.com/igmk/pamtra>, accessed: 01 November 2018) is used to simulate the radiative transfer of microwave radiation through the atmosphere. The description of the model was originally provided by M.Mech (April 2019) and was only slightly modified for this chapter. PAMTRA is a framework written in FORTRAN90 and python for the simulation of the transfer of passive and active radiation in a plane-parallel, one-dimensional, and horizontally homogeneous cloudy atmosphere. PAMTRA makes use of the RT4 model by Evans (1995), which applies the doubling and adding method to solve the passive radiative transfer. It is limited to the microwave frequency between 1 GHz and up to 1 THz. With PAMTRA, it is possible to simulate up- and down-welling radiation at any height and observation angle. The model provides radiances or polarized brightness temperatures. The atmospheric input to PAMTRA can be artificial, from radiosondes or any other profiling in-situ measurement.

For the calculation of the interaction parameters between radiation and atmosphere or ground, the model utilizes well known and established methods and modules created by various authors and publicly available. The gaseous absorption for oxygen, water vapor, and nitrogen is by default and in this study calculated by the Rosenkranz 98 absorption model (Rosenkranz, 2015) including recent modifications of the water vapor continuum absorption presented in Turner et al. (2009) and the line width modification of the 22.235 GHz H₂O line as proposed by Liljegregd et al. (2005). An unlimited number of hydrometeor types can be described by different implemented particle size distributions. The parameters to these distributions can be adjusted so that the microphysical assumptions in the radiative transfer are consistent with the one made in the input source, i.e., the atmospheric models. Single scattering and absorption properties for the hydrometeors can be calculated by various methods. These include the cost effective Mie theory and the more time consuming T-Matrix theory by Mischenko and Travis (1994).

PAMTRA allows as well the use of scattering databases that are usually created by applying the Discrete Dipole Approximation Method (DDA). For aggregates or more complex particles, PAMTRA also includes a very recent approximation called the self-similar Rayleigh-Gans Approximation (SSRGA; Hogan et al., 2017; Hogan and Westbrook, 2014) that is rather cost effective compared to DDA calculations. For the lower boundary the reflectivity and emissivity properties have to be provided. For ocean this can be done by the Tool to Estimate Sea-Surface Emissivity from Microwaves to sub-Millimeter waves (TESSEM2; Prigent et al., 2017) that is built around the community model FAST microwave Emissivity Model (FASTEM; Liu et al., 2011). For land surfaces the Tool to Estimate Land Surface Emissivity from Microwave to Submillimeter Waves (TELSEM2; Aires et al., 2011; Wang et al., 2017) has been implemented which provides the emissivities based on geographic location and month derived from satellite measurements.

4.2 Results

4.2.1 Influence of the Ice Properties

For microwave observations, it is important to distinguish between Arctic FYI and MYI since they have different microwave signatures. Here, the focus is on how the natural variability of the ice properties influences the GR. For this purpose, a 1000 member Monte-Carlo simulation is performed. The snow depth is increased in 2 cm steps from 10 cm to 70 cm. A simplified snowpack is used, consisting of two layers. The snow properties of each layer are summarised in Table 4.3. A linear temperature profile is assumed in the snow in such a way

that the temperature at the snow-ice interface is always -13°C . The ice thickness is set to 2 m and split into 2 cm thick layers. For each snow thickness, 1000 simulations for both FYI and MYI are performed and in every individual simulation the ice properties are randomly varied around their mean values \pm the standard deviation given in Table 2. The reference values for the ice density are obtained from Shokr and Sinha (1999) and Fung and Eom (1982). The exponential correlation length and its standard deviation for MYI were calculated based on the air bubble diameters found by Shokr and Sinha (1999) using the same method as for the snow (Mätzler, 2002). However, as discussed in Chapter 2, this relationship is only valid under the assumption of a two-phase medium (i.e., no brine) and spherical inclusions (i.e., only air bubbles are considered). While microwaves can only travel a few cm into FYI, they can travel up to 1 m in MYI (Ulaby and Long, 2014b) due to its low salinity. Therefore, volume scattering in MYI is important and the estimated volume scattering in MYI may be inaccurate due to the above mentioned simplifications (see Chapter 2).

Table 4.2: Mean snow and sea ice density (ρ), salinity (S), exponential correlation length (e_{corr}), temperature (T) and superimposed layer depth (d_{SSI}) and their standard deviations used for the sensitivity study. The sea ice properties are obtained from (Fung and Eom, 1982; Grenfell, 2015; Shokr and Sinha, 1999)

	FYI	MYI	snow top	snow bottom
ρ (kg/m^3)	910 ± 8	800 ± 81	290	310
S	$5 \text{ to } 8 \pm 0.81$	0 ± 0.81 (S > 0)	0	0
e_{corr}	0.15 ± 0.07	0.28 ± 0.07	0.11	0.13
d_{SSI} (cm)	0	0.40 ± 0.31		
T (K)	± 1	± 1		

Figure 4.3 shows the results of the Monte-Carlo simulation for GR(19/7) (left) and GR(37/19) (right) for FYI (blue) and MYI (red). The thick line represents the mean over the 1000 simulations and the error bars the standard deviation. For visualisation purpose, the error bars are displayed every 10 cm. In addition, the resulting error for potential snow depth retrievals (%) is shown. This error is calculated as follows: first a simple linear regression model is used to retrieve a theoretical snow depth (Sd_n) using equation 3.1 and the averaged GR. A second snow depth (Sd_e) is derived including the standard deviation to the GR for every snow depth. The error shown in Figure 4.3 the normalized RMSD (NRMSD) between Sd_n and Sd_e .

For FYI the influence of the ice properties on the GR is very small and the error is only 2% for both GR. For MYI, the influence of the ice properties on GR(19/7) remains small (standard deviation is between 0.00036 and 0.00042), and, more important, is smaller than its

sensitivity to snow depth (roughly 0.003/10 cm). The error due to changes in ice properties is around 8% of the actual snow depth. For GR(37/19), the influence of the MYI properties is one magnitude larger than for GR(19/7) and the potential error due to the variability of MYI properties is 29%. This is consistent with earlier findings that GR(37/19) cannot be used to retrieve snow depth for MYI, since the signal of the MYI at GR(37/19) is of similar strength to the signal of snow (e.g. Brucker and Markus, 2013; Rostosky et al., 2018).

In Chapter 3, a reasonable correlation between GR(19/7) and snow depth on MYI was found, indicating that it is possible to derive a retrieval for snow depth on MYI using this gradient ratio, even though the correlation between it and snow depth was lower for MYI than for FYI and high errors were found for MYI. Also the results found in this study indicate that MYI properties have only little influence on GR(19/7). However, the lower correlation and increased error between GR(19/7) and snow depth on MYI found in Chapter 3 is not visible in the modelled results shown here. This can have several reasons. The influence of large scale roughness (e.g., from pressure ridges) on the GR is not considered here. However, this roughness has a strong impact on the GR, especially at lower frequencies (Worby et al., 2008). Second, the implementation of MYI in MEMLS is simplified in a way that it is considered as an two-phase media consisting of air and ice. The influence of brine on the scattering is neglected in the model, which could lead to an underestimation of the scattering in MYI.

While the focus of the other experiments is based on the N-ICE2015 datasets, for the ice properties, only a few ice core measurements over MYI were taken. The variability of ice properties from the N-ICE2015 observations is smaller than the values found in literature. For the MYI, the mean density and variability of the ice is around $850 \text{ kgm}^{-3} \pm 50 \text{ kgm}^{-3}$. The salinity of the top layers vary between 0 ppt and 2 ppt, which is similar to the values used in this study. No estimation of the air-bubble size distribution for the N-ICE2015 cores was performed so far. However, using the same e_{corr} but the density variability based on MYI cores from N-ICE2015, the NRMSD between Sd_n and Sd_e is $\pm 6\%$ for GR(19/7) and $\pm 24\%$ for GR(37/19). The variability in the FYI properties is low compared to the variability of MYI properties. To test if the low NRMSD obtained for FYI is only a result of this low variability, the variability of the FYI properties are artificially increased to $\pm 50 \text{ kgm}^{-3}$ for the density and to ± 0.25 for e_{corr} . This added variability, however, only increased the NRMSD by below 1%.

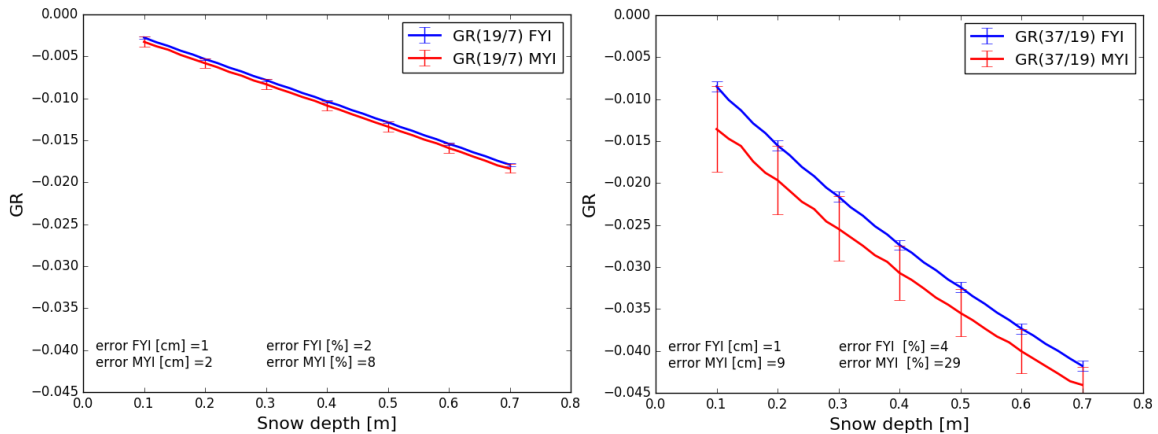


Figure 4.3: Sensitivity of GR(19/7) (left) and GR(37/19) (right) to FYI properties (blue) and MYI properties (red). The thick line represents the mean over the 1000 Monte-Carlo simulations and the errorbar the standard deviation. In addition, the mean error of potential snow depth retrievals is shown.

4.2.2 Influence of the Atmosphere

As described in section 4.1.4, PAMTRA is used to investigate the influence of the atmosphere and clouds on the GR. The model is forced with radiosonde measurements of the atmospheric temperature, humidity, wind speed and air pressure obtained during the N-ICE2015 campaign (Hudson et al., 2017). For the sensitivity study, the same snowpack as described in section 4.2.1 is used.

Overall, 258 simulations were performed based on all available radiosonde profiles obtained during the N-ICE2015 campaign. Clouds cannot be directly measured by radiosondes. However, since clouds can have a strong impact on the GR, the cloud liquid water content (CLW) in the atmosphere was estimated using the modified adiabatic cloud model proposed by Karstens et al. (1994). Overall, based on this model, clouds were detected in 77 out of 258 profiles with an average CLW of 0.29 kg m^{-2} . Most of the clouds were low level clouds with a cloud base between 500 m and 1000 m and the cloud top was always below 5000 m. Besides clouds, also the total water vapour (TVP) is relevant for microwaves. The mean TVP in this dataset is 4.58 kg m^{-2} with a standard deviation of $\pm 3.18 \text{ kg m}^{-2}$.

Two studies are performed. In the first study, only the influence of the atmosphere on the GR is investigated based on the 258 radiosonde profiles. In the second study, the influence of clouds on GR is investigated based on the 77 radiosonde profiles including the CLW profiles derived from Karstens et al. (1994).

Figure 4.4 shows the influence of the atmosphere and clouds on GR(19/7) (left) and GR(37/19) (right). The blue line shows the mean over all simulations for the cloud free case and the

error bars show the standard deviation of GR for a cloud free atmosphere (blue) and cloudy atmosphere (red). In addition, the mean variability in GR is shown together with the error (%), derived in a similar way as described in Section 4.2.1. For both GR, the influence of the atmosphere is rather low and results in a NRMSD of $\pm 4\%$ for a GR(19/7) and $\pm 3\%$ for a GR(37/19) based snow depth retrieval. The NRMSD due to clouds is $\pm 7\%$ at GR(19/7) and $\pm 24\%$ at GR(37/19). Based on these results, GR(19/7) is less influenced by the atmosphere and clouds, and is therefore more suited to retrieve snow depth over FYI if no atmospheric corrections are applied. The results found here are in good agreement with the results from Markus et al. (2006b) where the authors found a strong influence of the atmosphere and cloud liquid water on GR(37/19) but only a weak influence on GR(19/10).

4.2.3 Influence of the Snow Properties

The snowpack properties observed during the N-ICE2015 campaign show a high variability in space and time (Merkouriadi et al., 2017a). Figure 4.5 shows GR(19/7) (blue) and GR(37/19) (red) for all 28 snowpits calculated using MEMLS. Details about the snow measurements and the initialisation files for MEMLS are given in appendix B.

Although some relation between GR and snow depth is visible (correlation is -0.7 for GR(19/7) and -0.4 for GR(37/19)), the RMSD is very high for both GR (9.7 cm for GR(19/7) and 12.5 cm for GR(37/19)). However, likely these results display the effect of local variability in the snow properties and on the scale of satellite footprints, part of it should average out. Therefore, it is more important to consider how large scale phenomena such as warm air inflow influence the snowpack and consequently the GR.

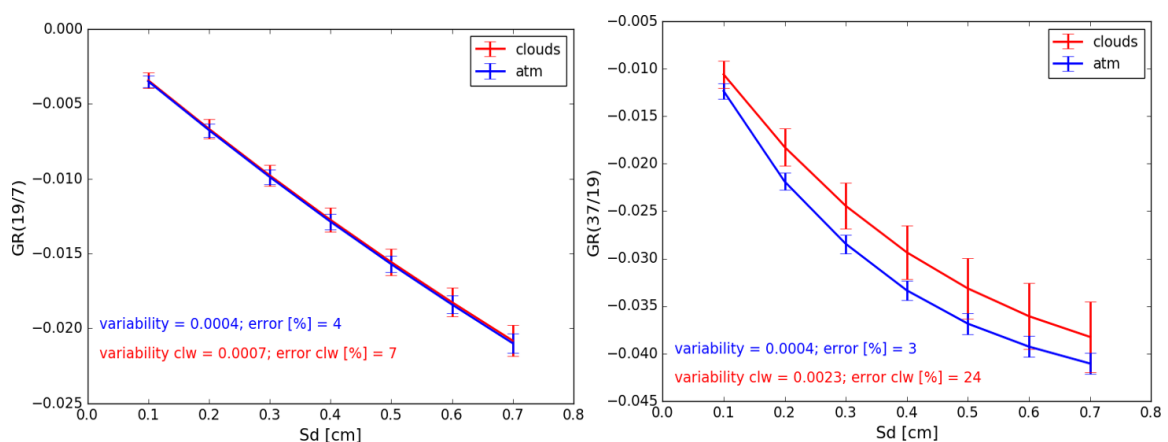


Figure 4.4: Sensitivity of GR(19/7) (left) and GR(37/19) (right) to atmospheric properties and clouds. The thick line represents the mean of all 258 simulations and the errorbar the variability.

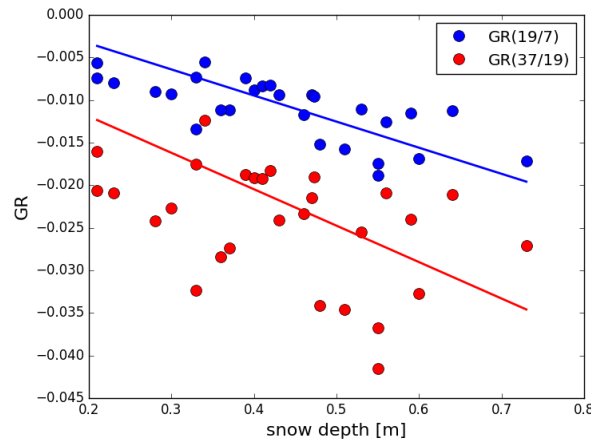


Figure 4.5: GR based on MEMLS simulations of the 28 snowpits used from the N-ICE2015 campaign. In addition, the regression lines are shown.

Cavalieri et al. (2012) showed that warm air intrusions have a strong impact on the snow depth derived from GR(37/19) based snow depth retrievals due to the potential formation of melt/refreeze layers in the snow. Different from previous studies, the extensive observations of ice, snow and atmospheric properties obtained during the N-ICE2015 campaign provide the opportunity to link atmospheric measurement to snow metamorphism using a snow evolution model (SNOWPACK) and to calculate its influence on the microwave signal using MEMLS. During the campaign, several storms crossed the measurement site and advected warm and moist air (Figure 4.2) and therefore likely introduced strong snow metamorphism. Here, a case study is performed investigating the snow metamorphism introduced by the storm event around 05 February 2015 using the thermodynamic snow evolution model SNOWPACK in addition to MEMLS. For this purpose, SNOWPACK is initialised with the N-ICE2015 snow pit measurement obtained on the 23 January 2015 and then run until the 01 March 2015 using the atmospheric observations obtained during the N-ICE2015 campaign. The full initialisation profile is given in Appendix B. As described in section 4.1.3, SNOWPACK needs grain information that were not measured in the N-ICE2015 snowpits and therefore must be estimated from the available grain related measurements.

Figure 4.6 (a) shows the temporal evolution of the snowpack temperature. The initial temperature profile shows a strong negative gradient in the snow which is typical for a cold, Arctic snowpack. Around 05 February, a storm advected warm air into the area and the temperature gradient in the snow changes its sign, rising close to the freezing point at the snow surface. Two days after the storm, the temperature falls again and the temperature profile looks similar to the profile before the storm.

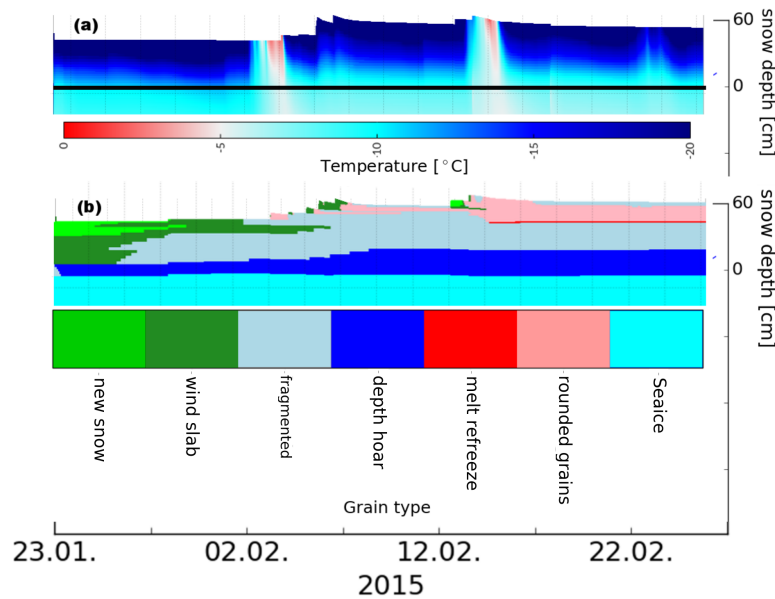


Figure 4.6: Time series of the snowpack temperature in $^{\circ}\text{C}$ (a) and grain type (b) based on a SNOWPACK simulation from 23 January 2015 to 01 March 2015. The black line in (a) marks the snow-ice interface.

Figure 4.6 (b) shows the temporal evolution of the snow grain type. At the beginning, the top layer of the snowpack consists of newly fallen snow (13 cm) followed by a layer of wind slab (27 cm). At the bottom layer, depth hoar (11 cm) exists. From the 25 January to 02 February, the layer of new fallen snow transforms into wind slab and the wind slab layer in the middle of the snowpack transforms into fragmented snow. During the storm (05 February), a layer of rounded grains forms at the top of the snowpack. In contrast to the temperature profile (Figure 4.6), the short period of warm air temperature during the storm has a long term impact on the snow grain type.

In Figure 4.7, the snow type simulated by SNOWPACK is compared to snow type measurements from N-ICE2015 (modified from Merkouriadi et al., 2017b) obtained at 28 January 2015 (snow pit 1, cool conditions before the storm), at 05 February 2015 (snow pit 2, during the storm) and at 13 February 2015 (snow pit 3, cool conditions after the storm). Even though snow pit surveys are destructive and therefore cannot be obtained at the exact same spot relative to the ice floe, they allow a rough comparison with the simulated snowpack to check if the overall snow evolution was modelled correctly. The grain types of snow pit 1 and 2 are in a good agreement with the simulated snowpits. The transformation into a snowpack with predominantly fragmented snow is visible in both data. In the 3rd snow pit a layer of wind slab snow was found while in the model simulations, a 5 cm thick layer of rounded grains has formed at the top of the snowpack.

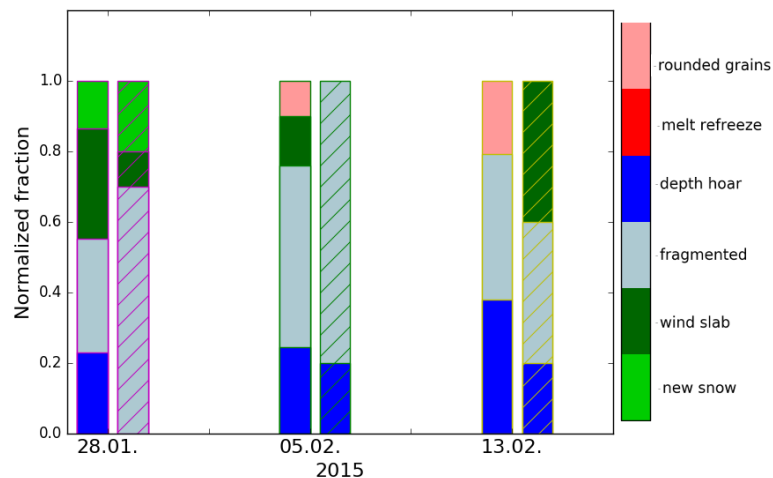


Figure 4.7: Comparison of three distinct grain type profiles simulated with SNOWPACK and the according N-ICE2015 measurements (shaded bars). The edge-colors (i.e., magenta for snow pit 1, green for snow pit 2 and yellow for snow pit 3) are chosen according to the colors in Figure 4.9.

In order to evaluate the influence of the snow metamorphism on the GR, a MEMLS study is set up using the simulated snow profiles by SNOWPACK, (see Figure 4.7) as input data. In order to obtain a full picture, the properties of the simulated snow profiles were scaled to 1 and then transferred to a snowpack varying from 2 cm to 70 cm with 2 cm steps.

In MEMLS, only incoherent scattering is considered (i.e., wavelength larger than $0.5 \times$ layer thickness; Mätzler, 2006), while coherent scattering leads to unphysical model results. In the case of 6.9 GHz and new snow (i.e., no volume scattering), the layer thickness has at least to be 2 cm in order to avoid coherent scattering. Therefore, for the snow type experiment (4.2.3), the scaling of the different snow types slightly varied between each step of the simulation (i.e., from 10 cm to 12 cm) resulting in a step-wise variability in the Monte-Carlo ensemble simulations of the resulting brightness temperatures. Figure 4.8 shows the mean variability of the simulated brightness temperatures for the snow-type experiment. The wavy form of the curves is due to the above described model limitations and has no physical meaning. Since this might influence further calculations, a five point running average is applied to the data to mitigate the problem.

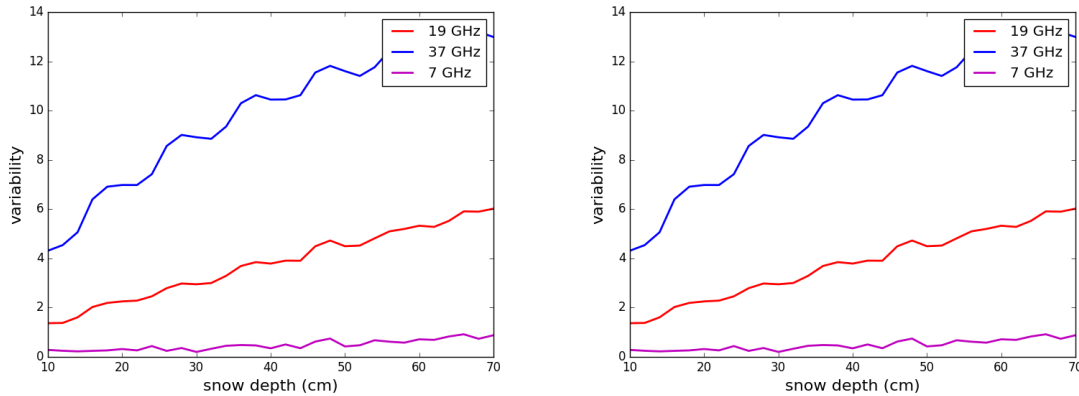


Figure 4.8: Variability of the simulated brightness temperatures in dependence of the snow depth for 6.9 GHz, 18.7 GHz and 36.5 GHz using the Monte-Carlo approach.

Figure 4.9 shows the results of the MEMLS simulation using the above mentioned snow profiles as input for GR(19/7) (left) and GR(37/19) (right). Two additional, artificial snow profiles were added in order to cover a wider range of possible snowpacks. These profiles are similar to profile 1 but contain a fraction of 20% new fallen snow at the top (red curve) or 20% slightly compacted snow (blue curve). These type of snow profiles were not observed during N-ICE2015 campaign. However, the N-ICE2015 snowpack is representative for spring snow conditions, where the snow is compacted and has undergone metamorphism. During the Surface Heat Budget of the Arctic Ocean (SHEBA) campaign, which took place from October 1997 to October 1998, the most predominant snow types observed consisted of predominantly depth hoar, wind slab and fresh snow (Sturm et al., 2002). With the addition of the 2 above mentioned snowpacks, the simulations also cover early winter snow conditions. Both, GR(19/7) and GR(37/19) strongly depend on the snow type (Figure 4.9). Especially the snow pit which was simulated after the storm event (yellow curve) leads to significant lower GR than the snowpits before and during the storm. These simulation should cover a good amount of variability which can be expected over large scales in the whole Arctic. The NRMSD is similar for both GR's and is around 20% for GR(19/7) and 24% for GR(37/19).

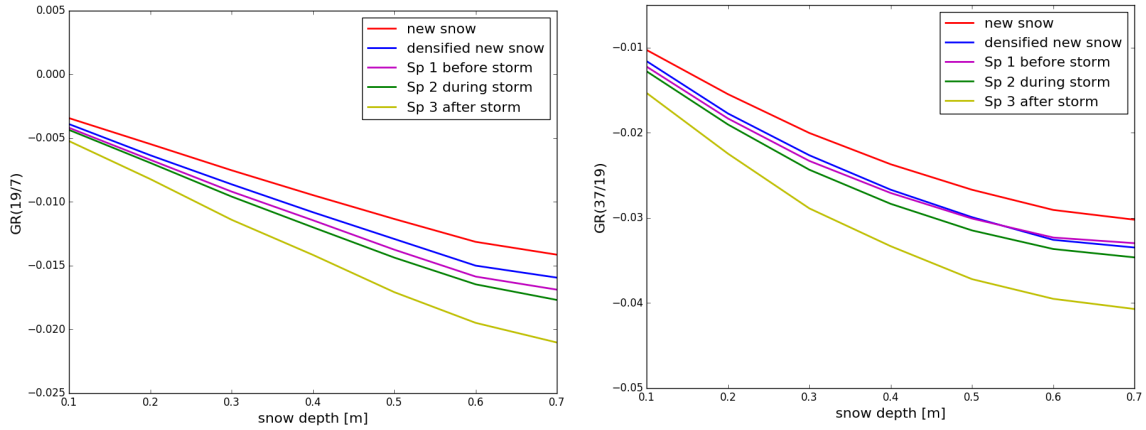


Figure 4.9: GR(19/7), left and GR(37/19), right for five snowpack with different snow properties.

4.3 Uncertainty of Potential Snow Depth Retrievals

From the uncertainties in GR derived in this study, it is possible to estimate the uncertainty of GR-based snow depth retrievals due to unknown state of the atmosphere and unknown snow type. To investigate this, the following study is set up: based on the individual results from each study, a set of 2580 simulations is available, each simulation with slightly different conditions for the atmosphere, clouds and snow type. From these simulations the standard deviation of the GR due to each quantity can be obtained (see Table 4.3). Then, similar to the technique described in Section 4.2.1, a 1000 member Monte-Carlo simulation is performed for a snowpack varying between 10 cm and 70 cm. In each simulation and for each snow depth, a random error between \pm the standard deviation from the three types of uncertainty sources (snow type, atmosphere and clouds) is added to the averaged GR(19/7) and GR(37/19) (in the following called GR_{noise}). Then, a linear regression is performed between GR_{noise} and the snow depth and the regression coefficients are used to retrieve a snow depth. This retrieved snow depth is then compared to the real snow depth. With this method, it is possible to estimate the uncertainty of a snow depth retrieval if no information about the snow type, the state of the atmosphere or clouds are available during the training of the retrieval under the assumption that all quantities vary in the training dataset.

The first two columns in Table 4.4 show the results of the reference regression analysis based on an GR without any uncertainties (in the following called GR_{mean}). Here the NRMSD is related to the error introduced for assuming a linear model.

Table 4.3: Standard deviation of the GR due to the variability in Atmospheric and snow properties as well as clouds.

	GR(19/7)	GR(37/19)
Atmosphere	± 0.0004	± 0.0005
Clouds	± 0.0007	± 0.0023
Snow	± 0.0013	± 0.0026

For GR(19/7), the assumption of a linear relation between GR and the snow depth leads only to small errors ($\text{NRMSD} \leq 2\%$). However, for a GR(37/19) based retrieval, the linear assumption results in a NRMSD of 10% for the snowpack investigated here. This is mainly due to the nonlinear relation between GR(37/19) and snow depths > 50 cm (as can be seen in Figure 4.9, right). The same analysis is performed limiting the snow depth to 50 cm. In this case, the NRMSD for GR(37/19) based retrievals is 4%.

Table 4.4: Regression coefficients and error statistics of GR based snow depth retrievals without $(\text{GR}(v1,v2)_{mean})$, column one and two) and with uncertainties $(\text{GR}(v1,v2)_{noise})$, column three and four) in GR.

	$\text{GR}(19/7)_{mean}$	$\text{GR}(37/19)_{mean}$	$\text{GR}(19/7)_{noise}$	$\text{GR}(37/19)_{noise}$
slope	-3900	-3230	-3300 ± 230	-3150 ± 140
intercept	-30.04	-30.19	0.06 ± 0.03	0.02 ± 0.04
correlation	-0.99	-0.98	-0.99	-0.98
NRMSD (%)	2	10	11	19

The results of the Monte-Carlo simulations including the uncertainties of GR derived in section 4.2 (see Table 4.3) are shown in the third and fourth column of Table 4.4. Here, the mean regression coefficients over all 1000 simulations are shown together with their standard deviation, along with the NRMSD and correlation between the snow depth retrieved from GR_{noise} and the input snow depth. The NRMSD increases in both models to 11% for the GR(19/7) and to 19% for the GR(37/19) based retrieval. These results demonstrate the need for additional data in GR based snow depth retrievals, since otherwise the retrieval has a mean error of at least 11%.

The influence of e.g., sea ice roughness on the GR is not considered in this study. In addition, the training of satellite retrievals will always contain errors due to resolution differences between the satellite observations and the snow depth measurements. Therefore the real error of GR based snow depth retrievals could be higher than the errors found here. On the

other hand the employed models might contain uncertainties, which are not present in the observations.

The variability in the regression coefficients gives an indication about the robustness of the fit. For both retrievals, the standard deviation of the regression coefficients is less than 10% for the slope and 3 cm to 4 cm for the intercept (column three and four in Table 4.4).

The strongest contribution to the NRMSD of the retrieved snow depth is due to the uncertainties obtained from the different snowtypes. Assuming the snowtype is known (e.g., zero uncertainty for the snow type), the NRMSD of the GR(19/7) based retrieval would decrease to 4% which is close to ideal case (i.e., no uncertainties in GR) and for GR(37/19) to 13%. Adding information about the atmosphere leads to an improvement on the results of GR(37/19) reducing the NRMSD to 15%. In addition, the variability in the regression coefficients reduces with a reduced uncertainty in GR.

The results demonstrate that if a GR based snow depth retrieval is trained without adding information about properties influencing the GR, high potential errors in the derived regression coefficients can be the result. However, even if information about snow type and the clouds are available during the training, they also need to be considered during daily retrieval in order to improve the snow depth retrievals (e.g., Cavalieri et al., 2012). Especially a good knowledge of the snow type is crucial for improving GR based snow depth retrievals. For snow on land, studies have shown that it is possible to link snow metamorphism relevant for microwave scattering to the vertical temperature gradient in the snow (e.g., Josberger and Mognard, 2002). Other studies attempt to assimilate observations from measurement data into a thermodynamic snow evolution model for improving satellite borne snow depth retrievals (e.g., Pulliainen, 2006). On sea ice, however, weather observations from stations are rare. Ice mass balance buoys drifting on Arctic MYI can provide atmospheric measurements valid for a small scale around the buoy. For snow on sea ice, the thermodynamic modelling of snow evolution is still part of ongoing work and faces difficulties. Simple relations between the air temperature and the snow metamorphism as derived for snow on land might not be possible due to the sea ice drifting and unknown heat fluxes through the ice causing snow metamorphism at the bottom. If information about the initial snow profile and ice properties are known, thermodynamic snow models (e.g., SNOWPACK) are able to simulate the influence of large scale effects like warm air intrusions on snow evolution as shown in this study. Thus models constrained by observations could provide a way forward for improved satellite retrievals.

Earlier studies suggested to combine GR(19/7) and GR(37/19) to take advantage of their individual strengths (e.g., Markus et al., 2006b). While GR(37/19) has a higher sensitivity to shallow snowpacks but saturates around 50 cm, GR(19/7) is sensitive to snowpacks deeper

than 1 m. Thus a snow depth retrieval using a combination of GR(19/7) and GR(37/19) weighted by their sensitivity would have an increased overall sensitivity to snowpacks at all thicknesses. However, as shown in Table 4.4, GR(37/19) has a higher uncertainty than GR(19/7). Therefore, instead of the sensitivity, the signal-to-noise ratio (STN) should be used:

$$STN = \frac{\delta S}{\sigma^2} \quad (4.3)$$

In equation 4.3, δS is the sensitivity and σ^2 the noise (= variance of the uncertainty). A snow depth retrieval using both GR could then have the form:

$$Sd = Sd_{GR(19/7)} * W_{GR(19/7)} + Sd_{GR(37/19)} * W_{GR(37/19)} \quad (4.4)$$

Here, W_{GR} is the weighing function of the GR based on its STN. The weighing functions fulfil the condition $W_{GR(19/7)} + W_{GR(37/19)} = 1$. Figure 4.10 shows the weighting functions of GR(19/7) (blue) and GR(37/19) (red) for a perfect retrieval (i.e., without uncertainties) and for a retrieval considering the uncertainties in brightness temperatures found in this study (see Table 4.3). Including the uncertainty results in a higher weight for GR(19/7). For lower snow depths, the GR(37/19) based retrieval has the better signal to noise ratio and thus the corresponding weighting function is higher. At a snow depth around 38 cm, both weighting functions are around 0.5 and afterwards, GR(19/7) becomes more important. Table

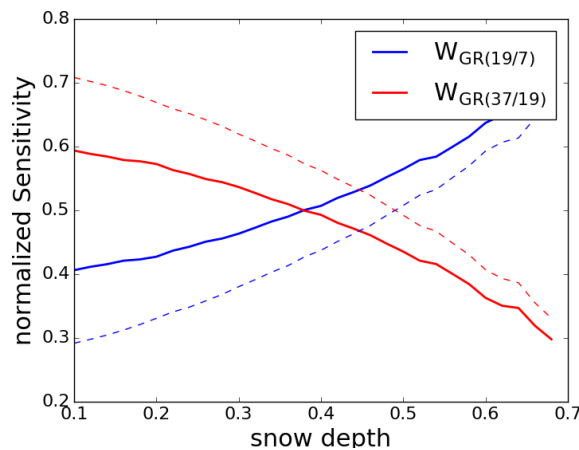


Figure 4.10: Normalised weighting function for GR(19/7), blue and GR(37/19), red. The dashed lines show the weighting functions without considering noise.

4.5 shows the performance of the combined retrieval for the ideal case (no uncertainties) and with included uncertainties. Here, a linear fit was applied to both GRs and to account for the nonlinear relation of GR(37/19) to snow depth, the combined retrieval is limited to snow depth smaller than 50 cm. For higher snow depths, only the GR(19/7) based retrieval is used.

In principle, also a higher order polynomial fit could be used for the GR(37/19) retrieval but polynomial fits perform worse when applied to observational data (see Chapter 3). In the ideal case, the combined retrieval performs slightly better (correlation = -0.98 and RMSD = 1.7%) than the single GR snow depth retrievals. Including the uncertainties, the combined retrieval has the lowest RMSD (= 9.8%) compared to the single GR retrievals.

Over Arctic FYI, the snow depth is mostly below 50 cm (except for the Atlantic sector; Merkouriadi et al., 2017a) and therefore, the combined snow depth retrieval would perform even better compared to e.g., GR(19/7) retrievals since it benefits from the higher sensitivity of GR(37/19) to shallow snow.

Table 4.5: Regression coefficients and error statistics for the combined snow depth retrieval (GRM) without (GRM)_{mean}, column one and two) and with uncertainties (GRM)_{noise}, column three and four) in GR.

	GRM _{mean}	GRM _{noise}
slope	-3900	-1500 ± 140
intercept	-0.04	0.02 ± 0.04
correlation	-0.98	-0.96
NRMSD [%]	1.7	9.8

The results shown here are all based on models and thus subject to assumptions and simplifications. This is particular important for the results shown in Figure 4.5 and Figure 4.9. In order to simulate these brightness temperatures, the scattering parameter e_{corr} had to be estimated from a lookup table (Mätzler, 2002). In addition, thin ice crusts were present in most of the snow pits observed during the N-ICE2015 campaign. However, these ice crusts are not resolved in MEMLS (see Chapter 2). Therefore, the variability of the GR in dependence of the snow type might be too low and the derived uncertainty for GR based snow depth retrievals underestimated. In the simulations for Figure 4.9, the different layers within the snowpack were equally scaled from 2 cm to 70 cm. While this is may not be the most realistic approach, not enough information about the evolution of the Arctic snowpack is available to derive a more sophisticated approach.

4.4 Application to the AMSR-E/2 Snow Depth Retrieval

The uncertainty for potential snow depth retrievals derived in this study can be used to improve the first uncertainty assessment of the new developed snow depth retrieval (see Chapter 3). To estimate the uncertainty of the new retrieval based on the Monte-Carlo model,

the variability in the brightness temperatures derived in this study are applied to the satellite and OIB snow depth datasets used in Chapter 3. It is important to note that the relation between GR and snow depth (i.e., slope and intercept of the regression results) are different in the simulations and satellite observations. The sensitivity of the modelled brightness temperatures to snow depth is higher than the sensitivity of the satellite observed brightness temperatures to OIB snow depth. Therefore, the uncertainty estimated from the Monte-Carlo model might be too low.

Figure 4.11 shows the uncertainty of the snow depth retrieval over FYI derived from the Monte-Carlo model for a GR(19/7) based retrieval (left) and a combined GR retrieval (right) based on equation 4.4, i.e. using the GR(19/7) and GR(37/19) regression coefficients derived in chapter 3 and the weighting functions derived in section 4.3. Overall, the uncertainty derived from the Monte-Carlo model ranges from 4.2 cm at 12 cm snow depth to 8.5 cm at 40 cm snow depth and is higher than the uncertainty based on the Gaussian Error Propagation described in Chapter 3. Especially for low snow depth, the Monte-Carlo model gives more reasonable results, since the uncertainty does not drop to zero for shallow snow. The uncertainty of the combined snow depth retrieval is slightly lower than the uncertainty of the GR(19/7) based snow depth retrieval (Figure 4.11, right).

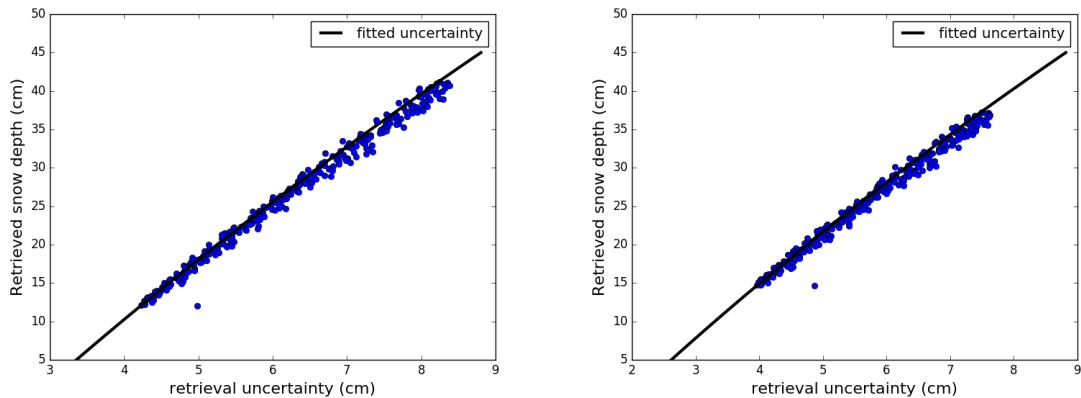


Figure 4.11: Uncertainty of the snow depth retrieval derived in Chapter 3 (left) and for a combined GR(19/7) and GR(37/19) snow depth retrieval (right) over FYI using the Monte-Carlo uncertainty model. The solid line represents a polynomial fit to the data.

Figure 4.12 shows the same as 4.11 but for MYI. Here, the uncertainty ranges from 5 cm at 25 cm snow depth to 10 cm at 50 cm snow depth. For low snow depths, the Monte-Carlo derived uncertainty is higher than the uncertainty based on the Gaussian Error Propagation, while for high snow depths, both methods give similar uncertainties.

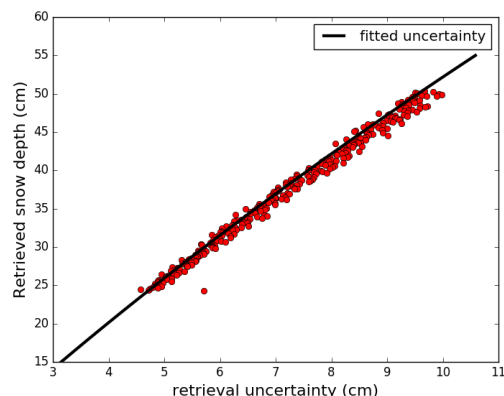


Figure 4.12: Same as Figure 4.11 but for MYI.

4.5 Conclusions

In this Chapter, the influences of the atmosphere, clouds, snow- and ice properties on the GR are estimated based on model simulations using the microwave emission model of layered snowpack (MEMLS), the passive and active radiative transfer model PAMTRA and the thermodynamic snow model SNOWPACK. All results are based on in-situ ice, snow and atmospheric measurements obtained during the first part of the N-ICE2015 campaign (winter conditions).

The (cloud free) atmosphere has only little influence on both GR, GR(19/7) and GR(37/19). For GR(19/7), the biggest source of uncertainty is the variability in the snow properties. Based on a case study for snow metamorphism introduced by warm air advection, an uncertainty in the GR(19/7) of about 20% due to different snow types was found. For GR(37/19) the influence of clouds (24%) and snow metamorphism (29%) are of similar range. The ice properties have only a strong influence on GR in the case of Arctic MYI. Here, the uncertainty is around 8% for GR(19/7) and 29% for GR(37/19). However, the results for the influence of the MYI properties on the GR are lower than what is found in satellite observations. This potentially is due to the simplified description of microwave scattering in sea ice implemented in MEMLS. The influence of the ice roughness on the GR is not investigated here.

It was evaluated how the uncertainties in GR derived here, influence the performance of potential GR based snow depth retrievals. In the ideal case, without any uncertainties in GR, the GR(19/7) based retrieval performs best. The NRMSD of a GR(19/7) based retrieval is around 2% and for GR(37/19) 10%. Including the uncertainty of the GR to the regression analysis using a Monte-Carlo simulation (only for FYI), all NRMSD increase. The NRMSD of GR(37/19) increases 19% and of GR(19/7) to 11%. These results show the importance

of adding additional information to passive microwave based snow depth retrievals during both the training and operational use. While an estimation of the influence of the atmosphere and clouds on the brightness temperatures observed by satellite is already applied in e.g., passive microwave sea ice concentration retrievals (e.g., Lu et al., 2018), adding information about the snowtype remains difficult since measurements are sparse and thermodynamic snow evolution modelling is challenging. In the ongoing MOSAiC campaign, an extensive dataset of year round snow and ice properties will be collected. This dataset might help to improve the understanding of snow processes relevant for microwave scattering and helps to reduce uncertainties in passive microwave based snow depth on Arctic sea ice retrievals.

Using the results of the Monte-Carlo uncertainty model, a new uncertainties estimation is derived for the empirical AMSR-E/2 snow depth retrieval developed in Chapter 3. For shallow snow, the newly derived uncertainties give more realistic values compared to the uncertainties derived in chapter 3, which were almost zero for snow depths around 10 cm. The variability of the brightness temperatures due to the influence of geophysical parameters found in this study is not limited to passive microwave snow depth retrievals. They can also, after a few adjustments, be used to evaluate the sensitivity of other related sea ice parameter retrievals that are using similar microwave frequencies. These are e.g., sea ice concentration retrievals like the NASA-Team (Markus and Cavalieri, 2000) or the ASI algorithm (Spreen et al., 2008).

Chapter 5

Evaluation and Inter-comparison of Existing Snow Depth on Arctic Sea Ice Retrievals

In this chapter, the newly derived snow depth on Arctic sea ice retrieval is evaluated in more detail and inter-compared with three other passive microwave snow depth retrievals. The chapter is organised as follows: In section 5.1, three different snow depth retrievals, which are used for the inter-comparison, are introduced. In section 5.2, the snow depth retrievals are evaluated with in-situ snow depth measurements from various campaigns. Then, the seasonal evolution of the different retrievals is analysed in section 5.3 and compared to SNOWPACK simulations in section 5.4. The chapter closes with a discussion (section 5.5) and a summary (section 5.6).

5.1 Satellite Retrievals

In addition to the snow depth retrieval derived in chapter 3 (PR retrieval hereafter), three other snow depth retrievals are evaluated and inter-compared. All retrievals are based on passive microwave satellite observations, but are using different empirical models or training datasets. Except for one retrieval, no datasets to download exists and thus the snow depth was manually calculated using the empirical retrieval models described in the respective publications.

Marcus and Cavalieri Retrieval

Markus and Cavalieri (1998) were the first to develop a snow depth retrieval using passive microwave satellite observations (MC retrieval hereafter). The authors compared ship-borne snow depth observations from the ASPeCT protocol (Markus and Cavalieri, 1998) to passive microwave observations the DMSP SSM/I sensor (Defense Meteorological Satellite Program, Special Sensor Microwave/Imager; Meier et al., 2019). Using a linear regression model, they found that the gradient ratio $GR(37/19)$ (see equation 3.1) of vertical polarised brightness temperatures has the highest correlation to the ASPeCT snow depth observations. The regression coefficients were adapted to the AMSR-E sensor by Comiso et al. (2003), which was necessary due to differences in the incident angles (53° vs. 55°) and frequencies (e.g., 19.35 vs. 18.7 GHz and 37 GHz vs 36.5 GHz) of the SSM/I and AMSR-E sensors. The snow depth is retrieved based on:

$$Sd(cm) = 2.9 - 782 * GR(37/19) \quad (5.1)$$

In the Arctic, the product is only available for FYI. The uncertainty of this product is set to 5 cm and studies have shown that the retrieval performs well over smooth FYI (Cavalieri et al., 2014) but tends to underestimate snow depth over rough ice (Stroeve et al., 2006; Worby et al., 2008). The retrieval was applied on an operational basis only until 2011 (Comiso et al., 2003). The spatial resolution of the retrieval is 12.5 km x 12.5 km.

Neural-Network Retrieval

A neural network-based snow depth retrieval (NN retrieval hereafter) was developed by Braakmann-Folgmann and Donlon (2019). The retrieval uses AMSR2 brightness temperature observations which were fitted to OIB snow depth measurements using a neural network model. The model inputs are $GR(19/7)$, $GR(37/19)$ and $PR(37)$ (see equation 3.2). The model is available under <https://zenodo.org/badge/latestdoi/170323330> (accessed: 10 November 2019). The authors did not distinguish between FYI and MYI and thus, the retrieval is applied independent of the ice type. Since the model is only trained for AMSR2 observations, the AMSR-E observations are inter-calibrated to AMSR2 based on Du et al. (2014). For this snow depth retrieval, no uncertainties are provided. The spatial resolution of the retrieval is 25 km x 25 km.

Multilinear Retrieval

A snow depth retrieval based on a multilinear regression model (ML retrieval hereafter) was developed by Kilic et al. (2019). The retrieval is trained with OIB and buoy snow depth observations. Equation 5.2 shows the retrieval equation as published in Kilic et al. (2019) but converted to cm. The retrieval uses vertically polarised brightness temperature observations at 6.9 GHz (Tb_7), 18.7 GHz (Tb_{19}) and 36.5 GHz (Tb_{37}).

$$Sd(cm) = 177.01 + 1.75 * Tb_7 - 2.80 * Tb_{19} + 0.41 * Tb_{37} \quad (5.2)$$

Similarly to the NN product, the retrieval is applied independently of the ice type. No uncertainty estimation for this retrieval is given. The spatial resolution of the retrieval is 25 km x 25 km

5.2 Evaluation with In-situ Data

In this section, the four snow depth retrievals are evaluated with in-situ measurements. Measurements of snow on Arctic sea ice that cover a large enough fraction of a satellite pixel (here used: 25 km x 25 km) are rare. In the following evaluation, data from eight different campaigns are used which cover a fraction of at least 10% within a satellite pixel. The different campaigns are briefly introduced below.

SUMup Dataset

The SUMup (Surface Mass Balance and Snow on Sea Ice Working Group) dataset is a collection of Arctic sea ice and snow related datasets from different (partially unpublished) measurement campaigns. The data are quality controlled and provided in a fixed format (see <https://arcticdata.io/catalog/view/doi:10.18739/A2WS8HK6X>, accessed 16 January 2020). From the dataset, unpublished field observations in the central Arctic from March and April 2017 are used, which were taken during the INTPART Arctic Field Summer School (Turner et al., 2017). Overall, measurements over two FYI and two MYI pixels can be used from this campaign (blue asterisk in the Central Arctic and in the Beaufort Sea in Figure 5.1). Measurements covering the same satellite pixel were collected over several days. Since the satellite retrieved snow depth did not change over these days, the measurements were combined to improve the fractional coverage of the satellite pixel.

AMSRice03 Campaign

The AMSRice03 was a joint aircraft and in-situ measurement campaign which took place in March 2003 (Cavalieri et al., 2003) with the aim to evaluate the AMSR-E sea ice related products including snow depth on sea ice. Snow depth measurements were collected near Barrows (purple asterisk in Figure 5.1) and cover one satellite pixel over FYI. The data was downloaded from the National Snow and Ice Data Center (Sturm and Stroeve, 2009).

AMSRice06 Campaign

Similar to AMSRice03, the AMSRice06 campaign took place in March 2006 with the perspective to evaluate the AMSR-E sea ice related products. In-situ and aircraft snow- and ice measurements were taken over a one week period in the Chukchi and Beaufort Seas (see https://polynya.gsfc.nasa.gov/seaice_arctic2006.html, accessed 16 January 2020). From this campaign, only the mean and standard deviation of the measurements are published. The measurements cover one satellite pixel (purple asterisk in Figure 5.1, same location as for the AMSRice03 campaign).

CryoVex11 Campaign

The CryoVex11 campaign took place in mid April 2011 (see https://earth.esa.int/c/document_library/get_file?folderId=87248&name=DLFE-1870.pdf; accessed 02 March 2020). The aim of this campaign was to study the Arctic snow and ice characteristics and to analyse their effects on Ku-band radar observations. The basecamp of the campaign was situated in Alert, Greenland and snow depth measurements were taken with a ruler stick at two locations on MYI north of the Canadian Archipelago (red asterisk in Figure 5.1). The dataset is part of a large in-situ data collection published by Holt (2019).

GreenArc Campaign

The GreenArc campaign was carried out on 25 April 2009 on deformed FYI and MYI north of Greenland (dark green asterisk in Figure 5.1; Farrell et al., 2012). Snow depth measurements were taken along 2 km long transects. The measurements were used to evaluate OIB snow depth and ice thickness measurements. Similar to the CryoVex11 campaign, the dataset was downloaded from the data collection published by Holt (2019).

SEDNA Campaign

The SEDNA campaign took place in March and April 2007 in the Beaufort ice camp north of Alaska (light green asterisk in Figure 5.1; http://psc.apl.washington.edu/sea_ice_cdr/documentation/airborne_em/SEDNAfieldReport.pdf, accessed 24 February 2020). The aim of this campaign was to assess the dynamic nature of Arctic sea ice. Extensive snow depth measurements were taken over mainly FYI at 05 April 2007. Similar to the CryoVex11 campaign, the dataset was downloaded from the data collection published by Holt (2019).

N-ICE2015 Campaign

The N-ICE2015 campaign took place from January to June 2015 in the Atlantic sector of the Arctic Ocean. The campaign is described in detail in chapter 4.1.1. From the campaign, Magnaprobe snow depth measurements are available (Rösel et al., 2016), covering one satellite pixel over FYI and one satellite pixel over SYI. The measurements used here were collected over several days in March (FYI) and April (SYI). Since the satellite retrieved snow depth did not change during these days, the measurements are summarised into one pixel for FYI and one for SYI in order to improve their representativeness (pink asterisk in Figure 5.1). Measurements were also collected in January and February but due to the high amount of SYI in this area, the PR retrieval is not available (snow depth over MYI is only retrieved in March and April) and thus the measurements are not used in the evaluation.

Results

Figure 5.2 shows the histograms of snow depth measurements obtained from the SUMup dataset for two different satellite pixels over FYI in the Beaufort Sea (left) and in the Central Arctic Ocean (right). In addition, the mean (red dashed line) and median (blue dashed line) of the measurements and the snow depths from the different satellite retrievals are shown. The errorbar for the PR retrieval is the uncertainty derived in chapter 4.

For the measurements in the Beaufort Sea (Figure 5.2, left) the NSIDC retrieval is closest to the mean of the measurements (17 cm) with a difference of around -2.3 cm. The PR retrieval performs second best with a difference of 3.4 cm, which is within its uncertainty estimation. The difference between the NN retrieval and the mean of the measurements is around 5 cm. The ML retrieval underestimates the measured snow depth by around 10 cm. For the FYI pixel in the Central Arctic (Figure 5.2, right), all retrievals perform worse. All retrievals are closer to the median than mean snow depth. The PR and the NN retrieval both underestimate the mean snow depth (27 cm) by around 8 cm and the ML retrieval is even 12 cm too low.

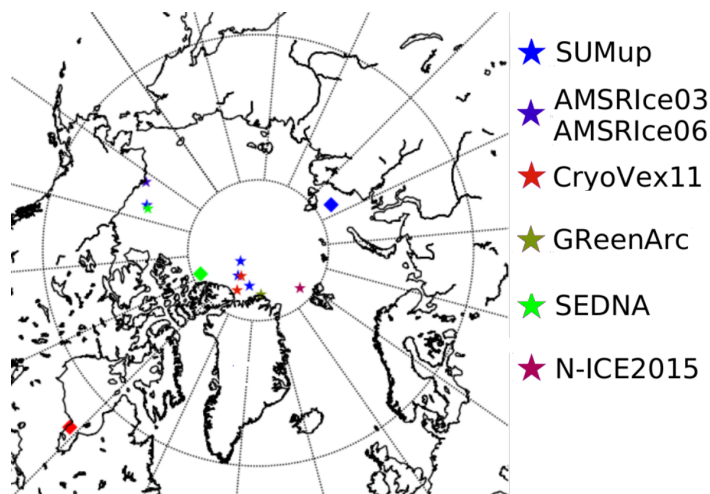


Figure 5.1: Location of the campaign data (asterisk) used for the evaluation of the snow depth retrieval. In addition, the locations of the three SNOWPACK simulations are shown (diamonds).

The NSIDC retrieval is not available due to a too high MYI concentration (= 42%).

Over MYI (Figure 5.3, left) the PR and NN retrieval are within 2 cm of the measurements and the ML retrieval is 3.4 cm lower than the mean of the measurements (29 cm). For the pixel in the central Arctic (Figure 5.3, right), the ML retrieval performs best with an underestimation of around 5 cm. The PR and NN retrieval are about 10 cm lower than the mean of the measured snow depth (39 cm).

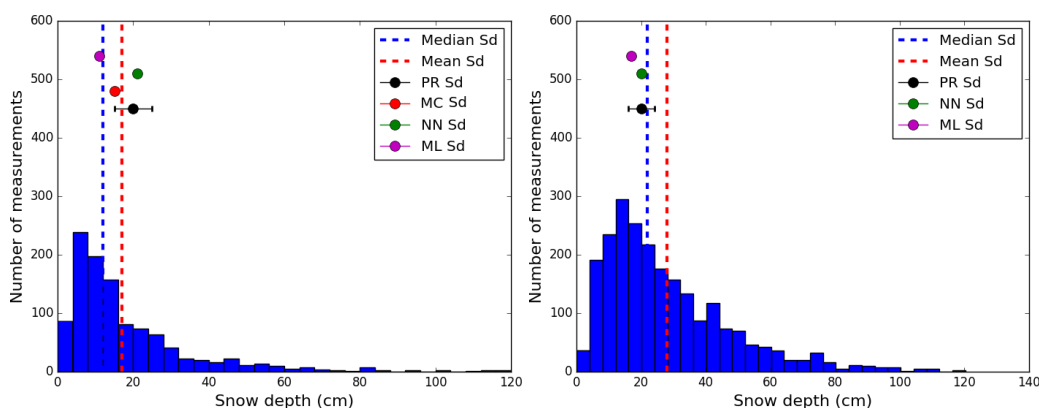


Figure 5.2: Histogram of measured snow depth over FYI from the SUMup dataset in the Beaufort Sea (left) and Central Arctic (right). In addition, the mean and median of the measured snow depth and the snow depths retrieved from different satellite retrievals are shown.

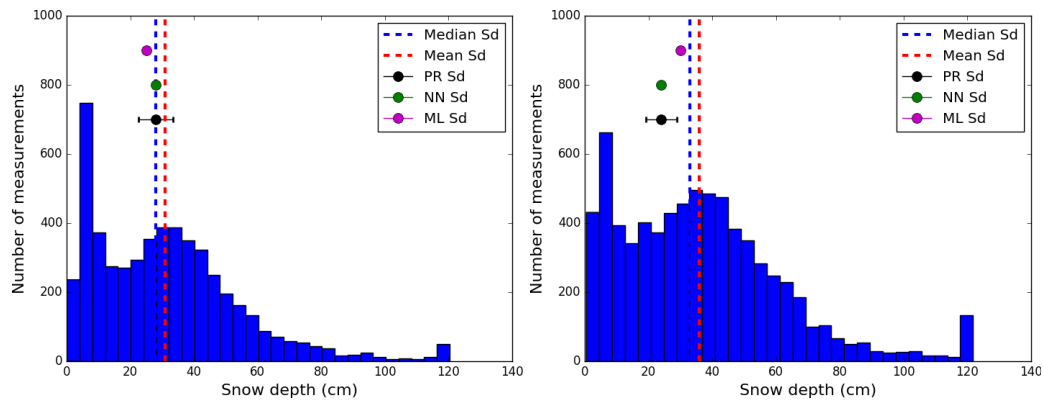


Figure 5.3: Same as Figure 5.2 but for two satellite pixels over MYI.

Figure 5.4 (left) shows the measurements obtained during the AMSRice03 campaign over FYI. The distribution of the measurements shows two peaks around 6 cm and 30 cm. In this campaign, measurements were taken at three different sites with slightly different ice conditions (shallow ice, smooth ice, rough ice). Shallow snow was present on the shallow and smooth ice while deep snow (peak at 30 cm) was found on rough ice. This shows how variable the snow depth conditions can be within one satellite pixel and that a representative sampling is needed to avoid biases in the data. Here, all retrievals overestimate the mean snow depth (15 cm). The PR and ML retrievals overestimate the mean by around 4 cm and the NN and NSIDC retrievals by around 5 cm and 6 cm, respectively.

Figure 5.4 (right) shows the distribution of the snow depth derived from the measurements of the AMSRice06 campaign. For this campaign, only the mean and standard deviations of the snow depth measurements are provided and therefore, the distribution had to be estimated. Here, due to the lack of better options, a normal distribution was assumed even though this might not reflect the true snow depth distribution in this region. All retrievals overestimate the measured snow depth. The PR and ML retrieval perform best with a difference to the mean measured snow depth of around 5 cm. The NSIDC and NN retrieval overestimate the mean snow depth by 8 cm.

Figure 5.5 shows the measurements obtained during the CryoVex11 campaign for two different pixels over MYI (left and right). Overall, only around 100 measurements within the pixels are available covering a transect of roughly 500 m length. Therefore, the mean of the measurements might not represent the mean snow depth of the whole satellite pixel. For both pixels, the ML retrieval is closest to the measurements with a difference to the mean of 6 cm in pixel one (Figure 5.5, left) and -2 cm in pixel two (Figure 5.5, right). Both, the PR and NN retrievals underestimate the measured snow depth in both pixels. In case of the PR retrieval, the underestimation is around 10 cm in both pixels.

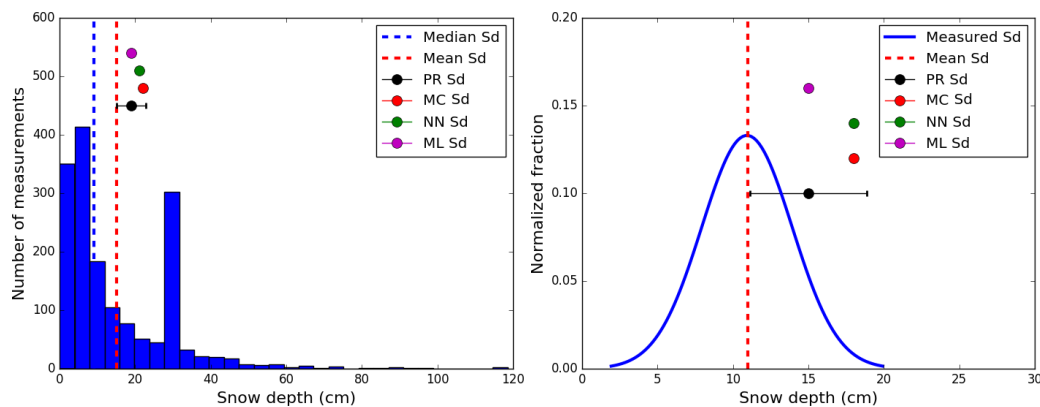


Figure 5.4: Left: same as Figure 5.2 but for the AMSRice03 campaign. Right: Normal distribution of the snow depth measured during the AMSRice03 campaign. In addition, the snow depths from different satellite retrievals are shown.

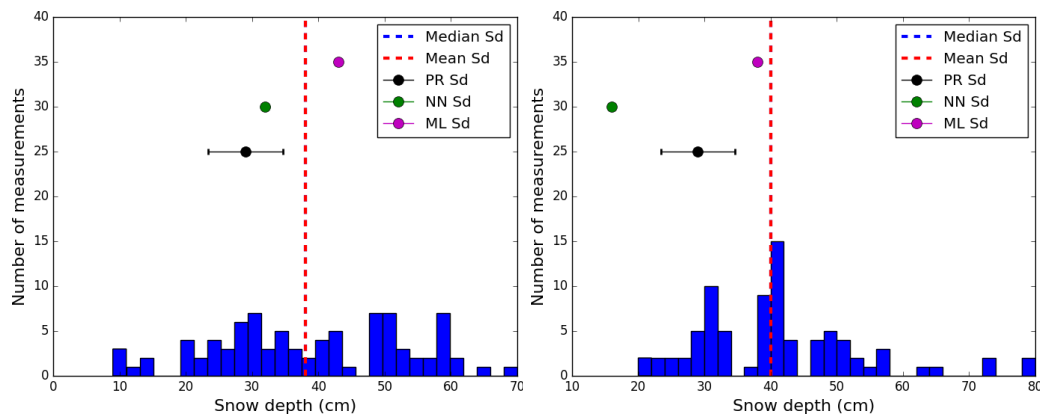


Figure 5.5: Same as Figure 5.2 but for the snow depth measurements from the CryoVex11 campaign over two MYI pixels.

Figure 5.6 shows the measurements obtained during the GreenArc campaign over MYI (left) and SEDNA campaign over FYI (right). For both campaigns, the PR retrieval matches the mean of the measurements within 1 cm while the NN and ML retrievals overestimate the snow depth measured during the GreenArc campaign and underestimate the snow depth measured during the SEDNA campaign.

Figure 5.7 shows the histogram of the snow depth obtained during the N-ICE2015 campaign over FYI (left) and SYI (right). All satellite retrievals underestimate the mean of the snow depth measurements over both FYI (49 cm) and SYI (43 cm) by at least 20 cm. The PR retrieval performs best with an underestimation of the N-ICE2015 snow depth by about 25 cm over FYI and 20 cm over SYI.

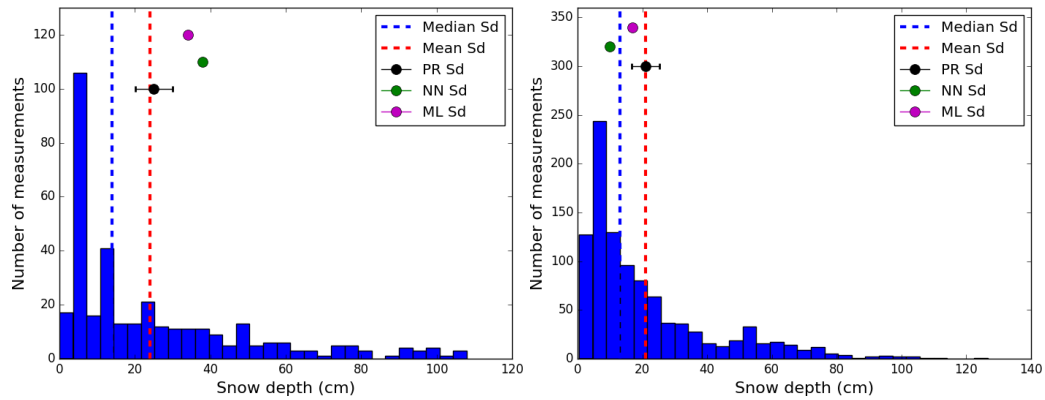


Figure 5.6: Same as Figure 5.2 but for the snow depth measurements from the GreenArc campaign over MYI (left) and SEDNA campaign over FYI (right).

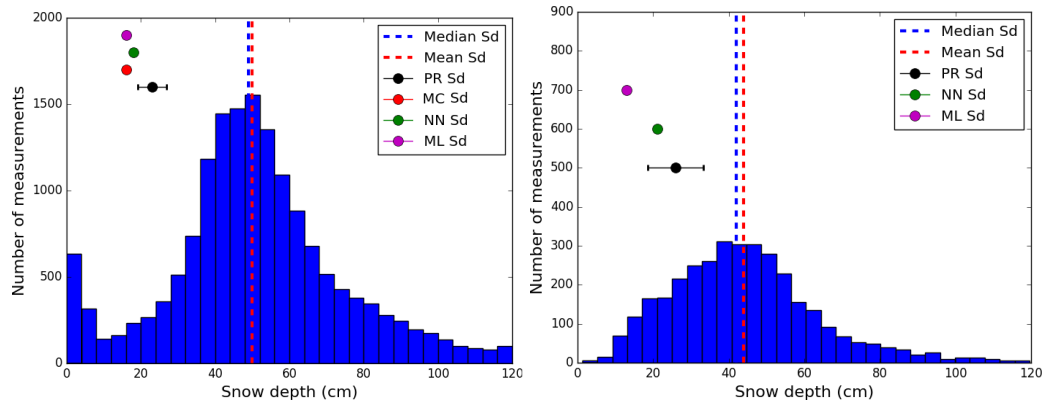


Figure 5.7: Same as Figure 5.2 but for the snow depth measurements from the N-ICE2015 campaign over FYI (left) and SYI (right).

Different to the data analysed before, the snow depth distributions measured during the N-ICE2015 campaign have only a small peak at low snow depths over FYI (Figure 5.7, left) and no peak at low snow depths over SYI (Figure 5.7, right). There are two main differences between the measurements taken during the N-ICE2015 campaign and the other campaigns: (i) With respect to the snow depth retrievals analysed here, it is interesting to note that the ground truth data used for the training of the PR, NN and ML retrievals (OIB snow depth observations) does not cover the region where the N-ICE2015 campaign took place. The data from the campaigns analysed before are in regions which are also covered by OIB campaigns.

(ii) A very deep snowpack was reported during the N-ICE2015 campaign. In all other campaigns, the mean snow depth is around 20 cm lower than the mean snow depth found during the N-ICE2015 campaign. Caused by the high snow load, large-scale flooding was observed during the campaign (Provost et al., 2017), which lead to a layer of slushy, salty

snow at the bottom of the spring snowpack.

Due to the capillary force, salt gets soaked into the snowpack. In the microwave regime, salty snow is almost opaque and therefore strongly influences passive microwave satellite retrievals, i.e., it leads to an underestimation of the snow depth. Unfortunately, no salinity in snow measurements were obtained during the N-ICE2015 campaign. Figure 5.8 shows the result of a MEMLS simulation for an average snowpack ranging from 10 cm to 70 cm and three different salinity profiles in the lowest 15 cm of the snow based on the findings from Nandan et al. (2017). The salinity profiles used here are based on Figure 1 in Nandan et al. (2017). The results show that even for the mean salinity profile, the lowest 13 cm of the snowpack are not visible in GR(19/7). For example, at 50 cm, the GR of the snowpack assuming a mean salinity profile is as low as the GR of the snowpack assuming no salinity at 37 cm. This means, in the case of the mean salinity profile, the snow depth is underestimated by 13 cm. Therefore, flooding may (partly) explain the large differences between the measured snow depth and the retrieved snow depth. However, this could not be verified since no salinity measurements were taken during the N-ICE2015 campaign. Another reason for the large underestimation could be that the empirical retrievals used here were not well trained for deep snow over FYI. For example, in the training dataset which was used to develop the PR retrieval, less than 5% of all datapoints over FYI contain snow depths larger than 35 cm.

Table 5.1 summarises the results of the evaluation study. Here the mean difference to the measurements (= bias) and the RMSE (cm) are shown. In absence of a better solution, the data from all campaigns are weighted equally, although it could be argued that some of them might not be as representative as others due to a different spatial sampling within the satellite pixel. On Average, all retrievals underestimate the measurements. Except for the ML retrieval, the underestimation is larger for MYI than for FYI. Since overall only 12 datapoints are available for the analysis, the N-ICE2015 measurements have a large influence on the results. Excluding the N-ICE2015 measurements (values in brackets), the performance of all retrievals improves.

Over FYI, the PR retrieval has the lowest bias -5.9 cm to the measured data and the bias is almost zero when excluding the N-ICE2015 observations. Over MYI, the ML retrieval has the lowest bias in both cases, including the N-ICE2015 observations (bias of -3.4 cm) and excluding them (bias of 2.0 cm). Overall the PR retrieval has with 14.5 cm (4.9 cm) the lowest RMSE over FYI while over MYI, the ML retrieval performs best (RMSE = 13.3 cm).

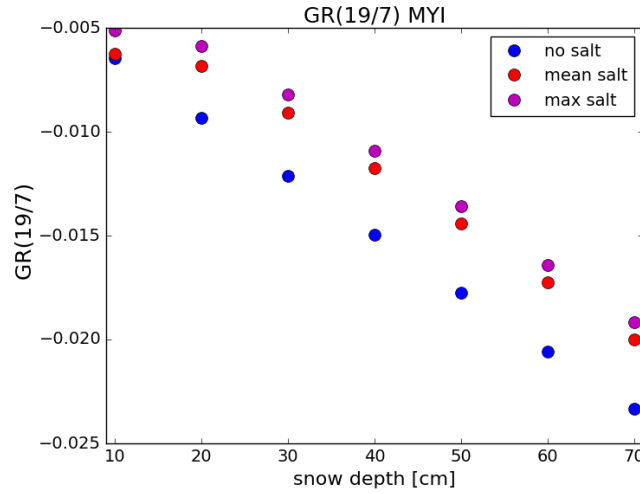


Figure 5.8: Simulated GR(19/7) for a snowpack with different salinity profiles in the lowest 15 cm of the snowpack.

The results found here can be used to evaluate the uncertainty of the PR retrieval estimated in chapter 4. The average uncertainty of the PR retrieval is around 5 cm for FYI (see Figure 4.11; average retrieved snow depth for the evaluated FYI pixels is 19.9 cm) and 6.5 cm for MYI (see Figure 4.12; average retrieved snow depth for the evaluated MYI pixels is 32 cm). This indicates that the uncertainty estimation over FYI is large enough (except for the N-ICE2015 observations) while over MYI, the estimated uncertainty might be too low.

Table 5.1: Evaluation of the different snow depth retrievals against in-situ measurements. Shown are the mean difference and RMSE for all data, FYI and MYI. The values in brackets show the results excluding the N-ICE2015 observations.

	Difference (cm)			RMSE (cm)		
	All	FYI	MYI	All	FYI	MYI
PR	-7.4 (-3.5)	-5.9 (-0.3)	-8.9 (-6.7)	12.9 (6.7)	14.5 (4.9)	11.1 (8.1)
MC	-	-7.1 (-0.3)	-	-	16.9 (8.3)	-
NN	-9.4 (-4.8)	-9.0 (-3.9)	-9.9 (-5.8)	16.5 (10.8)	15.6 (7.4)	17.0 (12.7)
ML	-7.5 (-1.9)	-11.5 (-5.7)	-3.4 (2.0)	15.9 (6.8)	17.8 (7.2)	13.3 (5.1)

5.3 Seasonal Cycle

Almost no large scale snow depth measurements exist from early and mid-winter. To evaluate the seasonal evolution of the new retrieval, an inter-comparison study between the four snow depth retrievals described above is carried out.

In addition to the snow depth retrievals described above, a different version of the PR retrieval is added (PR_mix). This version uses the combined GR(19/7) and GR(37/19) retrieval as suggested in chapter 4. The PR_mix retrieval is only applied over FYI. A 5-day running mean is applied to the retrieved snow depth to reduce day-to-day fluctuations.

Since the training data for most of the retrievals is limited to the Central Arctic and Beaufort Sea, it is important to evaluate their performance in different Arctic regions which may have very different snow and ice conditions. For the following study, the Arctic is split in six regions as shown in Figure 5.9. The regions are chosen such that they cover different Arctic meteorological and snow- and ice conditions. The division is based on the Arctic regions which Castro-Morales et al. (2017b) used in their study but slightly simplified and adapted to the main ice types (FYI and MYI) in the Arctic.

Region 1 (red) covers the Kara and Barents Seas where only FYI exist. Region 2 (yellow) covers the Laptev Sea and the East Siberian Sea. Also in this area, predominantly FYI exists but MYI may drift into the region through the Beaufort Gyre. In region 3 (green), which mainly covers the Beaufort Sea, high sea-ice drift is common and a mixture of FYI and MYI is expected. Region 4 (light blue) covers the Atlantic sector of the Arctic, a region where heavy snowfall occurs and flooding is more likely as observed during the N-ICE2015 campaign (Provost et al., 2017). Region 5 (pink) covers the Labrador Sea and the Baffin Bay and finally, region 6 (blue) covers the MYI region in the Central Arctic. The snow depth is averaged over the whole region of interest. Here the winter seasons 2005/2006 and 2018/2019 are discussed exemplary.

Barents and Kara Seas

Figure 5.10 shows the seasonal evolution of the snow depth retrieved in the winter season 2005/2006 (left) and 2018/2019 (right) in the Barents and Kara Seas (red area in Figure 5.9). In both years, the different snow depth retrievals show a similar pattern. At the start of the season, the MC and ML retrieval have the lowest snow depth (3 cm and 7 cm; season 18/19). Both the PR and the PR_mix retrieval start around 9 cm while the NN retrieval has a snow depth of around 20 cm, which is very high for beginning of November in the Kara and Barents Seas where freezing just started.

During the season both the PR and the MC algorithm show an increase in retrieved snow

depth. The increase is slightly stronger in the PR_mix retrieval than in the PR retrieval. The MC retrieval shows a even stronger increase in snow depth in both seasons, especially during mid winter.

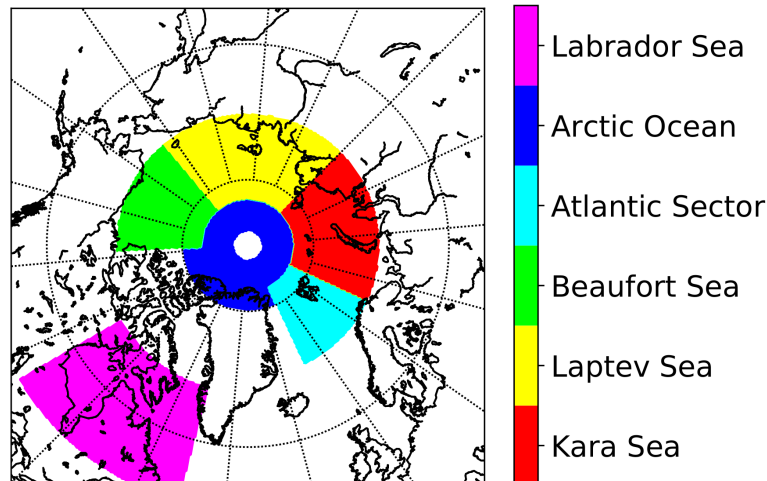


Figure 5.9: Six different regions of the sea ice covered Arctic.

At the start of the winter, the PR and MC retrievals show a high variability in their retrieved snow depth, which might be due to sea ice drift or a high temperature variability (this will be discussed in more detail in section 5.4). During mid-winter and spring, the day-to-day variability of the PR and MC retrievals decreases. In contrast, the NN retrievals shows a very high day-to-day variability throughout the whole season. Overall, the snow depth of the NN retrieval decreases until mid-winter and then stays on a similar level until the end of the season. The ML retrieval shows no increase in snow depth for both seasons. At the end of March 2019, a strong increase in snow depth is found in all retrievals. This can be related to a strong snowfall event which is visible in the ERA5 reanalysis snowfall product in the Kara Sea. The MC retrieval shows the strongest response with an increase in snow depth of around 5 cm. The PR, NN and ML retrievals show an increase in snow depth of around 3 cm. Even though the retrieved snow depths are different throughout the season, by April, the PR_mix, PR, MC and NN retrievals agree within 5 cm which is within the uncertainty of the MC and PR retrievals. However, the NN retrieval does not show any increase in snow depth throughout the season.

Laptev Sea

Figure 5.11 shows the seasonal evolution of the snow depth retrieved in the winter season 2005/2006 (left) and 2018/2019 (right) in the Laptev Sea (yellow area in Figure 5.9). Except for the ML retrieval, all other retrievals show a low day-to-day variability in their retrieved snow depth.

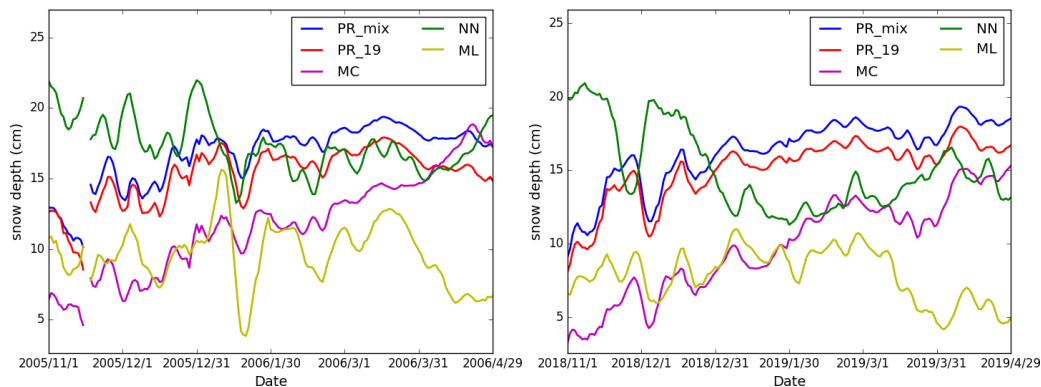


Figure 5.10: Seasonal evolution of the snow depth from five different satellite retrievals in the Barents and Kara Seas for the winter season 2005/2006 (left) and 2018/2019 (right). The covered area is shown in Figure 5.9 (red area). A 5-day running mean is applied to all data.

In 2018/2019, the PR, PR_mix and MC retrievals show an increase in snow depth until February and then the retrieved snow depth remains almost constant. In 2005/2006, the MC retrieval shows a strong increase in snow depth until January 2006, and then a strong drop in snow depth of around 6 cm. This is not visible in the other retrievals. Since the MC retrieval is not trained over MYI, this might be due to the influence of MYI drifting into the area. At the end of the season, all retrievals, except the ML retrieval, agree within 5 cm. Similar to the Barents and Kara seas, The PR_mix retrieval is slightly higher than the PR retrieval. This could be due to the inclusion of the 37 GHz observations in the PR_mix retrieval which has a higher sensitivity to snow depth than the 19 GHz observations used in the PR retrieval (see chapter 4). The difference is, however, below the uncertainty of the PR retrieval. Again, the NN and ML retrievals do not show the expected increase in snow depth throughout the winter.

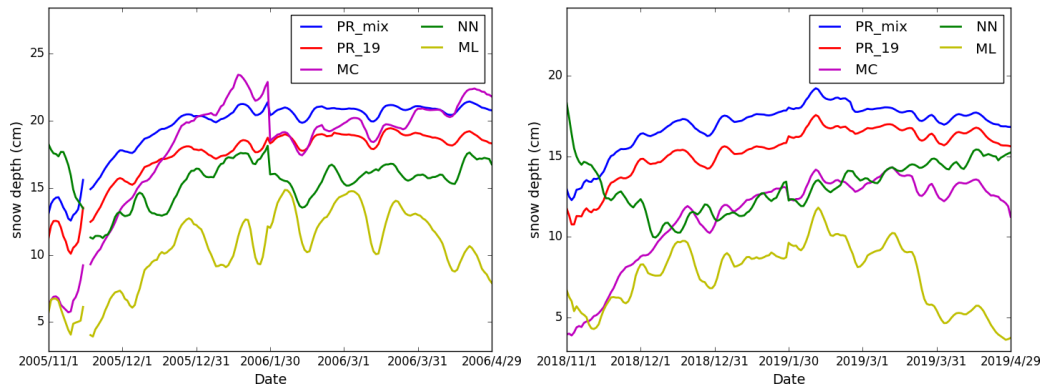


Figure 5.11: Same as Figure 5.10 but for the Laptev Sea (yellow area in Figure 5.9).

Beaufort Sea

Figure 5.12 shows the seasonal evolution of the retrieved snow depth for the winter season 2005/2006 (left) and 2018/2019 (right) in the Beaufort Sea (green area in Figure 5.9). The behaviour of the individual retrievals is similar to the other areas discussed until now. The NN retrieval starts with a high snow depth which is then decreasing until mid-winter. The MC retrieval starts with the lowest snow depth. Overall, the variability in the retrieved snow depth is very high for all retrievals which is likely due to sea-ice drift. Often MYI with a high snow load is drifting into the Beaufort Sea, which is e.g., visible in February 2006 where all snow depth retrievals show a strong, sudden increase in snow depth.

Atlantic Sector

Figure 5.13 shows the seasonal evolution of the snow depth retrieved in the winter season 2005/2006 (left) and 2018/2019 (right) in the Atlantic Sector of the Arctic (light blue area in Figure 5.9). Similar to the Beaufort Sea, sea-ice drift might lead to a high variability in the retrieved snow depths in all retrievals. Especially the MC retrieval shows a strong day-to-day variability during season 2018/2019.

Different to the other sectors, in the Atlantic sector of the Arctic, the ML retrieval agrees with the PR and NN retrievals in spring. The MC retrieval strongly differs in both seasons, especially in late winter and spring. Similar to the Beaufort Sea, MYI may drift into the Atlantic sector of the Arctic which could explain the differences in the MC product.

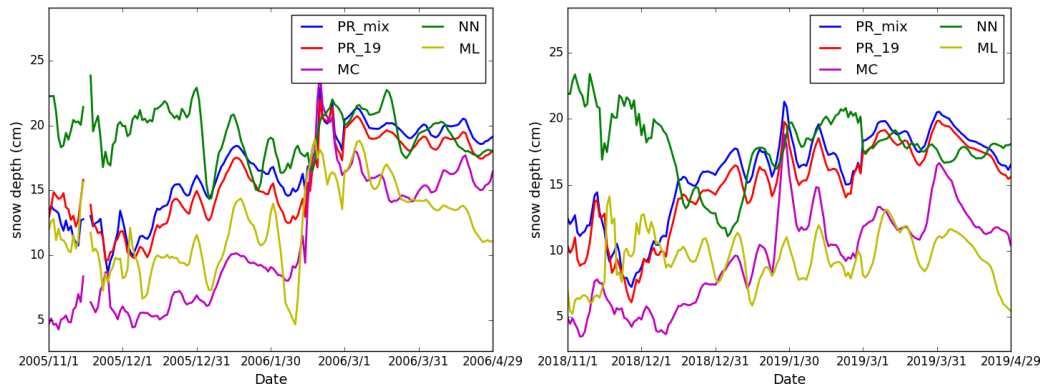


Figure 5.12: Same as Figure 5.10 but for the Beaufort Sea (green area in Figure 5.9).

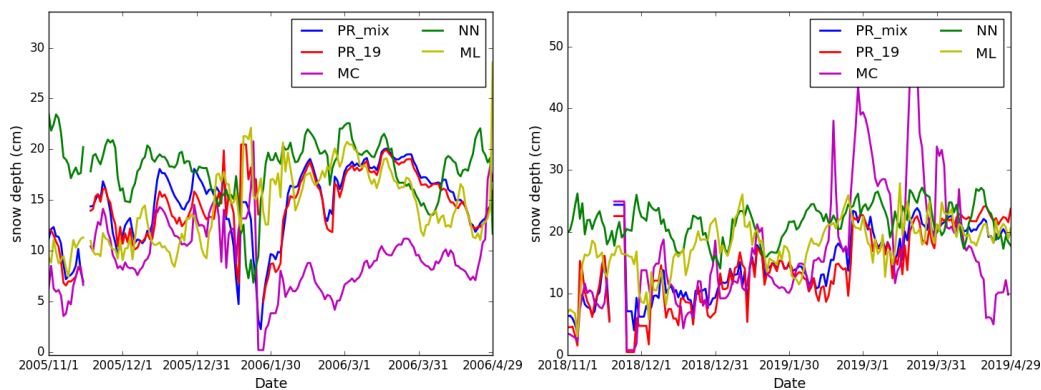


Figure 5.13: Same as Figure 5.10 but for the Atlantic Sector (light blue area in Figure 5.9).

Labrador Sea

Figure 5.14 shows the seasonal evolution of the snow depth retrieved in the winter season 2008/2009 (left) and 2018/2019 (right) in the Labrador Sea and Hudson Bay (pink area in Figure 5.9). Here, season 2008/2009 is shown instead of season 2005/2006 since freezing started late in the 2005. All retrievals show high variability in the retrieved snow depth at the beginning of the freezing season until mid-winter. During season 2008/2009, a sharp increase in snow depth is visible in the MC and PR retrievals while the NN and ML retrieval show no signal. The strong snowfall event in April 2019 is captured by all retrievals.

Central Arctic

Figure 5.15 shows the seasonal evolution of the snow depth retrieved in the winter season 2005/2006 (left) and 2018/2019 (right) in the Central Arctic (blue area in Figure 5.9). In this area, mainly MYI is present and therefore, only the NN and ML retrieval are applied

for the whole season. The PR retrieval is limited to March and April. Both, the NN and ML retrieval show no increase of snow depth during the whole season and the ML algorithm retrieves almost 30 cm deeper snow than the NN retrieval. In March and April, the PR and NN retrieval agree within 5 cm in season 2005/2006 and within 8 cm in season 2018/2019.

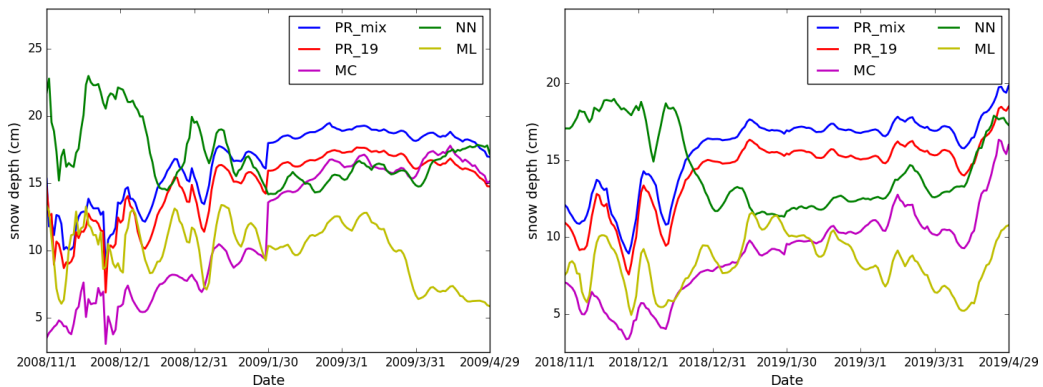


Figure 5.14: Same as Figure 5.10 but for the Labrador Sea (pink area in Figure 5.9).

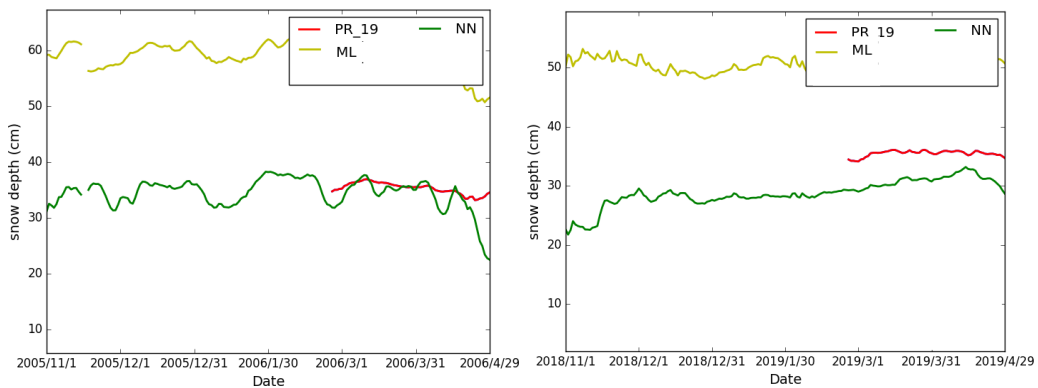


Figure 5.15: Same as Figure 5.10 but for the Arctic Ocean (blue area in Figure 5.9).

Summary

The results presented above revealed large differences between the single products, especially in early winter. This indicates the need of further evaluation, especially in early and mid-winter. In March and April, however, most of the retrievals are in good agreement. Also the MC retrieval, which was trained with Antarctic snow depth observations shows, in most sectors of the Arctic, similar snow depth in March and April. This confirms the results found in the evaluation section (section 5.2) that the retrievals perform well in March and April in most sectors of the Arctic. Snow depth is expected, with some variability, to increase

monotonically throughout the winter season. Thus questionable results are obtained from the ML retrieval which remains low during the whole season and shows almost no increase in snow depth. Also the NN algorithm retrieves unreasonably high snow depths at the beginning of the winter.

5.4 Sensitivity to Snow Evolution

The analysis carried out above revealed the need to further evaluate the seasonal cycle of the PR retrieval. Other than in-situ measurements, reanalysis-based snowfall products provide an option to derive daily and large scale information about snow depth on Arctic sea ice. It is, however, not possible to directly compare snowfall and snow depth since the transformation processes are hardly known and models using snowfall rely on empirical parametrisations (e.g., Petty et al., 2018).

Different reanalysis products have large differences in the amount of snowfall they produce due to different parametrisation schemes for snow and liquid water precipitation (Boisvert et al., 2018). However, good agreement is found in the temporal and spatial patterns of strong snowfall events (e.g., Boisvert et al., 2018). Therefore, it can be useful to compare the sensitivity of the snow depth retrieval to snowfall events and to analyse if the sensitivity changes in the course of the season. This is very important since the PR retrieval was only trained and evaluated with spring snow depths.

In this section, simulations with the SNOWPACK model (see chapter 4) are performed for the 2018/2019 winter season. SNOWPACK is a 1-d model and due to its advanced snow microphysics, simulations are cost-expensive and can not be carried out for the whole sea-ice covered Arctic. Therefore, first the ERA5 reanalysis snowfall product (Hersbach and Dee, 2016) is analysed to find areas in the Arctic where large snowfall events happened. These should be, in the best case, distributed over the whole winter season.

Figure 5.16 shows the integrated snow water equivalent (SWE) over the sea ice covered Arctic from ERA5 reanalysis data from November 2018 to April 2019. Integrated SWE values up to 300 mm are found around the coastal areas in the Arctic Ocean, whereas in the MYI region, integrated SWE values rarely exceed 100 mm. To reduce errors due to uncertainties in sea-ice drift products, regions with low sea-ice drift are selected. Furthermore it is important that the trajectory of the considered area reaches back until the beginning of the freezing season. Based on these criteria, SNOWPACK simulations are carried out in three different areas (100 km x 100 km averages are used) in the Barents Sea (blue diamond in Figure 5.1), the Labrador Sea (red diamond in Figure 5.1) and north of the Canadian Archipelago (green diamond in Figure 5.1).

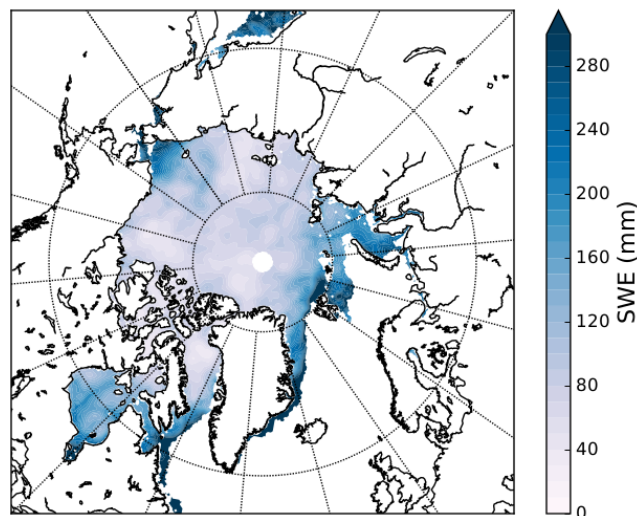


Figure 5.16: Integrated snowfall (SWE) from ERA5 reanalysis for the sea ice covered Arctic from 01 November 2018 to 30 April 2019.

Note that in Figure 5.1, the locations at the end of the season (30 April) are shown. For all three simulations, sea-ice drift backtracking trajectories are computed using the OSI-SAF sea-ice drift dataset (Lavergne et al., 2010) by starting on 30 April and then re-tracking the movement of the selected area back to 01 November. For the selected areas in the Labrador Sea and Barents Sea, the absolute shift in position was less than 5 pixels. For the area north of the Canadian Archipelago, the absolute shift in position was around 15 pixels. The main focus will be on evaluating the PR retrieval including a short comparison with the other retrievals.

Barents Sea

To initialise the model, parameters like the initial sea-ice thickness, the ocean heat flux and the initial snowpack have to be estimated. Selected initialisation values for the simulation in the Barents Sea are shown in Table 5.2. The whole initialisation file can be found in Appendix C (see Table C.1). As a first guess, the snow depth from the PR retrieval at 01 November 2018 was used (= 7 cm). The initialisation snowpack consists of two layers, a layer of fresh snow at the top (3 cm depth) and a depth hoar layer at the bottom (4 cm). For the sea ice, a typical FYI is assumed with a C-shaped salinity profile. The initial ice thickness (30 cm) was chosen based on the thin ice thickness product from <https://seaice.uni-bremen.de/thin-ice-thickness/> (Huntemann et al., 2014). The sea ice was initialised with a solid ice fraction of 95% and a void fraction of 5%. All the assumptions made for the initialisation lead to large uncertainties in the temporal evolution of the sea ice thickness. However, in this study, the main focus is

on evaluating the sensitivity of the PR retrieval to snowfall under different meteorological and snowpack conditions.

Figure 5.17 shows the timeseries of the snow grain type and snow depth from the SNOWPACK simulation. The black line is the snow depth retrieved from the PR retrieval. To improve the readability, the Figure is cut and does not show the bottom part of the sea ice. Overall, the sea ice grows from 30 cm to 130 cm during the season. Note that in figure 5.17 (and in all subsequent figures) the ice freeboard rises during the season. The height scale on the y-axis refers to the sum of the ice freeboard and snow depth. Thus the freeboard has to be subtracted from the height scale in order to obtain the snow depth.

The simulated snow depth is higher than the retrieved snow depth. This is an expected result since the SNOWPACK model does not consider the loss of snow due to wind redistribution, e.g., to ridges, or drift into open water. Similar results were found in simulations on Antarctic sea ice (Wever et al., 2019) where the authors compared the simulated snow depth to buoy measurements. The snow grain type remains predominantly fragmented snow (note that for most of the time, SNOWPACK gives wind slab as secondary snow type) with a layer of depth hoar in the middle of the snowpack. Below the layer of depth hoar, a melt-refreeze layer forms during the snowfall event around 20 November. Only at the end of March, a snowfall event under warm conditions (see Figure 5.18, left) leads to a layer of rounded grains at the top of the snowpack. At the bottom of the snowpack a melt-refreeze layer forms around 10 December just after a larger snowfall event. This indicates that SNOWPACK simulates a flooding event.

The snowfall event in March led to an increase of the retrieved snow depth by 6 cm. Rounded grains are strong scatterer (e.g., Mätzler, 2002) and thus decrease the gradient ratio more than other snow types. In contrast to the simulated snow depth, the retrieved snow depth is not instantaneously increasing after a snowfall event but increases slowly over a few days. This behaviour is expected since new fallen snow is a weak scatterer in the frequency range used for the PR retrieval and thus the new snow first has to be compacted and transformed into wind slab or fragmented snow until it is visible in the satellite observations.

Table 5.2: Initialisation data for the SNOWPACK simulation at a grid point in the Barents Sea. Shown are the layer thickness (L), temperature (T), ice volume fraction (I_{frac}), void volume fraction (V_{frac}) and salinity (S) for the six ice layers (I1 - I6, bottom to top) and the two snow layers (S1-S2, bottom to top). In addition, salinity and ocean heat flux (F) of the underlying ocean (layer B) is shown.

	L (m)	T (K)	I_{frac}	V_{frac}	S (ppt)	F (W/m ²)
B					34	3
I1	0.2	269.0	0.95	0.05	6	
I2	0.02	267.0	0.95	0.05	5.4	
I3	0.02	266.85	0.95	0.05	5.0	
I4	0.02	266.0	0.95	0.05	4.0	
I5	0.02	265.0	0.95	0.05	5.0	
I6	0.02	264.0	0.95	0.05	6.0	
S1	0.04	263.0	0.29	0.71	0.0	
S2	0.03	263.0	0.34	0.64	0.0	

Figure 5.18 shows the temporal evolution of the temperature (left) and grain size profiles (right). The snow temperature in the Barents Sea is mostly well below 0°C with a strong negative temperature gradient (bottom to top). Only during some snowfall events, the temperature at the top of the snowpack increases up to -5°C and the temperature gradient diminishes (e.g., at 20 November or 28 March). The grain size in the snow slightly increases during the season (Figure 5.17, right) and a layer of larger grains in the middle of the snowpack forms around November 20.

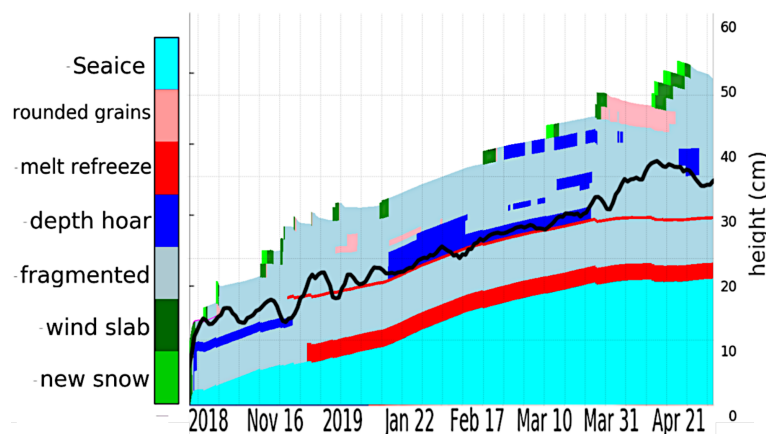


Figure 5.17: Grain type and snow depth of the simulated snowpack in the Barents Sea from November 2018 to April 2019. The back line shows the retrieved snow depth from the PR retrieval.

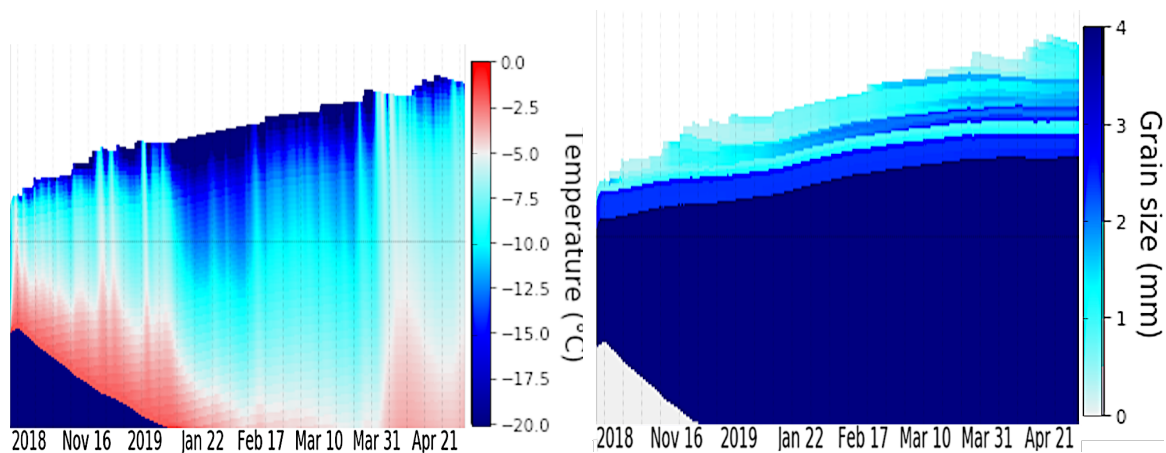


Figure 5.18: Temperature (left) and grain size (right) of the simulated snow-seaice system in the Barents Sea from November 2018 to April 2019.

Figures 5.19, 5.20 and 5.21 show the same as Figure 5.17 but with the snow depth retrieved from the MC, NN and ML algorithms. The snow depth from the MC retrieval (Figure 5.19) shows a similar seasonal evolution as the PR retrieval (Figure 5.17) at the beginning of the winter season. Around end of January, the retrieved snow depth drops to 5 cm and then starts increasing from mid February until beginning of April. The response to the snowfall event which led to a layer of rounded grains in March (March snowfall event hereafter) is stronger in the MC product than in the PR product. This is expected since the MC retrieval uses observations from the frequency channel at 36.5 GHz, which is more sensitive to the snow type compared to the frequencies used in the PR retrieval (6.9 GHz and 18.7 GHz, see also Figure 2.6).

The NN product (Figure 5.20) retrieves high snow depth (≈ 20 cm) at the beginning of the freezing season and then the snow depth decreases until 10 March 2019. For the March snowfall event, an almost instantaneously increase in retrieved snow depth of around 18 cm is visible.

The snow depth retrieved from the ML product (Figure 5.21) shows a high variability until beginning of 2019. Overall the retrieved snow depth decreases from around 12 cm at 15 November to 0 cm at 10 March. Afterwards the snow depth slightly increases again. Different to the other retrievals, the March snowfall has almost no influence on the retrieved snow depth.

These results show that the NN and ML retrievals have problems reproducing a reasonable seasonal cycle, even though the evaluation with in-situ measurements showed that both retrievals perform reasonably well in spring.

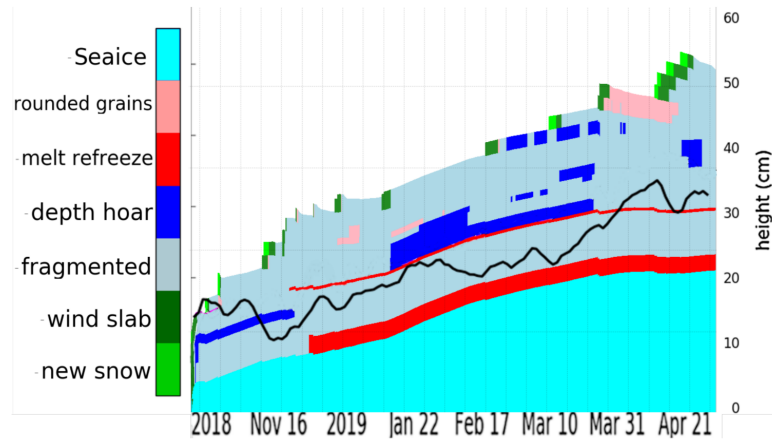


Figure 5.19: Same as Figure 5.17 but with the snow depth retrieved from the MC retrieval.

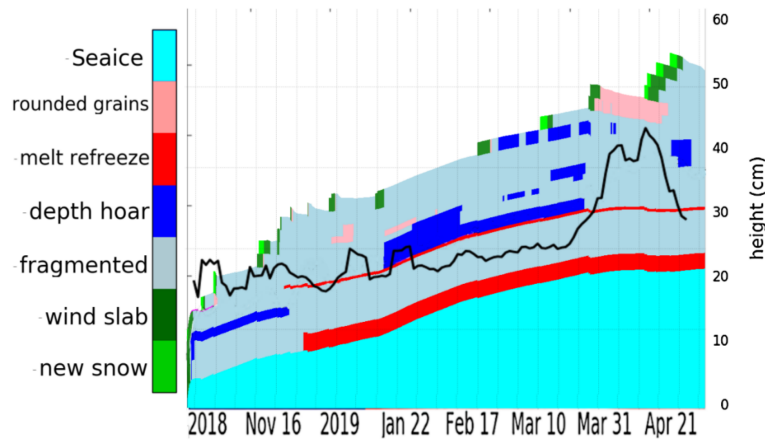


Figure 5.20: Same as Figure 5.17 but with the snow depth retrieved from the NN retrieval.

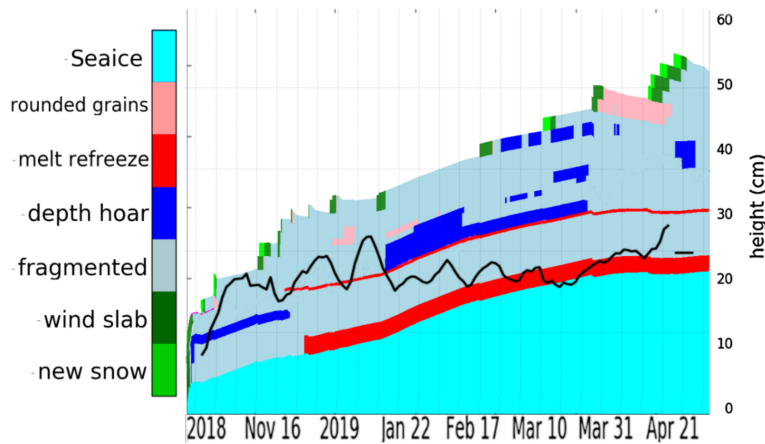


Figure 5.21: Same as Figure 5.17 but with the snow depth retrieved from the ML retrieval.

Labrador Sea

Table 5.3 selected initialisation values for the SNOWPACK simulation in the Labrador Sea (red diamond in Figure 5.1). Similar to the initialisation profile for the Barents Sea, the initial snow- and ice parameters are chosen from the PR snow depth retrieval (=15 cm) and Huntemann et al. (2014) sea ice thickness retrieval (=25 cm). The whole profile is given in Appendix C (see Table C.2). For the Labrador Sea, the simulation starts at 01 December since before December, no snow depth was retrieved around the area of interest due to a too low sea ice concentration.

Table 5.3: Same as Table 5.2 but for the SNOWPACK simulation in the Labrador Sea.

	L (m)	T (K)	I_{frac}	V_{frac}	S (ppt)	F (W/m ²)
B					34	3
I1	0.1	269.0	0.95	0.05	6	
I2	0.02	267.0	0.95	0.05	5.4	
I3	0.02	266.85	0.95	0.05	5.0	
I4	0.04	266.0	0.95	0.05	4.0	
I5	0.03	265.0	0.95	0.05	5.0	
I6	0.04	264.0	0.95	0.05	6.0	
S1	0.10	263.0	0.29	0.71	0.0	
S2	0.05	261.0	0.34	0.64	0.0	

Figure 5.22 shows the same as Figure 5.17 but for the Labrador Sea (red diamond in Figure 5.1). Different to the Barents Sea, strong snow metamorphism is present at the beginning of the winter season when snowfall events happened under warm conditions in mid December (see Figure 5.23, left). After an initial drop in the retrieved snow depth, the PR retrieval shows a strong response to the mid December snowfall event (snow depth increases around 15 cm). Then, until March, only moderate snowfall events happened. SNOWPACK simulates an increase in snow depth of 15 cm from mid December until end of February while the PR retrieval shows an overall increase of 4 cm. During this timeperiod, several drops in the retrieved snow depth are visible shortly before or after a snowfall event. At the beginning of March, a strong snowfall event under warm condition results in strong snow metamorphism. SNOWPACK simulates a thick melt-refreeze layer with a layer of rounded grains on top. In addition, layers of liquid water form in the snowpack (see Figure 5.23, right). The PR retrievals show a very sharp increase in snow depth of around 10 cm. Until beginning of April, several warm snowfall events happen which leads to strong responses in the satellite

retrieval. From April on, the air temperature reaching 0°C and melting starts (see Figure 5.23).

Central Arctic

Table 5.4 shows the initial snow- and sea ice profile for the SNOWPACK simulation in the Central Arctic (see green diamond in Figure 5.1). Here, the initial ice thickness (295 cm) was estimated from the CryoSat-2 ice thickness retrieval (Ricker et al., 2014), since the Huntemann et al. (2014) retrieval is only applied for ice thicknesses below 50 cm. For an initial snow depth estimation, the Warren climatology (Warren et al., 1999) was used. A typical MYI salinity profile was used with low salinity in the top layers of the ice.

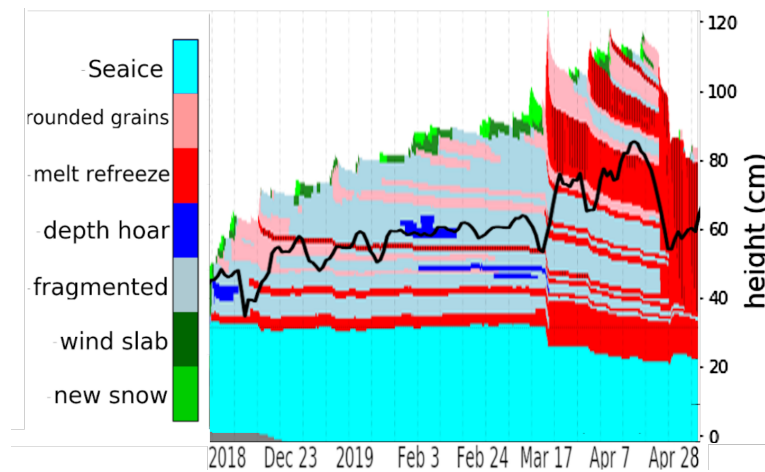


Figure 5.22: Same as Figure 5.17 but for the Labrador Sea

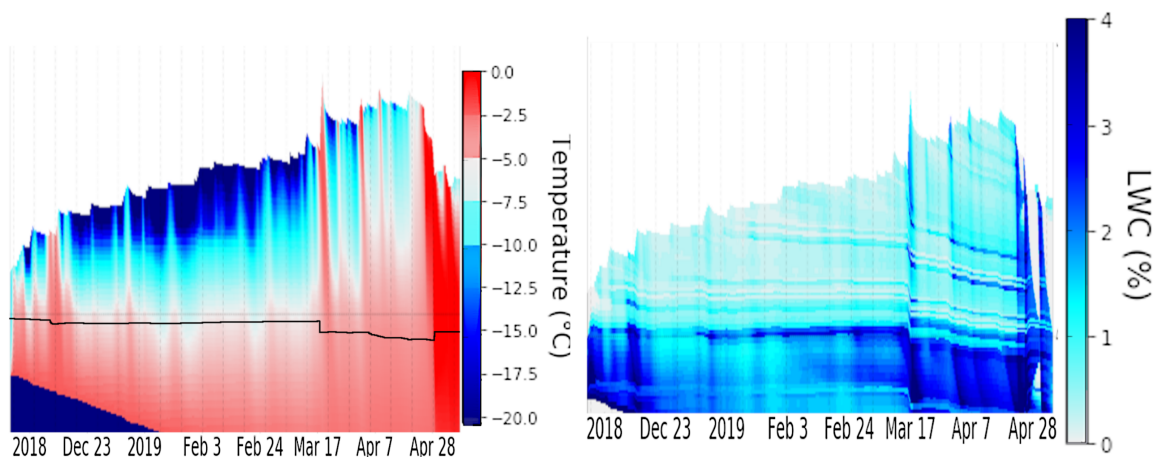


Figure 5.23: Temperature (left) and liquid water content (right) of the simulated snow-sea ice system in the Labrador Sea from December 2018 to April 2019.

Table 5.4: Same as Table 5.2 but for the SNOWPACK simulation in the Central Arctic.

	L (m)	T (K)	I_{frac}	V_{frac}	S (ppt)	F (W/m^2)
B					34	3
I1	2.8	269.0	0.95	0.05	6	
I2	0.02	265.0	0.95	0.05	2.4	
I3	0.02	264.0	0.95	0.05	1.0	
I4	0.04	263.0	0.95	0.05	0.8	
I5	0.03	262.0	0.95	0.05	0.5	
I6	0.04	261.0	0.95	0.05	0.0	
S1	0.25	259.0	0.29	0.71	0.0	
S2	0.10	256.0	0.34	0.64	0.0	

Figure 5.24 shows the same as Figure 5.17 but for the Central Arctic. The PR retrieval was applied for the whole winter season in order to gain further insights into its seasonal evolution over MYI. As mentioned before, SNOWPACK was initialised based on a snow depth estimate from climatology (Warren et al., 1999). However, inter-annual variability in the snow depth is not covered by the climatology and thus the estimated initial snow depth is not necessarily representing the conditions in November 2018. Therefore, the large differences between simulated and retrieved snow depth at the beginning of the season is not analysed further.

Similar to other areas, SNOWPACK simulates mainly fragmented snow with some layers of rounded grains which form after snowfall events. The initial depth hoar at the lower part of the snowpack disappears by the end of March.

In the Central Arctic, several snowfall events happen until mid of January and the snow depth simulated by SNOWPACK increases from 25 cm at beginning of November to 36 cm to the end of 2018. In the PR retrieval, almost no increase in snow depth is detected until mid of January 2019. This indicates that the signal observed by the satellites in early winter is dominated by the emission of the MYI. A slight increase in retrieved snow depth (4 cm) is found around 20 January just after a strong snowfall event. For the rest of the winter season, only a few, moderate snowfall events happened which are barely visible in the satellite retrieval.

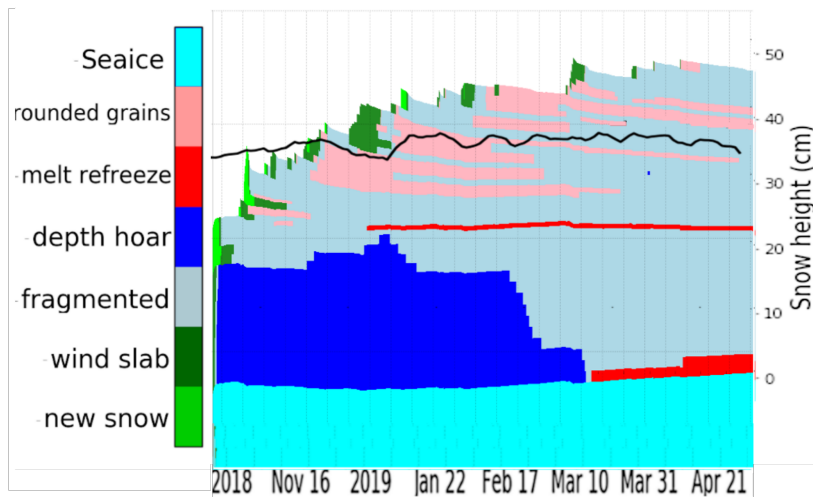


Figure 5.24: Same as Figure 5.17 but for the Central Arctic.

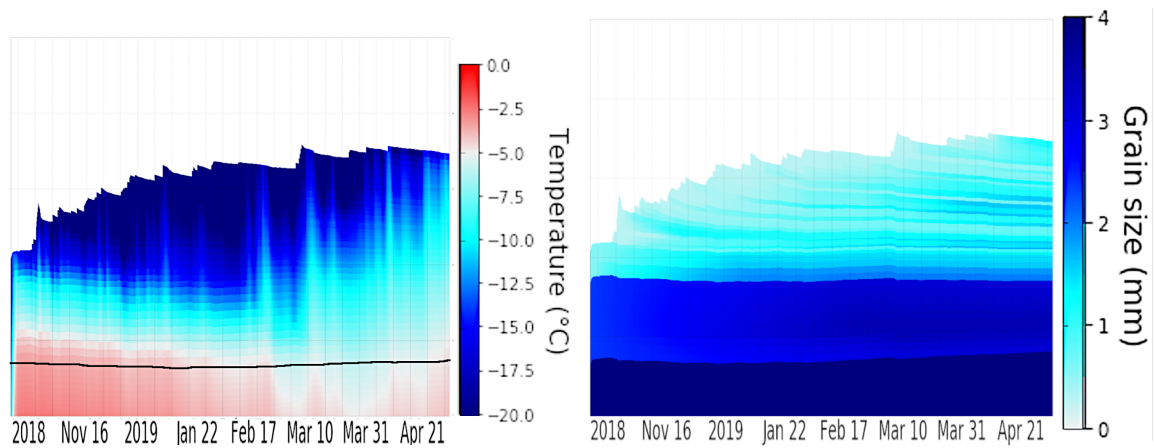


Figure 5.25: Same as Figure 5.23 but for the Central Arctic.

Summary

The comparison of the satellite retrieved snow depth with the SNOWPACK simulations revealed two interesting features:

- (i) A strong difference in the sensitivity of the satellite retrieved snow depth to snowfall events under cold conditions (snow metamorphism to wind slab and/or fragmented snow) or snowfall events under warm conditions (snow metamorphism to rounded grains and/or melt-refreeze) was found. In the first case, only a weak signal from the satellite retrieval was observed and often the retrieved snow depth slowly increases over several days after

the snowfall event. From all results obtained in this study, the average delay in increased snow depth (i.e., increase in snow depth reaches 95% of the total increase within 20 days after a snowfall event) after a snowfall event under cold conditions is five days. However, due to the limited amount of data, this is only a preliminary conclusion. In the second case (warm conditions), a strong increase in retrieved snow depth is found and the average delay is around two days.

(ii) Often, just before, or during a snowfall event, the retrieved snow depth initially drops and then starts increasing again. Possible reasons could be an increased snow drift/loss due to an increased wind speed during or shortly before the snowfall events (storm). Additionally, in the case of a fast warming during a snowfall event, the temperature gradient in the snow changes and this can influence the gradient ratio. However, the drop in retrieved snow depth (i.e., increase in GR) is, in most cases, much larger than the theoretical calculations suggest (see Figure 2.7).

For the data available in this study, only a low correlation ($R = -0.22$) between an increase in air temperature and a drop in snow depth is found. If a time lag of several days is allowed, the correlation between increased temperature and drop in snow depth increases to a maximum $R = -0.37$ at four days. This results show that part of the drop in retrieved snow depth can be related to strong changes of the temperature gradient in the snowpack. No significant correlation between the drop in retrieved snow depth and wind speed was found.

5.5 Discussion

The results of this evaluation and inter-comparison study show that comparing satellite retrieved snow depth to modelled snow depth which relies on reanalysis data is challenging due to a different sensitivity of the satellite retrievals to different snow- and meteorological conditions.

Overall, the different satellite retrievals (except the ML retrieval) agree within 5 cm during spring in most sectors of the Arctic and show a good performance when compared to spring snow depth observations from measurement campaigns (see sections 5.2 and 5.3). However, large differences in the seasonal cycle of the retrieved snow depth (see section 5.3) showed that additional training and evaluation data from early winter are crucially needed in order to develop a consistent snow depth product. The PR PR_{mix} and MC retrievals show the most reasonable seasonal cycle.

Unrealistic seasonal cycles in most sectors of the Arctic were produced by the NN and ML retrievals. Both retrievals use higher order models (neural network and multilinear regression) and the unreasonable seasonal evolution of the snow depth from these retrievals can be a

result of overfitting to spring data.

The simulations with SNOWPACK revealed the potential of using snow evolution models together with reanalysis data to improve the understanding of the sensitivity of satellite snow depth retrievals under different meteorological and snow conditions (see section 5.4). In theory, SNOWPACK simulations can be used to derive a proxy for snow properties to improve satellite based snow depth retrievals. However, simulations with SNOWPACK are computationally expensive and currently it is not feasible to use the model for Arctic-wide simulations. The SNOWPACK simulations performed here are limited to three small areas in the season 2018/2019 and no statistical significant relation between the retrieved snow depth and e.g., the grain type or meteorological conditions could be derived. From a larger dataset, it might be possible to derive such a relation which would then help to improve satellite based snow depth retrievals.

Overall, the results show that the error estimation for the PR retrieval is reasonable (see section 5.2), at least in spring under normal ice- and snow conditions (no flooding). Due to the delayed signal in the retrieved snow depth (see section 5.4) it might be more appropriate to use weekly or monthly averages for comparisons with reanalysis-based snow depth products. Due to the lack of evaluation data, no final conclusions can be drawn on how well the retrieval performs during early winter. However, PR and PR_{mix} both reproduce the expected increase in snow depth.

5.6 Conclusions

In this chapter, the new developed PR and PR_{mix} snow depth retrievals were evaluated with in-situ measurements and compared to three other satellite snow depth retrievals and simulations with the SNOWPACK model.

The inter-comparison revealed large differences between the different products in their seasonal cycle, especially in early winter (see Figure 5.11 to Figure 5.14). In spring, however, most of the retrievals are in good agreement. The evaluation with spring in-situ snow depth measurements showed a good performance of most of the snow depth retrievals in the Beaufort Sea and central Arctic. Overall, the PR retrieval performs best over FYI and the ML retrieval showed the best performance over MYI (see Table 5.1). However, in the Atlantic sector of the Arctic, all snow depth retrieval underestimate the measured snow depth, which could partly be related to flooding caused by high snow load by the time the in-situ measurements were taken (see figures 5.7 and 5.8). These result highlight the need of additional training data from other regions of the Arctic but also for the whole winter season. An comparison of the new derived retrieval with simulated snowpack using the SNOWPACK

model reveals the different sensitivity of the snow depth retrieval to different snow- and meteorological conditions. Especially in spring, a strong response of the satellite retrieval is found during snowfall events while during the cold season, the response was weaker. In addition, an average delay in increased snow depth of 5 (2) days compared to the snowfall event under cold (warm) conditions was found. Often shortly before, or during the snowfall event, an initial drop in the retrieved snow depth was found. First results indicate that this could be related to an increase in temperature which is often found during snowfall events ($R=-37$). Also an increased snow loss to leads and ridges due to an increased wind speed might play a role. However, for final conclusions, more SNOWPACK simulation need to be performed to analyse a larger amount of data.

Chapter 6

Conclusions and Outlook

6.1 Conclusions

The aim of this project was to develop a new passive microwave satellite snow depth on Arctic sea ice retrieval by incorporating newly available satellite observations (AMSR-E and AMSR2, 2002 - now) at lower microwave frequencies (e.g., 6.9 GHz and 10.7 GHz) and assess its uncertainties. In this chapter, the main findings of the thesis are summarised and discussed with respect to further improvements and development steps. The main results were presented in three chapters (chapter 3 to 5).

In chapter 3, a new snow depth on Arctic sea ice retrieval was developed using passive microwave satellite observations (Comiso et al., 2003; Maeda et al., 2016) and an extensive dataset of airborne snow depth observations from the Operation IceBridge (OIB) campaign (Newman et al., 2014). The results reported in this chapter were partly published in Rostosky et al. (2018). The main findings in this chapter are:

- (i) Using the gradient ratio of new available low frequency passive microwave satellite observations at 6.9 GHz and 18.7 GHz (GR(19/7); see equation 3.1), it is, for the first time, possible to retrieve snow depth on sea ice on a pan-Arctic scale. However, over Arctic MYI, the retrieval is currently limited to March and April, due to the strong influence of the underlying ice on the satellite observations in early and mid winter.
- (ii) A first evaluation with independent OIB snow depth observations showed a good performance of the new retrieval over FYI and a reasonable performance over MYI. Over FYI, deviations of the retrieved snow depth to the OIB snow depth are mostly below 5 cm, while over MYI, differences of ± 20 cm can be possible. The retrieval outperforms the most widely used passive microwave snow depth on Arctic sea ice retrieval developed by Markus and Cavalieri (1998).
- (iii) A comparison with snow depth data from climatology (Warren et al., 1999) highlights

the advantages of the new developed retrieval which is able to also cover the inter-annual variability of the snow depth on Arctic sea ice.

(iv) Based on all available data (season 2002/2003 to 2018/2019) a negative trend in monthly averaged snow depth of ($= -0.27$ cm/year) was found for March. This is consistent with the results found by Webster et al. (2014), who reported a negative trend in spring snow depth of -0.29 cm/year for the period from 1950 to 2013. The strongest negative trends were found in the Atlantic Sector and in the Kara and Laptev seas. In chapter 4 a Monte-Carlo model was used to estimate the uncertainty of the new derived retrieval. The analysis was based on state of the art microwave emission models for the snow-ice system (Tonboe, 2005) and the atmosphere and a large set of in-situ measurements obtained during the N-ICE2015 campaign (Granskog et al., 2016). The results reported in this chapter were partly published in Rostosky et al. (2020). The main findings in this chapter are:

(i) Unknown snow properties (e.g., grain type and grain size) have the highest contribution to the uncertainty of passive microwave snow depth retrievals. The error in retrieved snow depth due to unknown snow properties is 20% for a GR(19/7) and 24% for a GR(37/19) based snow depth retrieval.

(ii) Storms can cause rapid and long-term changes in the Arctic snowpack. A sensitivity study with the snow evolution model SNOWPACK (Wever et al., 2019) showed that a single storm event led to strong, persistent snow metamorphism and consequently strongly influenced the GR, even several days after the storm.

(iii) In general, lower frequency retrievals (i.e., based on GR(19/7)) have lower uncertainties than higher frequency retrievals (i.e., based on GR(37/19)) but are also less sensitive to changes in snow depth. Combining both, the uncertainty and the sensitivity to snow depth, it was shown that GR(37/19) has a better signal to noise ratio for snow depths below 38 cm. For deeper snow, GR(19/7) performs clearly better.

(iv) Based on the Monte Carlo model, the uncertainties of the newly derived retrieval was estimated. Overall, the uncertainties increase with increasing snow depth and are between 4 cm and 8 cm over FYI and 5 cm and 9 cm over MYI.

In chapter 5, the new snow depth retrieval was evaluated with spring in-situ measurements from eight different campaigns. In addition, an inter-comparison with three other existing passive microwave snow depth retrievals (Braakmann-Folgmann and Donlon, 2019; Kilic et al., 2019; Markus and Cavalieri, 1998) was carried out. The main findings of this chapter are:

(i) The evaluation of the retrieval shows that it performs well in most Arctic regions in spring. Over FYI, the newly derived retrieval has the lowest RMSE to the measurements compared to the three other passive microwave snow depth retrievals. An exception is the Atlantic

sector of the Arctic, where deep snow is common and flooding frequently occurs (Rösel et al., 2018b). Here, all snow depth retrievals underestimated the measured snow depth by at least 20 cm.

(ii) The evaluation with in-situ measurements showed that over FYI, the RMSE between the retrieved snow depth and measured snow depth (4.9 cm) is below the average uncertainty of the retrieval (derived in chapter 4) which indicates that at least in spring, the estimated uncertainty is accurate. Over MYI, the RMSE of the retrieval (8.1 cm) is slightly above the estimated uncertainty.

(iii) The evaluation of the seasonal cycle of the newly derived retrieval and the three other passive microwave retrievals revealed unrealistic snow depths from two other retrievals during early- and mid winter. These two snow depth retrievals (Braakmann-Folgmann and Donlon, 2019; Kilic et al., 2019) use less physical-based but more complex methods (neural-network; multi-linear regression) which might lead to better fits to the training data but fail to predict the snow depth for conditions outside of their training range (e.g., early winter conditions). Only the new developed retrieval and the retrieval developed by Markus and Cavalieri (1998) showed a reasonable seasonal evolution of the retrieved snow depth. These two retrievals are based on a simple empirical model (linear regression) with physical sense. As discussed in chapter 2 theoretical snow emission models predict a linear relation between snow depth and the GR in most cases. Within the scope of an increased use of complex machine learning techniques to derive new relations, these results highlight the need of a physical model to support the retrievals.

(iv) To further evaluate the seasonal evolution of the retrieved snow depth, the retrieval was compared to simulations of the Arctic snowpack based on the SNOWPACK model (Wever et al., 2019) and ERA5 reanalysis data (Hersbach and Dee, 2016). The analysis revealed that the sensitivity of the new retrieval to snowfall events strongly depends on the meteorological conditions. This is mainly due to different snow metamorphism under cold (main snow types: wind slap and fragmented snow) and under warm (main snow types: rounded grains and melt-refreeze) conditions. In comparison, the retrieval developed by Markus and Cavalieri (1998) showed a similar sensitivity to snowfall events but the retrievals developed by Braakmann-Folgmann and Donlon (2019) and Kilic et al. (2019) showed very little sensitivity to snowfall events, except for late spring.

Based on the new developed retrieval, two snow depth on Arctic sea ice datasets were published (see Appendix D) covering the winter periods from 2002 to 2011 (Rostosky et al., 2019b) and 2012 to 2018 (Rostosky et al., 2019a). This dataset was used in a snow depth retrieval inter-comparison study (Zhou et al., 2020) where the authors revealed large differences between the different snow depth retrievals. The differences were especially high

between satellite-based and reanalysis-based snow depth products.

One of central topics of this thesis was to develop a new snow depth on Arctic sea ice retrieval that can be used to evaluate and improve the snow depth simulated by coupled climate models. Snow depth is only poorly implemented in coupled climate models (Castro-Morales et al., 2017a) which leads to high uncertainties in the estimation of e.g., the distribution of snow on sea ice or the ocean-atmospheric heat fluxes (Castro-Morales et al., 2014, 2017a; Webster et al., 2018), highlighting the need of more evaluation. For this purpose, it is crucial to evaluate the quality of the new retrieval. In addition, for assimilation, accurate uncertainties are essential.

An accurate uncertainty estimation for early- and mid winter remains challenging since no evaluation data exists outside of spring. The uncertainty of the retrieval derived in chapter 4 is based on in-situ observations from late winter to spring (20 January to 31 May) and thus might be not representative for early winter. Especially at the start of the freezing season, also thin ice is a sources of uncertainty. When the ice is thin (i.e., less than 20 cm thick), the observations at 6.9 GHz may be influenced by the ocean (Ulaby and Long, 2014b) and consequently the GR is influenced as well. As a result, negative snow depths may be retrieved at the ice edge in September and October. For the time period available (2002 to now), no negative snow depths were found from November onward. Therefore, the retrieval is currently applied from November to the onset of melt.

When the ice concentration is below 100%, the satellite observations are a mixture of the signal from open water and from ice and thus the GR is higher than over pure ice. To account for that open water tiepoints are used to correct the satellite signal (Ivanova et al., 2015). However, the tiepoints themselves have uncertainties due to the presence of thin ice or wind roughened water (Ivanova et al., 2015) and thus increase the uncertainty of the retrieved snow depth, especially when the ice concentration is low. To mitigate this effect, the retrieval is currently only applied when the ice concentration is above 80%.

An additional source of uncertainty, which was not assessed in this thesis due to the lack of data and theoretical models, is the impact of large scale ice roughness (e.g., due to pressure ridges) on the retrieval. It has been found that the Markus and Cavalieri (1998) snow depth retrieval, which uses a similar method as the snow depth retrieval developed in this thesis, is influenced by sea ice roughness (Markus et al., 2006a; Stroeve et al., 2006). Further analysis of the retrieval is needed to assess its performance over e.g., rough or thin ice where the estimated uncertainty might be too low or the results might be biased.

So far, the retrieval over MYI is limited to March and April. However, especially for the comparison with model results and to improve sea ice thickness estimates from altimetry (Kern et al., 2015), it is important to also have snow depth observations over MYI for the

whole winter season. A comparison of the snow depth over MYI retrieved during the whole season with simulated snow depth from the SNOWPACK model in chapter 5 showed that the retrieval is not able to detect snowfall events during early winter (November to December) and only in January, an increase in retrieved snow depth, collocated with a major snowfall event, was found. Therefore, it is of central importance to further improve the knowledge of the microwave emission of snow on MYI, especially shortly after freeze-up. The measurements obtained during the ongoing MOSAiC campaign (<http://www.mosaic-expedition.org>, accessed 15 November 2019) may provide the needed information to further constrain the satellite observations over MYI.

Regardless the need of further evaluation and improvements, the new snow depth dataset can already be used to evaluate or improve snow depth output from climate models. In a study using an early version of the snow depth product (status November 2018) Fritzner et al. (2019) showed that assimilating spring snow depth into the metroms model system (Kristensen et al., 2017) leads to not only an improvement in the modelled snow depth but also improves the modelled ice concentration and ice thickness.

Further comparison of the new snow depth dataset with simulated snow depth from coupled climate models can be useful for further evaluation of the new snow depth retrieval. However, as concluded in chapter 5, a direct comparison of retrieved and simulated snow depth is challenging since the response of the satellite retrieval to snowfall events can be delayed by up to five days, depending on the snow metamorphism. In addition, uncertainties in the parametrisation of snow accumulation at ridges and snow depletion in the climate models can lead to large errors in the simulated snow depth.

6.2 Outlook

The newly derived snow depth on Arctic sea ice retrieval including the extensive uncertainty estimation provides a good basis for an operational snow depth product. However, the study in chapter 5 revealed that further evaluation is needed which requires additional snow depth observations covering different Arctic regions and seasons. Right now, such data does not exist and up to now, no future missions on large scale snow depth surveys during early winter are known which would help to close the gap. A different option for further improvement or evaluation of the retrieval could be an extensive study using the SNOWPACK model forced with reanalysis data. In this study, no significant correlation between e.g., air temperature and sensitivity of the satellite retrieval to snowfall was found. This, however, might be due to the limited dataset used for the analysis. A more extensive study is out of the scope of this work but can be useful to further deepen the understanding in how the satellite retrieval

behaves under different meteorological conditions and, especially, in early winter.

In the published snow depth datasets (see appendix D), reanalysis 2 m temperature data were used to flag possible melt in the snow. It is, however, more convenient to use snow melt detection algorithms based on satellite observations as e.g, proposed by Arndt and Haas (2019) for snow on Antarctic sea ice since the liquid water content in snow can reach a critical amount even when the air temperature is still negative (see chapter 5).

To summarise, snow depth on Arctic sea ice was identified as a key quantity for improving the understanding of the rapid Arctic climate change (Webster et al., 2018). The newly developed snow depth retrieval including an extensive uncertainty estimation, provides an important contribution to Arctic climate research. However, further work needs to be done on improving and further evaluating the performance of the retrieval during early winter.

References

- Aaboe, S., Breivik, L. A., Soerensen, A., Eastwood, S., and Lavernge, T. (2016). Global sea ice edge and type user's manual—v13. *Technical report/SAFOSI/CDOP2/MET-Norway/TEC/MA/205, EUMETSAT OSI SAF—Ocean and Sea Ice Satellite Application Facility.*
- Aires, F., Prigent, C., Bernardo, F., Jiménez, C., Saunders, R., and Brunel, P. (2011). A tool to estimate land-surface emissivities at microwave frequencies (TELSEM) for use in numerical weather prediction. *Quarterly Journal of the Royal Meteorological Society*, 137(656):690–699.
- Arndt, S. and Haas, C. (2019). Spatiotemporal variability and decadal trends of snowmelt processes on antarctic sea ice observed by satellite scatterometers. *The Cryosphere*, 13(7):1943–1958.
- Arndt, S., Meiners, K. M., Ricker, R., Krumpfen, T., Katlein, C., and Nicolaus, M. (2017). Influence of snow depth and surface flooding on light transmission through Antarctic pack ice. *J. Geophys. Res. Oceans*, 122:2108–2119.
- Bartelt, P. and Lehning, M. (2002). A physical SNOWPACK model for the swiss avalanche warning part I: numerical model. *Cold Regions Science and Technology*, 35:123–145.
- Blanchard-Wrigglesworth, E., Farrell, S. L., Newman, T., and Bitz, C. M. (2015). Snow cover on Arctic sea ice in observations and an Earth System Model. *Geophysical Research Letters*, 42(10):342–348.
- Blanchard-Wrigglesworth, E., Webster, M. A., Farrell, S. L., and Bitz, C. M. (2018). Reconstruction of Snow on Arctic Sea Ice. *Journal of Geophysical Research: Oceans*, 123(5):3588–3602.
- Boisvert, L. N., Webster, M. A., Petty, A. A., Markus, T., Bromwich, D. H., and Cullather, R. I. (2018). Intercomparison of Precipitation Estimates over the Arctic Ocean and Its Peripheral Seas from Reanalyses. *Journal of Climate*, 31(20):8441–8462.
- Braakmann-Folgmann, A. and Donlon, C. (2019). Estimating snow depth on Arctic sea ice using satellite microwave radiometry and a neural network. *The Cryosphere*, 13(9):2421–2438.
- Brucker, L. and Markus, T. (2013). Arctic-scale assessment of satellite passive microwave-derived snow depth on sea ice using operation iceBridge airborne data. *Journal of geophysical research*, 118:2892–2905.

- Castro-Morales, K., Kauker, F., Losch, M., Hendricks, S., Riemann-Campe, K., and Gerdes, R. (2014). Sensitivity of simulated Arctic sea ice to realistic ice thickness distributions and snow parameterizations. *Journal of Geophysical Research: Oceans*, 119(1):559–571.
- Castro-Morales, K., Ricker, R., and Gerdes, R. (2017a). Regional distribution and variability of model-simulated Arctic snow on sea ice. *Polar Science*, 13:33–49.
- Castro-Morales, K., Ricker, R., and Gerdes, R. (2017b). Regional distribution and variability of model-simulated arctic snow on sea ice. *Polar Science*, 13:33–49.
- Cavalieri, D. J., Markus, T., and Comiso, J. C. (2014). AMSR-E/aqua daily L3 25 km brightness temperature sea ice concentration polar grids, version 3. *NASA National Snow and Ice Data Center Distributed Active Archive Center*.
- Cavalieri, D. J., Markus, T., Ivanoff, A., Miller, J. A., Brucker, L., Sturm, M., Maslanik, J. A., Heinrichs, J. F., Gasiewski, A. J., Leuschen, C., Krabill, W., and Sonntag, J. (2012). A comparison of snow depth on sea ice retrievals using airborne altimeters and an AMSR-E simulator. *IEEE Transactions on Geoscience and Remote Sensing*, 50(8):3027–3040.
- Cavalieri, D. J., Markus, T., Maslanik, J. and Sturm, M., and Lobl, E. (2003). March 2003 EOS Aqua AMSR-E Arctic Sea Ice Field Campaign. *IEEE Transactions on Geoscience and Remote Sensing*, 44(11):3003–3008.
- Cavalieri, D. J., T. M. and Comiso., J. C. (2014a). AMSR-E/Aqua Daily L3 12.5 km Brightness Temperature, Sea Ice Concentration, Snow Depth Polar Grids, Version 3. status 03 January 2020.
- Cavalieri, D. J., T. M. and Comiso., J. C. (2014b). AMSR-E/Aqua Daily L3 25 km Brightness Temperature Sea Ice Concentration Polar Grids, Version 3. status: 03 January 2020.
- Chang, A., Foster, J., and Hall, D. (1987). NIMBUS- 7 SMMR DERIVED GLOBAL SNOW COVER PARAMETERS. *Annals of Glaciology*, 9.
- Che, T., Li, X., Jin, R., Armstrong, R., and Zhang, T. (2008). Snow depth derived from passive microwave remote-sensing data in China. *Annals of Glaciology*, 49:145–154.
- Choudhury, B. J., Schmugge, T. J., Chang, A., and Newton, R. W. (1979). Effect of surface roughness on the microwave emission from soils. *Journal of Geophysical Research: Oceans*, 84(C9):5699–5706.
- Christos, E. P. and Hoi, Y. (2001). Uncertainty estimation and monte carlo simulation method. *Flow Measurement and Instrumentation*, 12(4):291 – 298.
- Cohen, L., Hudson, S. R., Walden, V. P., Graham, R. M., and Granskog, M. A. (2017). Meteorological conditions in a thinner arctic sea ice regime from winter to summer during the Norwegian Young Sea Ice expedition (N-ICE2015). *J. Geophys. Res. Atmos.*, 122:7235–7259.
- Colbeck, S. C. (1986). Classification of seasonal snow cover crystals. *Water Resources Research*, 22(9S):59S–70S.

- Comiso, J. C., Cavalieri, D. J., and Markus, T. (2003). Sea ice concentration, ice temperature, and snow depth using AMSR-E data. *IEEE Transactions on Geoscience and Remote Sensing*, 42(2):243–252.
- Dee, D. P., Uppala, S. M., Simmons, A. J., Berrisford, P., Poli, P., Kobayashi, S., and et al. (2011). The ERA-Interim reanalysis: Configuration and performance of the data assimilation system. *Quarterly Journal of the Royal Meteorological Society*, 137(656):553–597.
- Du, J., Kimball, J. S., Shi, J., Jones, L. A., Wu, S., Sun, R., and et al. (2014). Inter-calibration of satellite passive microwave land observations from AMSR-E and AMSR2 using overlapping FY3B-MWRI sensor measurements. *Remote Sensing*, 6(9):8594–8616.
- Dupont, F., Picard, G., Royer, A., Fily, M., Roy, A., Langlois, A., and et al. (2014). Modeling the microwave emission of bubbly ice: Applications to blue ice and superimposed ice in the Antarctic and Arctic. *IEEE Transactions on Geoscience and Remote Sensing*, 52(10):6639–6651.
- Evans, K. F. and, S. G. L. (1995). Free access microweve radiative transfer through clouds composed of realistically shaped ice crystals. Part II. Remote sensing of ice clouds. *J. Atmos. Sci.*, 52(11):2058–2072.
- Farrell, S. L., Kurtz, N., Connor, L. N., Elder, B. C., Leuschen, C., Markus, T., McAdoo, D. C., Panzer, B., Richter-Menge, J., and Sonntag, J. G. (2012). A First Assessment of IceBridge Snow and Ice Thickness Data Over Arctic Sea Ice. *IEEE Transactions on Geoscience and Remote Sensing*, 50(6):2098–2111.
- Fritzner, S., Graverson, R., Christensen, K. H., Rostosky, P., and Wang, K. (2019). Impact of assimilating sea ice concentration, sea ice thickness and snow depth in a coupled ocean–sea ice modelling system. *The Cryosphere*, 13(2):491–509.
- Fung, A. K. and Eom, H. J. (1982). Application of a combined rough surface and volume scattering theory to sea ice and snow backscatter. *IEEE Tansaction on Geoscience and Remote Sensing*, 20(4).
- Graham, R. M., Cohen, L., Petty, A. A., Boisvert, L. N., Rinke, A., Hudson, S. R., Nicolaus, M., and Granskog, M. A. (2017). Increasing frequency and duration of arctic winter warming events. *Geophysical Research Letters*, 44(13):6974–6983.
- Graham, R. M., Itkin, P., Meyer, A., Sundfjord, A., Spreen, G., Smedsrud, L. H., Liston, G. E., Cheng, B., and et al. (2019). Winter storms accelerate the demise of sea ice in the Atlantic sector of the Arctic Ocean. *Nature Scientific Reports*, 9.
- Granskog, M. A., Assmy, P., Gerland, S., Spreen, G., Steen, H., and Smedsrud, L. H. (2016). Arctic research on thin ice - Consequences of Arctic sea ice loss. *Eos, Trans. Am. Geophys. Union*, 97(5):22–26.
- Granskog, M. A., Ilker, F., Rinke, A., and Steen, H. (2017). Atmosphere-Ice-Ocean-Ecosystem Processes in a Thinner Arctic Sea Ice Regime: The Norwegian Young Sea ICE (N-ICE2015) Expedition. *Journal of Geophysical Research: Ocean*, 123:1586–1594.

- Grenfell, T. C. (2015). Surface-based passive microwave studies of multiyear sea ice. *J. Geophys. Res. Earth Surf.*, 120:346–362.
- Grenfell, T. C. and Warren, S. G. (1999). Representation of a nonspherical ice particle by a collection of independent spheres for scattering and absorption of radiation. *Journal of Geophysical Research: Atmospheres*, 104(D24):31697–31709.
- Guerreiro, K., Fleury, S., Zakharova, E., Remy, F., and Kouraev, A. (2016). Potential for estimation of snow depth on arctic sea ice from CryoSat-2 and SARAL/Altika missions. *Remote Sensing of Environment*, 186:339–249.
- Hersbach, H. and Dee, D. (2016). ERA5 reanalysis is in production. *ECMWF Newsletter*, 147:7. accessed 15 December 2019.
- Hogan, R. J., Honeyager, R., Tyynelä, J., and Kneifel, S. (2017). Calculating the millimetre-wave scattering phase function of snowflakes using the self-similar rayleigh-gans approximation. *Quarterly Journal of the Royal Meteorological Society*, 143(703):834–844.
- Hogan, R. J. and Westbrook, C. D. (2014). Equation for the microwave backscatter cross section of aggregate snowflakes using the self-similar rayleigh-gans approximation. *Journal of the Atmospheric Sciences*, 71(9):3292–3301.
- Holmes, C., Holland, P., and Bracegirdle, T. (2019). Compensating Biases and a Noteworthy Success in the CMIP5 Representation of Antarctic Sea Ice Processes. *Geophysical Research Letters*, 46(8):4299–4307.
- Holt, B. (2019). On-Ice Arctic Sea Ice Thickness Measurements by Auger, Core, and Electromagnetic Induction, from the Late 1800s Onward, Version 2. accessed: 15 January 2019.
- Huber, P. J. (1981). *Robust statistics*. John Wiley and Sons Inc., New York.
- Hudson, S. R., Cohen, L., Kayser, M., Maturilli, M., Kim, J.-H., Park, S.-J., Moon, W., and Granskog, M. A. (2017). N-ICE2015 atmospheric profiles from radiosondes.
- Huntemann, M., Heygster, G., Kaleschke, L., Krumpen, T., Mäkynen, M., and Drusch, M. (2014). Empirical sea ice thickness retrieval during the freeze-up period from SMOS high incident angle observations. *The Cryosphere*, 8:439–451.
- Ivanova, N., Pedersen, L. T., Tonboe, R. T., Kern, S., Heygster, G., Lavergne, T., and et al. (2015). Inter-comparison and evaluation of sea ice algorithms: Towards further identification of challenges and optimal approach using passive microwave observations. *The Cryosphere*, 9(5):1797–1817.
- Josberger, E. G. and Mognard, N. M. (2002). A passive microwave snow depth algorithm with a proxy for snow metamorphism. *Hydrological Processes*, 16(8).
- Kanagaratnam, P., Markus, T., Lytle, V., Heavey, B., Jansen, P., Prescott, G., and et al. (2007). Ultrawideband radar measurements of thickness of 9 snow cover over sea ice. *IEEE Transactions on Geoscience and Remote Sensing*, 45(9):2715–2724.

- Karstens, U., Simmer, C., and Ruprecht, E. (1994). Remote sensing of cloud liquid water. *Meteorol. Amtos. Phys.*, (54):157–171.
- Kern, S., Khvorostovsky, K., Skourup, H., Rinne, E., Parsakhoo, Z. S., Djepa, V., and et al. (2015). The impact of snow depth, snow density and ice density on sea ice thickness retrieval from satellite radar altimetry: Results from the ESA-CCI Sea Ice ECV Project Round Robin Exercise. *The Cryosphere*, 9(1):37–52.
- Kern, S. and Ozsoy, B. (2019). An Attempt to Improve Snow Depth Retrieval Using Satellite Microwave Radiometry for Rough Antarctic Sea Ice. *Remote Sensing*, 11(19).
- Kilic, L., Tonboe, R. T., Prigent, C., and Heygster, G. (2019). Estimating the snow depth, the snow–ice interface temperature, and the effective temperature of Arctic sea ice using Advanced Microwave Scanning Radiometer 2 and ice mass balance buoy data. *The Cryosphere*, 13(4):1283–1296.
- King, J., Howell, S., Derksen, C., Rutter, N., Toose, P., Beckers, J. F., and et al. (2015). Evaluation of Operation IceBridge quick-look snow depth estimates on sea ice. *Geophysical Research Letters*, 42:9302–9310.
- König, M., Winther, J.-G., and Isaksson, E. (2001). Measuring snow and glacier ice properties from satellite. *Reviews of Geophysics*, 39(1):1–27.
- Kristensen, N., Debernard, J., Maartensson, S., Wans, K., and Hedstrom, K. (2017). metno/metroms. status: 09 March 2020.
- Krol, Q. and Löwe, H. (2016). Relating optical and microwave grain metrics of snow: the relevance of grain shape. *The Cryosphere*, 10(6):2847–2863.
- Kumar, A., Perlwitz, J., Eischeid, J., Quan, X., Xu, T., Zhang, T., and et al. (2010). Contribution of sea ice loss to Arctic amplification. *Geophysical Research Letters*, 37(L201701).
- Kurtz, N., Farrell, S. L., Studinger, M., Galin, N., Harbeck, J., Lindsay, R., and et al. (2013a). Sea ice thickness, freeboard, and snow depth products from Operation IceBridge airborne data. *The Cryosphere*, 7(4):1035–1056.
- Kurtz, N., Studinger, M., Harbeck, J., Onana, V., and Farrell, S. (2013b). IceBridge sea ice freeboard, snow depth, and thickness, version 1.
- Kurtz, N. T. and Farrell, S. L. (2011). Large-scale surveys of snow depth on Arctic sea ice from Operation iceBridge. *Geophysical Research Letters*, 38(L20505).
- Kwok, R., Kurtz, N. T., Brucker, L., Ivanoff, A., Newman, T., Farrell, S. L., King, J., and et al. (2017). Intercomparison of snow depth retrievals over Arctic sea ice from radar data acquired by Operation iceBridge. *The Cryosphere*, 11(6):2571–2693.
- Kwok, R. and Rothrock, D. A. (2009). Decline in Arctic sea ice thickness from submarine and ICESat records: 1958–2008. *Geophysical Research Letters*, 36(15).
- Lavergne, T., Eastwood, S., Teffah, Z., Schyberg, H., and Breivik, L.-A. (2010). Sea ice motion from low-resolution satellite sensors: An alternative method and its validation in the Arctic. *Journal of Geophysical Research: Oceans*, 115(C10).

- Lawrence, I. R., Tsamados, M. C., Stroeve, J. C., Armitage, T. W. K., and Ridout, A. L. (2018). Estimating snow depth over arctic sea ice from calibrated dual-frequency radar freeboards. *The Cryosphere*, 12(11):3551–3564.
- Laxon, S. W., Giles, K. A., Ridout, A. L., Wingham, D. J., Willatt, R., Cullen, R., Kwok, R., and et al. (2013). CryoSat-2 estimates of Arctic sea ice thickness and volume. *Geophysical Research Letters*, 40(4):732–737.
- Lehning, M., Bartelt, P., Brown, B., and Fierz, C. (2002a). A physical SNOWPACK model for the swiss avalanche warning part III: meteorological forcing, thin layer formation and evaluation. *Cold Regions Science and Technology*, 35:169–184.
- Lehning, M., Bartelt, P., Brown, B., Fierz, C., and Satyawali, P. (2002b). A physical SNOWPACK model for the swiss avalanche warning part II: Snow microstructure. *Cold Regions Science and Technology*, 35:147–167.
- Leinss, S., Lemmetyinen, J., and Hajnsek, I. (2015). Snow Water Equivalent of Dry Snow Measured by Differential Interferometry. *IEEE Journal of Selected Topics in Applied Earth Observations and Remote Sensing*, 8(8):3773–3790.
- Liljegred, J. C., Boukabaram, S. A., Cady-Pereira, K., and Clough, S. A. (2005). The effect of the half-width of the 22-ghz water vapor line on retrievals of temperature and water vapor profiles with a 12-channel microwave radiometer. *IEEE Transactions on Geoscience and Remote Sensing*, 43:1102–1108.
- Lindsay, R., Wensnaham, M., Schweiger, A., and Zhang, J. (2013). Evaluation of seven different atmospheric reanalysis products in the Arctic. *Journal of Geophysical Research: Atmospheres*, 27(7):2588–2606.
- Liston, G. E., Polashenski, C., Roesel, A., Itkin, P., King, J., and Merkouriadi, I. (2018). A distribution snow-evolution model for sea-ice applications (SnowModel). *Journal of Geophysical Research: Oceans*, 123:3786–3810.
- Liu, J., Zhang, Y., Cheng, X., and Hu, Y. (2019). Retrieval of Snow Depth over Arctic Sea Ice Using a Deep Neural Network. *Remote Sensing*, 11(23).
- Liu, Q., Weng, F., and English, S. J. (2011). An Improved Fast Microwave Water Emissivity Model. *IEEE Transactions on Geoscience and Remote Sensing*, 49(4):1238–1250.
- Löwe, H. and Picard, G. (2015). Microwave scattering coefficient of snow in MEMLS and DMRT-ML revisited: the relevance of sticky hard spheres and tomography-based estimates of stickiness. *The Cryosphere*, 9(6):2101–2117.
- Löwe, H., Riche, F., and Schneebeli, M. (2013). A general treatment of snow microstructure exemplified by an improved relation for thermal conductivity. *The Cryosphere*, 7(5):1473–1480.
- Lu, J., Heygster, G., and Spreen, G. (2018). Atmospheric correction of sea ice concentration retrieval for 89 GHz AMSR-E observations. *IEEE Journal of Selected Topics in Applied Earth Observation and Remote Sensing*, 11(5).

- Löwe, H., Spiegel, J., and Schneebeli, M. (2011). Interfacial and structural relaxations of snow under isothermal conditions. *Journal of Glaciology*, 57(203):499–510.
- Lüpkes, C., Vihma, T., Jakobson, E., König-Langlo, G., and Tetzlaff, A. (2010). Meteorological observations from ship cruises during summer to the central arctic: A comparison with reanalysis data. *Geophysical Research Letters*, 37(9).
- Maaß, N., Kaleshke, L., Tian-Kunze, X., Itkin, P., King, J., and Merkouriadi, I. (2013). Snow thickness retrieval over thick Arctic sea ice using SMOS satellite data. *The Cryosphere*, 7(6):1971–1989.
- Maeda, T., Taniguchi, Y., and Imaoka, K. (2016). GCOM-W1 AMSR2 Level 1R Product: Dataset of Brightness Temperature Modified Using the Antenna Pattern Matching Technique. *IEEE Transactions on Geoscience and Remote Sensing*, 54(2).
- Markus, T. and Cavalieri, D. J. (1998). Snow depth distribution over sea ice in the southern ocean from satellite passive microwave data. *Antarctic Research Series*, 74:19–39.
- Markus, T. and Cavalieri, D. J. (2000). An Enhancement of the NASA Team Sea Ice Algorithm. *IEEE Transactions on Geoscience and Remote Sensing*, 38(3).
- Markus, T., Cavalieri, D. J., Gasiewski, A. J., Klein, M., Maslanik, J. A., Powell, D. C., Stankov, B. B., Stroeve, J. C., and Sturm, M. (2006a). Microwave signatures of snow on sea ice: Observations. *IEEE Transactions on Geoscience and Remote Sensing*, 44(11):3081–3090.
- Markus, T., Massom, R., Worby, A., Lytle, V., Kurtz, N., and Maksym, T. (2011). Freeboard, snow depth and sea-ice roughness in East Antarctica from in situ and multiple satellite data. *Annals of Glaciology*, 52(57):242–248.
- Markus, T., Powell, D. C., and Wang, J. R. (2006b). Sensitivity of passive microwave snow depth retrievals to weather effects and snow evolution. *IEEE Transactions on Geoscience and Remote Sensing*, 44(11):3091–3102.
- Maslowsky, W., Kinney, J. C., Higgins, M., and Roberts, A. (2012). The Future of Arctic Sea Ice. *Annual Review Earth Planet. Science*, 40.
- Mätzler, C. (1987). Applications of the Interaction of Microwaves with the Natural Snow Cover. *Remote Sensing Review*, 2":259–387.
- Mätzler, C. (1997). Autocorrelation functions of granular media with free arrangement of spheres, spherical shells or ellipsoids. *Journal of Applied Physics*, 81(3):1509–1517.
- Mätzler, C. (1998). Improved Born approximation for scattering of radiation in a granular medium. *Journal of Applied Physics*, 83:6111–6117.
- Mätzler, C. (2002). Relation between grain-size and correlation length of snow. *Journal of Glaciology*, 48(162).
- Mätzler, C., editor (2006). *Thermal Microwave Radiation: Applications for Remote Sensing*, volume 52. IEE Electromagnetic Waves Series, London, UK.

- Mätzler, C. and Wiesmann, A. (1999). Extension of the Microwave Emission Model of Layered Snowpacks to coarse-grained snow. *Remote Sensing of Environment*, 70(3):317–325.
- Meier, W. N., Wilcox, H., Hardman, M. A., and S., S. J. (2019). DMSP SSM/I-SSMIS Daily Polar Gridded Brightness Temperatures.
- Merkouriadi, I., Gallet, J.-C., Graham, R. M., Liston, G. E., Polashenski, C., Rösel, A., and Gerland, S. (2017a). Winter snow conditions on Arctic sea ice north of svalbard during the Norwegian young sea ICE (N-ICE2015) expedition. *J. Geophys. Res. Atmos.*, 122:10.837–10.854.
- Merkouriadi, I., Gallet, J.-C., Liston, G., Polashenski, C., Itkin, P., King, J., Espeseth, M., Gierisch, A., Oikkonen, A., Orsi, A., and Gerland, S. (2017b). N-ICE2015 snow pit data.
- Mischenko, M. I. and Travis, L. D. (1994). T-matrix computations of light scattering by large spheroidal particles. *Optics Communications*, 109:16–21.
- Nandan, V., Geldsetzer, T., Yackel, J., Mahmud, M., Scharien, R., Howell, S., King, J., Ricker, R., and Else, B. (2017). Effect of Snow Salinity on CryoSat-2 Arctic First-Year Sea Ice Freeboard Measurements. *Geophysical Research Letters*, 44(20):10.419–10.426.
- Newman, T., Farrell, S. L., Richter-Menge, J., Elder, B., Connor, L., Kurtz, N., and et al. (2014). Assessment of radar-derived snow depth measurements over Arctic sea ice. *Journal of Geophysical Research: Oceans*, 119:8578–8602.
- Onstott, R. G., Grenfell, T. C., Mätzler, C., Luther, C. A., and Svendsen, E. A. (1987). Evolution of microwave sea ice signatures during early summer and midsummer in the marginal ice zone. *Journal of Geophysical Research*, 92(C7):6825–6835.
- Perovich, D. K., Grenfell, T. C., Light, B., and Hobbs, P. V. (2002). Seasonal evolution of the albedo of multiyear Arctic sea ice. *Journal of Geophysical Research*, 107(C10):8044.
- Perovich, D. K., Meier, W. Tschudi, M., Farrell, S. L., Hendricks, S., Gerland, S., Haas, C., and et al. (2017a). Sea ice, Arctic report card 2017.
- Perovich, D. K., Meier, W., T., M., Farrell, S. L., Hendricks, S., Gerland, S., and et al. (2017b). Sea ice, arctic report card 2017.
- Perovich, D. K. and Richter-Menge, J. A. (2015). Regional variability in sea ice melt in a changing arctic. *Philosophical Transactions of the Royal Society A*, 373(2045).
- Petty, A. A., Webster, M., Boisvert, L., and Markus, T. (2018). The NASA Eulerian Snow on Sea Ice Model (NESOSIM) v1.0: initial model development and analysis. *Geoscientific Model Development*, 11(11):4577–4602.
- Picard, G., Brucker, L., Roy, A., Dupont, F., Fily, M., Royer, A., and Harlow, C. (2013). Simulation of the microwave emission of multi-layered snowpacks using the Dense Media Radiative transfer theory: the DMRT-ML model. *Geoscientific Model Development*, 6(4):1061–1078.

- Picard, G., Sandell, M., and Löwe, H. (2018). SMRT: An active/passive microwave radiative transfer model for snow with multiple microstructure and scattering formulations (v1.0). *Geoscientific Model Development Discussion*.
- Pithan, F., Medeiros, B., and Mauritsen, T. (2014). Mixed-phase clouds cause climate model biases in arctic wintertime temperature inversions. *Climate Dynamics*, 43:289–303.
- Powell, D. C., Markus, T., Cavalieri, D. J., Gasiewski, A. J., Klein, M., Maslanik, J. A., Stroeve, J. C., and Sturm, M. (2006). Microwave signatures of snow on sea ice: Modeling. *IEEE Transactions on Geoscience and Remote Sensing*, 44(11):3091–3102.
- Prigent, C., Aires, F., Wang, D., Fox, S., and Harlow, C. (2017). Sea-surface emissivity parametrization from microwaves to millimetre waves. *Quarterly Journal of the Royal Meteorological Society*, 143(702):596–605.
- Proksch, M., Löwe, H., and Schneebeli, M. (2015). Density, specific surface area, and correlation length of snow measured by high-resolution penetrometry. *Journal of Geophysical Research: Earth Surface*, 20(4).
- Provost, C., Sennéchaël, N., Miguët, J., Itkin, P., Rösel, A., Koenig, Z., Villaceros-Robineau, N., and Granskog, M. A. (2017). Observations of flooding and snow-ice formation in a thinner Arctic sea-ice regime during the N-ICE2015 campaign: Influence of basal ice melt and storms. *Journal of Geophysical Research: Oceans*, 122(9):7115–7134.
- Pulliaainen, J. (2006). Mapping of snow water equivalent and snow depth in boreal and sub-arctic zones by assimilating space-borne microwave radiometer data and ground-based observations. *Remote Sensing of Environment*, (101):257–269.
- Riche, F. and Schneebeli, M. (2013). Thermal conductivity of snow measured by three independent methods and anisotropy considerations. *The Cryosphere*, 7(1):217–227.
- Ricker, R., Hendricks, S., Helm, V., Skourup, H., and Davidson, M. (2014). Sensitivity of CryoSat-2 Arctic sea-ice freeboard and thickness on radar-waveform interpretation. *The Cryosphere*, 8(4):1607–1622.
- Rösel, A., Itkin, P., King, J., Divine, D., Wang, C., Granskog, M. A., Krumpfen, T., and Gerland, S. (2018a). Thin Sea Ice, Thick Snow, and Widespread Negative Freeboard Observed During N-ICE2015 North of Svalbard. *Journal of Geophysical Research: Oceans*, 123(2):1156–1176.
- Rösel, A., Itkin, P., King, J., Divine, D., Wang, C., Granskog, M. A., Krumpfen, T., and Gerland, S. (2018b). Thin Sea Ice, Thick Snow, and Widespread Negative Freeboard Observed During N-ICE2015 North of Svalbard. *Journal of Geophysical Research: Oceans*, 123(2):1156–1176.
- Rösel, A. and Polashenski, C. M., Liston, G. E., King, J. A., Nicolaus, M., Gallet, J.-C., Divine, D., Itkin, P., Spreen, G., Ervik, A., Espeseth, M., Gierisch, A., Haapala, J., Maaß, N., Oikkonen, A., Orsi, A., Shestov, A., Wang, C., Gerland, S., and Granskog, M. A. (2016). N-ICE2015 snow depth data with Magnaprobe.

- Rosenkranz, P. W. (2015). A model for the complex dielectric constant of supercooled liquid water at microwave frequencies. *IEEE Transactions on Geoscience and Remote Sensing*, 53(3):1387–1393.
- Rostosky, P., Melsheimer, C., and Spreen, G. (2019a). AMSR-2 winter snow depth on Arctic sea ice, Version 1.0 (NetCDF) (2012 to 2018).
- Rostosky, P., Melsheimer, C., and Spreen, G. (2019b). AMSR-E winter snow depth on Arctic sea ice, Version 1.0 (NetCDF) (2002 to 2011).
- Rostosky, P., Spreen, G., Farrell, S. L., Frost, T., Heygster, G., and Melsheimer, C. (2018). Snow Depth Retrieval on Arctic Sea Ice From Passive Microwave Radiometers—Improvements and Extensions to Multiyear Ice Using Lower Frequencies. *Journal of Geophysical Research: Oceans*, 123(10):7120–7138.
- Rostosky, P., Spreen, G., Gerland, S., Huntemann, M., and Mech, M. (2020). Modeling the Microwave Emission of Snow on Arctic Sea Ice for Estimating the Uncertainty of Satellite Retrievals. *Journal of Geophysical Research: Oceans*, 125(3).
- Serreze, M. C., Barret, A. P., Stroeve, J. C., Kindig, D. N., and Holland, M. M. (2009). The emergence of surface-based Arctic amplification. *The Cryosphere*, 3(1):11–19.
- Serreze, M. C. and Barry, R. G. (2011). Processes and impacts of Arctic amplification: A research synthesis. *Global and Planetary Change*, 77(1-2):85–96.
- Shi, H., Sohn, B.-J., Dybkjær, G., Tonboe, R. T., and Lee, S.-M. (2020). Simultaneous estimation of wintertime sea ice thickness and snow depth from space-borne freeboard measurements. *The Cryosphere Discussions*, 2020:1–31.
- Shokr, M. E. and Sinha, N. K. (1999). Arctic sea ice microstructure observations relevant to microwave scattering. *Arctic*, 47(3):265–279.
- Sommerfeld, R. A. and LaChapelle, E. (1970). The classification of snow metamorphism. *J. Glaciol.*, 9(55):3–17.
- Spreen, G., Kaleschke, L., and Heygster, G. (2008). Sea ice remote sensing using AMSR-E 89 GHz channels. *Journal of Geophysical Research*, 113(C02S03):11–19.
- Stiles, W. H. and Ulaby, F. T. (1980). The Active and Passive Microwave Response to Snow Parameters 1. Wetness. *Journal of Geophysical Research*, 85(C2):1037–1044.
- Stogryn, A. (1987). An analysis of the tensor dielectric constant of sea ice at microwave frequencies. *IEEE Transactions on Geoscience and Remote Sensing*, 25(2):147–158.
- Stroeve, J. C., Markus, T., Maslanik, J. A., Gasiewski, A. J., Heinrichs, J. F., Holgem, J., and et al. (2006). Impact of surface roughness on AMSR-E sea ice products. *IEEE Transactions on Geoscience and Remote Sensing*, 44(11):3103–3117.
- Sturm, M., Holmgren, J., and Perovich, D. K. (2002). Winter snow cover on the sea ice of the arctic ocean at the surface heat budget of the arctic ocean (SHEBA): Temporal evolution and spatial variability. *Journal of Geophysical Research.*, 107(C10).

- Sturm, M. and Stroeve, J. (2009). AMSRice03 Snow Depth Data, Version 1. accessed: 10 December 2019.
- Tonboe, R. T. (2005). A mass and thermodynamic model for sea ice. *Danish Meteorological Institute Scientific Report.*, pages 5–10.
- Tonboe, R. T., Heygster, G., Pedersen, L. T., and Andersen, S. (2006). Sea ice emission modelling. In Mätzler, C., editor, *Thermal Microwave Radiation: Applications for Remote Sensing*, volume 52, pages 382–425. IEE Electromagnetic Waves Series, London, UK.
- Trodahl, H. J., Wilkinson, S. O. F., McGuinness, M. J., and Haskell, T. G. (2001). Thermal conductivity of sea ice; dependence on temperature and depth. *Geophysical Research Letters*, 28(7):1279–1282.
- Turner, D. D., Cadeddu, M. P., Lohnert, U., Crewell, S., and Vogelmann, A. M. (2009). Modifications to the water vapor continuum in the microwave suggested by ground-based 150-ghz observations. *IEEE Transactions on Geoscience and Remote Sensing*, 47(10):3326–3337.
- Turner, J., Bracegirdle, T. J., Phillips, T., Marshall, G. J., and Hosking, J. S. (2013). An Initial Assessment of Antarctic Sea Ice Extent in the CMIP5 Models. *Journal of Climate*, 26(5):1473–1484.
- Turner, K., M., A., Baadshaug, O., Clark, A., Alexeev, V., Doulgeris, A., Eicken, H., Gong, M., Jensen, D., Kjellman, S., Krivova, M., Lohse, J., Mahoney, A., Miller, K., M. B., Ochwat, N., Olsen, I., Quigley, C., a. R. R., Shates, J., and St. Germain, S. (2017). unpublished field observations. *INTPART Arctic Field Summer Schools: Norway-Canada-USA*.
- Ulaby, F. and Long, D. G. (2014a). *Microwave Remote Sensing.*, volume 1. University of Michigan Press, Ann Arbor, Michigan.
- Ulaby, F. and Long, D. G. (2014b). *Microwave Remote Sensing.*, volume 3. University of Michigan Press, Ann Arbor, Michigan.
- Wang, D., Prigent, C., Kilic, L., Fox, S., Harlow, C., Jimenez, C., Aires, F., Grassotti, C., and Karbou, F. (2017). Surface Emissivity at Microwaves to Millimeter Waves over Polar Regions: Parameterization and Evaluation with Aircraft Experiments. *Journal of Atmospheric and Oceanic Technology*, 34(5):1039–1059.
- Warren, S. G., Rigor, I. G., Untersteiner, N., Radionov, V. F., Bryazgin, N. N., Aleksandrov, Y. I., and et al. (1999). Snow depth on arctic sea ice. *Journal of Climate*, 12(6):1814–1829.
- Webster, M., Gerland, S., Holland, M., Hunke, E., Kwok, R., Lecomte, O., Massom, R., Perovich, D., and Sturm, M. (2018). Snow in the changing sea-ice systems. *Nature Climate Change*, 8:946–953.
- Webster, M. A., Rigor, I. G., Nghiem, S. V., Kurtz, N. T., Farrell, S. L., Perovich, D. K., and Sturm, M. (2014). Interdecadal changes in snow depth on Arctic sea ice. *Journal of Geophysical Research: Oceans*, 119(8):5395–5406.

- Wever, N., Rossmann, L., Maaß, N., Leonard, K. C., Kaleschke, L., Nicolaus, M., and Lehning, M. (2019). Version 1 of a sea ice module for the physics based, detailed, multi-layer SNOWPACK model. *Geosci. Model Dev. Discuss.*, 2019:1–30.
- Wiesmann, A. and Mätzler, C. (1999). Microwave emission model of layered snow packs. *Remote Sens. Environ.*, 123(3):307–316.
- Wiesmann, A., Mätzler, C., and Weise, T. (1998). Radiometric and structural measurements of snow samples. *Radio Science*, 33(2):273–289.
- Willmes, S., Nicolaus, M., and Haas, C. (2014). The microwave emissivity variability of snow covered first-year sea ice from late winter to early summer: A model study. *The Cryosphere*, 8(3):891–904.
- Worby, A. P., Markus, T., Steer, A. D., Lytle, V. I., and Massom, R. A. (2008). Evaluation of the AMSR-E snow depth product over east Antarctic sea ice using in situ measurements and aerial photography. *Journal of Geophysical Research*, 11(C05S94):2892–2905.
- Yackel, J., Geldsetzer, T., Mahmud, M., Nandan, V., Howell, S. E. L., Scharien, R. K., and Lam, H. M. (2019). Snow Thickness Estimation on First-Year Sea Ice from Late Winter Spaceborne Scatterometer Backscatter Variance. *Remote Sensing*, 11(4).
- Yan, J.-B., Gogineni, S., Rodriguez-Morales, F., Gomez-Garcia, D., Paden, J., Li, J., and et al. (2017). Airborne measurements of snow thickness: Using ultrawide-band frequency-modulated-continuous-wave radars. *IEEE Geoscience and Remote Sensing Magazine*, 5(2):57–76.
- Ye, Y., Shokr, M., Heygster, G., and Spreen, G. (2016). Improving Multiyear Sea Ice Concentration Estimates with Sea Ice Drift. *Remote Sensing*, 8(5).
- Zhou, L., Stroeve, J., Xu, S., Petty, A., Tilling, R., Winstrup, M., Rostosky, P., Lawrence, I. R., Liston, G. E., Ridout, A., Tsamados, M., and Nandan, V. (2020). Inter-comparison of snow depth over sea ice from multiple methods. *The Cryosphere Discussions*, 2020:1–35.
- Zhou, L., Xu, S., Liu, J., and Wang, B. (2018). On the retrieval of sea ice thickness and snow depth using concurrent laser altimetry and L-band remote sensing data. *The Cryosphere*, 12(3):993–1012.

Appendix A

Gaussian Error Propagation

In This Chapter the Gaussian Error propagation model is derived which is used to asses an early uncertainty estimation for the snow depth retrieval derived in chapter 3. This model was already published in Rostosky et al. (2018) and was originally developed by T. Frost. The Gaussian Error Propagation is a common method to estimated the uncertainty of a model based on the uncertainties of the contributing parameters. The snow depth retrieval equation has the form $Sd = a + b * GR$ (see equation 3.1). GR is the gradient ratio of the vertically polarised brightness temperature at 18.7 GHz and 6.9 GHz. The following parameters contribute to the derived snow depth and have to be considered: The brightness temperature T_b at frequency ν_1 (= 18.7 GHz) and ν_2 (= 6.9 GHz) and the corresponding open water tie points k . The uncertainty of the observed brightness temperatures at these frequencies is estimated to 0.5 K. The last quantity that contributes to GR is the sea ice concentration C . The algorithm is limited to $C = 80\%$ in order to minimise its influence. In this case, the uncertainty of C is estimated to be 5%. To calculate the uncertainty a Gaussian error propagation model is used following Spreen et al. (2008). First, the uncertainty of vertically polarised GR corrected for the sea ice concentration is derived. The partial derivatives of GR with respect to the variables Tb_{ν_i} , k_i and C are given by:

$$\sigma_{k1} = \sigma_{k2} = \pm \sigma_{Tb_{\nu_1,ow}}^2 \quad (A.1)$$

$$G_1 = \frac{\partial GR}{\partial Tb_{\nu_1}} = \frac{2 * Tb_{\nu_2} + (k_1 - k_2) * (1 - C)}{(Tb_{\nu_1} + Tb_{\nu_2} - (1 - C) * k_2)^2} \quad (A.2)$$

$$G_2 = \frac{\partial GR}{\partial Tb_{\nu_2}} = \frac{2 * Tb_{\nu_1} + (k_1 - k_2) * (1 - C)}{(Tb_{\nu_1} + Tb_{\nu_2} - (1 - C) * k_2)^2} \quad (A.3)$$

$$G_3 = \frac{\partial GR}{\partial k_1} = \frac{(1-C)}{(Tb_{v1} + Tb_{v2} - (1-C) * k_2)} \quad (A.4)$$

$$G_4 = \frac{\partial GR}{\partial k_2} = \frac{(1-C) * (Tb_{v1} - Tb_{v2} - k_1 * (1-C))}{(Tb_{v1} + Tb_{v2} - (1-C) * k_2)^2} \quad (A.5)$$

$$G_5 = \frac{\partial GR}{\partial C} = \frac{(k_1 - k_2) * Tb_{v1} + (k_1 + k_2) * Tb_{v2}}{(Tb_{v1} + Tb_{v2} - (1-C) * k_2)^2} \quad (A.6)$$

From these equations, the uncertainty of GR is calculated as follows:

$$\sigma_{GR} = \sqrt{G_1^2 * \sigma_{Tb_{v1}}^2 + G_2^2 * \sigma_{Tb_{v2}}^2 + G_3^2 * \sigma_{k_1}^2 + G_4^2 * \sigma_{k_2}^2 + G_5^2 * \sigma_C^2} \quad (A.7)$$

The error propagation for the snow depth retrieval can be calculated from:

$$\frac{\partial Sd}{\partial a} = 1 \quad (A.8)$$

$$\frac{\partial Sd}{\partial b} = GR \quad (A.9)$$

$$\frac{\partial Sd}{\partial GR} = b \quad (A.10)$$

And finally the uncertainty of the snow depth (Sd) can be calculated from:

$$Sd = \sqrt{\sigma_a^2 + GR^2 * \sigma_b^2 + b * 2\sigma_{GR}^2} \quad (A.11)$$

Appendix B

N-ICE2015 Snow Pit Data

The snow pit data used in chapter 4 can be downloaded from the Norwegian Polar Datacentre (doi: 10.21334/npolar.2017.d2be5f05, accessed 02 November 2017). In Table B.1, all selected snow pits used in chapter 4 are listed.

Table B.1: Date, latitude, longitude and number of the N-ICE2015 snow pit data. In addition, the air temperature (T) during the snow pit measurements is given.

Date in 2015	Latitude °N	Longitude °E	Number	T (°C)
20 January	83.15	20.07	1	−21.8
23 January	83.10	20.67	2	−33
23 January	83.10	20.68	3	−32.9
28 January	83.07	17.95	4	−28.8
28 January	83.06	19.95	5	−26.9
28 January	83.06	17.95	6	−28.3
03 February	83.08	16.48	7	−9
03 February	83.09	16.53	8	−10.7
13 February	81.95	19.70	10	−30.2
27 February	82.92	26.55	1	−34.2
02 March	82.97	25.90	2	−21.5
05 March	83.13	24.15	3	−6.7
07 March	83.15	23.85	4	−3.6
08 March	83.19	23.23	5	−2.8
09 March	83.17	22.06	6	−2.9
09 March	83.17	22.06	7	−3.3
10 March	83.11	21.69	8	N/A
11 March	83.02	21.32	9	N/A

13 March	82.88	21.28	10	N/A
13 March	82.86	21.23	11	N/A
18 March	82.61	22.78	12	N/A
19 April	83.11	14.25	1	-14.5
27 April	82.25	14.47	3	-11.8
27 April	82.24	14.40	4	-12.75
13 May	81.38	9.09	14	N/A
13 May	81.37	9.06	15	N/A
31 May	80.69	6.40	32	N/A
31 May	80.69	6.93	33	N/A

Below, the full input snow profiles which were used for the simulations with MEMLS and SNOWPACK in chapter 4 are given.

Table B.2 to Table B.29 show the 28 snow profiles used for the MEMLS simulations, derived from the N-ICE2015 snow pit measurements (Merkouriadi et al., 2017b). In order to avoid incoherent effects in the model, observed layers with less than 2 cm thickness are merged to the next lower layer. The exponential correlation length was estimated from Table 1 in Mätzler (2002) using the grain type, grain size and snow density measurements. For all MEMLS simulations, an incident angle of 55° and an ocean salinity of 34 ppt was used. The automatic averaging of coherent layers was disabled in the Model. Instead, coherent layers were avoided by using a minimum layer thickness of 2 cm.

Table B.2: N-ICE2015 snow pit properties for the snow pit from 20 January 2015, number 1. N is the layer number (N = 1 is the top layer), ρ the snow density, T the snow temperature and e_{corr} the exponential correlation length. In MEMLS, it is distinguished between normal snow (snow type =1) and depth hoar (snow type =2).

N	ρ (kg/m ³)	T (°C)	e_{corr}	layer depth (cm)	snow type
5	326	-9.85	0.218	9	2
4	312	-10.07	0.156	10	1
3	306	-12.40	0.161	8	1
2	214	-14.35	0.0899	10	1
1	107	-18.84	0.0345	6	1

Table B.3: Same as Table B.2 but for the snow pit from 23 January 2015, number 2.

N	T ρ (kg/m ³)	(°C)	e_{corr}	layer depth (cm)	snow type
4	263	-8.45	0.218	13	2
3	273	-12.28	0.218	13	2
2	307	-17.78	0.087	11	1
1	307	-26.40	0.085	11	1

Table B.4: Same as Table B.2 but for the snow pit from 23 January 2015, number 3.

N	T ρ (kg/m ³)	(°C)	e_{corr}	layer depth (cm)	snow type
4	399	-8.25	0.22	18	2
3	329	-13.05	0.218	21	2
2	275	-21.16	0.085	11	1
1	260	-29.5	0.085	5	1

Table B.5: Same as Table B.2 but for the snow pit from 28 January 2015, number 4.

N	T ρ (kg/m ³)	(°C)	e_{corr}	layer depth (cm)	snow type
3	314	-12.05	0.22	5	2
2	290	-15.5	0.137	5	1
1	248	-23	0.071	11	1

Table B.6: Same as Table B.2 but for the snow pit from 28 January 2015, number 5.

N	T ρ (kg/m ³)	(°C)	e_{corr}	layer depth (cm)	snow type
5	309	-12.23	0.218	9	2
4	315	-17.35	0.156	9	1
3	301	-21.12	0.137	8	1
2	279	-24.0	0.087	4	1
1	244	-27.9	0.04	6	1

Table B.7: Same as Table B.2 but for the snow pit from 28 January 2015, number 6.

N	T	ρ (kg/m ³)	(°C)	e_{corr}	layer depth (cm)	snow type
5		372	−8.8	0.138	16	1
4		333	−12.3	0.138	10	1
3		338	−15.9	0.135	10	1
2		325	−18.6	0.057	6	1
1		256	−24.8	0.052	11	1

Table B.8: Same as Table B.2 but for the snow pit from 03 February 2015, number 7.

N	T	ρ (kg/m ³)	(°C)	e_{corr}	layer depth (cm)	snow type
3		306	−11.8	0.327	6	2
2		299	−12.1	0.158	9	1
1		253	−11.4	0.137	6	1

Table B.9: Same as Table B.2 but for the snow pit from 03 February 2015, number 8.

N	T	ρ (kg/m ³)	(°C)	e_{corr}	layer depth (cm)	snow type
4		342	−8.7	0.327	18	2
3		296	−11	0.137	19	1
2		221	−12.6	0.137	14	1
1		153	−12.6	0.0345	4	1

Table B.10: Same as Table B.2 but for the snow pit from 13 February 2015, number 10.

N	T	ρ (kg/m ³)	(°C)	e_{corr}	layer depth (cm)	snow type
3		328	−11	0.135	8	1
2		343	−12.6	0.07	11	1
1		385	−12.6	0.09	20	1

Table B.11: Same as Table B.2 but for the snow pit from 27 February 2015, number 1.

N	T ρ (kg/m ³)	(°C)	e_{corr}	layer depth (cm)	snow type
7	360	-11.6	0.178	5	1
6	358	-12.3	0.178	5	1
5	353	-13.6	0.178	2	1
4	340	-15.3	0.09	5	1
3	310	-17.9	0.178	4	1
2	280	-19.3	0.178	2	1
1	261	-23.1	0.071	5	1

Table B.12: Same as Table B.2 but for the snow pit from 02 March 2015, number 2.

N	T ρ (kg/m ³)	(°C)	e_{corr}	layer depth (cm)	snow type
5	264	-19.6	0.195	7	1
4	329	-19.9	0.161	4	1
3	391	-20.0	0.161	4	1
2	468	-21.1	0.161	5	1
1	478	-21.4	0.156	3	1

Table B.13: Same as Table B.2 but for the snow pit from 05 March 2015, number 3.

N	T ρ (kg/m ³)	(°C)	e_{corr}	layer depth (cm)	snow type
9	460	-7.1	0.218	5	2
8	425	-7.15	0.103	5	1
7	430	-7.2	0.113	5	1
6	445	-7.15	0.1	5	1
5	385	-7.1	0.135	5	1
4	333	-7.2	0.22	5	2
3	358	-7.4	0.135	5	1
2	390	-7.7	0.102	5	1
1	380	-7.8	0.12	2	1

Table B.14: Same as Table B.2 but for the snow pit from 07 March 2015, number 4.

N	T ρ (kg/m ³)	(°C)	e_{corr}	layer depth (cm)	snow type
11	355	-6.1	0.195	6	1
10	328	-6.5	0.219	5	2
9	344	-6.6	0.135	7	2
8	359	-6.8	0.135	3	1
7	350	-7.0	0.114	5	1
6	352	-7.0	0.131	2	1
5	358	-7.0	0.131	4	1
4	355	-6.8	0.121	5	2
3	353	-6.4	0.121	5	1
2	348	-5.9	0.135	2	1
1	303	-5.7	0.089	3	1

Table B.15: Same as Table B.2 but for the snow pit from 08 March 2015, number 5.

N	T ρ (kg/m ³)	(°C)	e_{corr}	layer depth (cm)	snow type
12	452	-5.5	0.183	6	1
11	424	-5.8	0.201	5	1
10	362	-5.9	0.201	5	2
9	344	-5.9	0.201	5	2
8	373	-5.9	0.201	5	1
7	419	-5.9	0.135	2	1
6	437	-5.8	0.220	3	1
5	434	-5.8	0.178	4	1
4	417	-5.6	0.178	5	2
3	395	-5.4	0.156	5	1
2	377	-5.1	0.089	2	1
1	354	-4.6	0.104	3	1

Table B.16: Same as Table B.2 but for the snow pit from 09 March 2015, number 6.

N	T ρ (kg/m ³)	(°C)	e_{corr}	layer depth (cm)	snow type
7	325	-4.7	0.126	6	1
6	322	-4.5	0.135	5	1
5	324	-4.3	0.218	5	1
4	355	-4.0	0.069	5	1
3	384	-3.8	0.069	5	1
2	401	-3.8	0.069	4	1
1	374	-3.7	0.071	4	1

Table B.17: Same as Table B.2 but for the snow pit from 09 march 2015, number 7.

N	T ρ (kg/m ³)	(°C)	e_{corr}	layer depth (cm)	snow type
10	374	-5.0	0.052	4	1
9	422	-5.3	0.056	2	1
8	399	-5.2	0.056	5	1
7	385	-5.0	0.156	5	1
6	401	-4.8	0.219	5	2
5	426	-4.6	0.219	5	2
4	393	-4.5	0.219	3	2
3	365	-4.3	0.118	2	1
2	328	-4.3	0.121	2	1
1	201	-3.9	0.043	4	1

Table B.18: Same as Table B.2 but for the snow pit from 10 March 2015, number 8.

N	T ρ (kg/m ³)	(°C)	e_{corr}	layer depth (cm)	snow type
12	380	-5.6	0.158	5	1
11	387	-5.6	0.158	5	1
10	397	-5.5	0.158	5	1
9	400	-5.5	0.158	3	1
8	391	-5.5	0.158	4	1
7	336	-5.4	0.178	5	1
6	330	-5.4	0.135	3	1
5	373	-5.4	0.135	5	1
4	386	-5.4	0.137	5	1
3	400	-5.4	0.056	2	1
2	363	-5.5	0.056	3	1
1	126	-5.0	0.036	4	1

Table B.19: Same as Table B.2 but for the snow pit from 11 March 2015, number 9.

N	T ρ (kg/m ³)	(°C)	e_{corr}	layer depth (cm)	snow type
13	366	-6.9	0.138	6	1
12	388	-5.4	0.135	5	1
11	390	-5.6	0.135	4	1
10	377	-7.0	0.135	6	1
9	396	-7.4	0.135	4	1
8	429	-8.7	0.135	5	1
7	420	-9.2	0.135	7	1
6	360	-10.0	0.135	2	1
5	260	-10.4	0.08	3	1
4	300	-11.1	0.053	2	1
3	232	-14.4	0.0345	3	1
2	278	-13.5	0.161	2	1
1	332	-14.6	0.161	2	1

Table B.20: Same as Table B.2 but for the snow pit from 13 March 2015, number 10.

N	T ρ (kg/m ³)	(°C)	e_{corr}	layer depth (cm)	snow type
13	374	-9.7	0.053	6	1
12	362	-7.9	0.056	5	1
11	358	-9.6	0.056	4	1
10	394	-11.4	0.137	6	1
9	406	-12.2	0.137	4	1
8	402	-12.9	0.178	5	1
7	398	-14.3	0.137	7	1
6	389	-15.3	0.137	2	1
5	391	-16.4	0.137	3	1
4	355	-18.1	0.158	2	1
3	265	-19.6	0.158	3	1
2	213	-20.8	0.158	2	1
1	203	-22.4	0.042	2	1

Table B.21: Same as Table B.2 but for the snow pit from 13 March 2015, number 11.

N	T ρ (kg/m ³)	(°C)	e_{corr}	layer depth (cm)	snow type
15	388	-8.4	0.194	7	1
14	385	-6.3	0.220	4	2
13	370	-7.8	0.220	5	2
12	383	-9.5	0.220	3	2
11	407	-11.2	0.218	7	2
10	413	-12.2	0.218	3	2
9	392	-12.3	0.135	7	1
8	377	-14.0	0.135	3	1
7	374	-16.0	0.137	7	1
6	375	-18.1	0.137	3	1
5	379	-20.2	0.137	2	1
4	385	-22.1	0.137	5	1
3	383	-23.6	0.138	2	1
2	380	-24.8	0.138	3	1
1	329	-25.5	0.053	3	1

Table B.22: Same as Table B.2 but for the snow pit from 18 March 2015, number 12.

N	T ρ (kg/m ³)	(°C)	e_{corr}	layer depth (cm)	snow type
12	382	-10.3	0.137	6	1
11	404	-7.5	0.158	6	2
10	383	-8.3	0.218	4	2
9	351	-9.7	0.218	5	2
8	325	-12.3	0.218	10	2
7	323	-14.8	0.218	5	2
6	336	-15.9	0.218	4	2
5	351	-17.7	0.158	6	1
4	313	-19.9	0.158	5	1
3	247	-21.6	0.158	2	1
2	211	-23.7	0.126	3	1
1	223	-26.0	0.042	2	1

Table B.23: Same as Table B.2 but for the snow pit from 19 April 2015, number 1.

N	T ρ (kg/m ³)	(°C)	e_{corr}	layer depth (cm)	snow type
6	530	-7.2	0.161	16	1
5	312	-9.9	0.158	23	1
4	297	-13.3	0.057	5	1
3	280	-14.6	0.057	3	1
2	329	-15.2	0.085	7	1
1	370	-15.7	0.057	4	1

Table B.24: Same as Table B.2 but for the snow pit from 27 April 2015, number 3.

N	T ρ (kg/m ³)	(°C)	e_{corr}	layer depth (cm)	snow type
6	360	-3.5	0.056	15	1
5	327	-4.7	0.212	12	2
4	277	-6.1	0.137	6	1
3	269	-7.5	0.056	7	1
2	279	-12.1	0.043	5	1
1	280	-14.5	0.045	2	1

Table B.25: Same as Table B.2 but for the snow pit from 27 April 2015, number 4.

N	T ρ (kg/m ³)	(°C)	e_{corr}	layer depth (cm)	snow type
4	230	−6.5	0.209	6	2
3	310	−7.6	0.045	7	1
2	310	−10.0	0.045	5	1
1	230	−11.4	0.056	2	1

Table B.26: Same as Table B.2 but for the snow pit from 13 May 2015, number 14.

N	T ρ (kg/m ³)	(°C)	e_{corr}	layer depth (cm)	snow type
17	250	−3.9	0.218	4	2
16	246	−4.2	0.218	6	2
15	237	−4.8	0.218	5	2
14	264	−5.5	0.158	5	1
13	329	−6.1	0.135	4	1
12	370	−6.8	0.122	6	1
11	347	−6.9	0.122	2	1
10	319	−7.4	0.122	3	1
9	327	−7.6	0.132	5	1
8	365	−7.9	0.135	5	1
7	392	−8.3	0.135	5	1
6	393	−8.6	0.158	5	1
5	352	−8.8	0.161	5	1
4	314	−8.9	0.135	5	1
3	323	−9.0	0.135	4	1
2	343	−9.0	0.158	2	1
1	350	−9.3	0.179	2	1

Table B.27: Same as Table B.2 but for the snow pit from 13 May 2015, number 15.

N	T ρ (kg/m ³)	(°C)	e_{corr}	layer depth (cm)	snow type
7	273	-6.5	0.202	4	2
6	260	-6.2	0.218	5	2
5	296	-6.5	0.218	5	2
4	285	-6.4	0.218	4	2
3	266	-6.8	0.218	5	2
2	294	-7.1	0.140	5	1
1	339	-7.7	0.218	5	2

Table B.28: Same as Table B.2 but for the snow pit from 31 May 2015, number 31.

N	T ρ (kg/m ³)	(°C)	e_{corr}	layer depth (cm)	snow type
8	251	-2.8	0.136	10	1
7	265	-2.6	0.137	10	1
6	316	-2.5	0.137	8	1
5	361	-2.2	0.135	2	1
4	385	-2.0	0.135	10	1
3	390	-1.8	0.220	2	2
2	348	-1.8	0.090	5	1
1	308	-1.7	0.057	3	1

Table B.29: Same as Table B.2 but for the snow pit from 31 May 2015, number 32.

N	T ρ (kg/m ³)	(°C)	e_{corr}	layer depth (cm)	snow type
7	250	-3.3	0.218	10	2
6	289	-3.2	0.218	7	2
5	328	-2.5	0.135	3	1
4	313	-2.5	0.137	2	1
3	237	-1.5	0.071	8	1
2	163	-1.5	0.055	2	1
1	140	-1.5	0.035	2	1

Table B.30 shows the initialization snow profile for the SNOWPACK simulation performed in chapter 4, derived from table B.3. The values for bond radius (RB) are estimated from a lookup table (see: <https://models.slf.ch/p/snowpack/page/Starting-from-profiles/>, accessed

15 December 2018). The denticity (DD) and sphericity (SP) are estimated from figure 8 in Lehning et al. (2002b). The model was initialized using the recommended options. The internal model timestep was set to 0.1 minutes and the Richards water transport model was used. The ocean heat flux was set to $3 \frac{W}{m}$.

Table B.30: Initialisation snow- and ice profile for the SNOWPACK model. Given are the layer thickness (L), the temperature (T), the volume fraction of ice (VI), the volume fraction of void (VV), the grain radius (RG), the bond radius (RB), the denticity (DD), the sphericity (SP), the number of elements within one layer (NE) and the salinity (S).

L (m)	T (K)	VI	VV	RG (m)	RB	DD	SP	N	S (ppt)
0.15	285.0	0.9	0.1	5	2.5	1	0	30	6
0.15	284.8	0.92	0.08	5	2.5	1	0	30	6
0.15	282.7	0.94	0.06	5	2.5	1	0	30	6
0.15	278.5	0.95	0.05	5	2.5	1	0	30	5.0
0.15	275.0	0.95	0.05	5	2.5	1	0	30	4.1
0.15	272.0	0.95	0.05	5	2.5	1	0	30	3.3
0.15	269.0	0.95	0.05	5	2.5	1	0	30	2.6
0.15	267.0	0.95	0.05	5	2.5	1	0	30	2
0.02	266.0	0.95	0.05	5	2.5	1	0	30	1.3
0.02	265.0	0.95	0.05	5	2.5	1	0	30	1.1
0.02	264.0	0.95	0.05	5	2.5	1	0	30	1
0.11	262.7	0.287	0.713	1.2	1.0	0.1	0.1	10	0
0.11	258.4	0.297	0.703	0.8	1.0	0.1	0.1	10	0
0.13	254.4	0.335	0.665	0.3	0.075	0.5	0.5	10	0
0.13	245.8	0.335	0.665	0.3	0.075	1	0.4	10	0

Appendix C

SNOWPACK Initialisation Files

Table C.1 to table C.3 show the full initialisation profiles for the SNOWPACK simulations in chapter 5 for the Barents Sea (Table 5.2), the Labradors Sea (Table C.2) and Central Arctic (Table C.3). More details about the parameters used in initialisation of the SNOWPACK model can be found in chapter 4 and in the model documentation (<https://models.slf.ch/docserver/snowpack/html/index.html>, accessed 18 December 2019). The sea ice version of SNOWPACK is not in the official release of the SNOWPACK cohort (status December 2019) but details about the initialisation of this model version can be found in the supporting information provided in Wever et al. (2019).

Table C.1: Initialisation parameters for the SNOWPACK simulation in the Barents Sea. Shown are the Layer depth D_{layer} (m), the temperature (K), the fraction of pure ice I_{frac} and void I_{frac} , the grain size (mm), the bond radius (mm), the dendricity and sphericity of each layer of the snow-ice system. The marker is a measure for previous snow metamorphism. N_e sets the number of elements each layer is split in the initialisation. The last column is the salinity (ppt).

D_{layer}	temperature	I_{frac}	V_{frac}	grain size	bond radius	dendricity	sphericity	marker	N_e	salinity
0.2	269.0	0.95	0.05	3.0	2.0	1.0	0.0	7	50	6.0
0.02	267.0	0.95	0.05	3.0	2.0	1.0	0.0	7	1	5.4
0.02	266.8	0.95	0.05	3.0	2.0	1.0	0.0	7	1	5.0
0.02	266.0	0.95	0.05	3.0	2.0	1.0	0.0	7	1	4.0
0.02	265.0	0.95	0.05	3.0	2.0	1.0	0.0	7	1	5.0
0.02	264.0	0.95	0.05	3.0	2.0	1.0	0.0	7	1	6.0
0.04	263.0	0.29	0.71	1.2	1.0	0.1	0.1	1	10	0.0
0.03	261.0	0.34	0.66	0.3	0.075	1.0	0.4	0	10	0.0

Table C.2: Same as Table C.1 but for Labrador Sea.

D_{layer}	temperature	I_{frac}	V_{frac}	grain size	bond radius	dendricity	sphericity	marker	N_e	salinity
0.1	269.0	0.95	0.05	3.0	2.0	1.0	0	7	50	6.0
0.02	267.0	0.95	0.05	3.0	2.0	1.0	0	7	1	5.4
0.02	266.8	0.95	0.05	3.0	2.0	1.0	0	7	1	5.0
0.02	266.0	0.95	0.05	3.0	2.0	1.0	0	7	1	4.0
0.02	265.0	0.95	0.05	3.0	2.0	1.0	0	7	1	5.0
0.02	264.0	0.95	0.05	3.0	2.0	1.0	0	7	1	6.0
0.10	263.0	0.29	0.71	1.2	1.0	0.1	0.1	1	10	0.0
0.05	261.0	0.34	0.66	0.3	0.075	1.0	0.4	0	10	0.0

Table C.3: Same as Table C.1 but for the central Arctic.

D_{layer}	temperature	I_{frac}	V_{frac}	grain size	bond radius	dendricity	sphericity	marker	N_e	salinity
2.8	269.0	0.95	0.05	3.0	2.0	1.0	0.0	7	50	6.0
0.02	265.0	0.95	0.05	3.0	2.0	1.0	0.0	7	1	2.4
0.02	264.0	0.95	0.05	3.0	2.0	1.0	0.0	7	1	1.0
0.02	263.0	0.95	0.05	3.0	2.0	1.0	0.0	7	1	0.8
0.02	262.0	0.95	0.05	3.0	2.0	1.0	0.0	7	1	0.5
0.02	261.0	0.95	0.05	3.0	2.0	1.0	0.0	7	1	0.0
0.25	259.0	0.29	0.71	1.2	1.0	0.1	0.1	1	10	0.0
0.1	256.0	0.34	0.66	0.3	0.075	1.0	0.4	0	10	0.0

Appendix D

Snow Depth Dataset

The new retrieval coefficients derived in chapter 3 and the uncertainty estimations derived in chapter 4 are used to compile a snow depth on Arctic sea ice dataset which is published in the PANAGEA datacenter. The dataset consists of two sub-versions, for the AMSR-E (2002-2011, Rostosky et al., 2019b) and AMSR2 (2012-2018, Rostosky et al., 2019a) measurement periods. In the following chapter, the compilation of the dataset is described. In order to apply the snow depth on Arctic sea ice retrieval, the following data is needed on a daily basis.

Brightness Temperature

The retrieval uses AMSR-E/2 vertical polarised brightness temperature at 6.9 GHz and 18.7 GHz observation on a polar stereographic grid resampled to 25 km x 25 km spatial resolution (Cavaliere et al., 2014; Maeda et al., 2016). More details about the satellite observations are provided in Appendix E.

Sea Ice Concentration

In addition to the brightness temperature, information about the sea ice concentration (SIC) are needed. SIC is used as a flag for the retrieval since is only applied for $SIC \geq 80\%$. If SIC is below 100%, GR(19/7) is corrected for the contribution of open water following Ivanova et al. (2015). Here, the ASI sea ice concentration is used (Spren et al., 2008), which can be downloaded under <https://seaice.uni-bremen.de/databrowser/> (status, 05 February 2020). The product is provided on a polar stereographic grid and has a resolution of 6.25 km x 6.25 km. It is resampled to 25 km x 25 km using the Pyresample Python package (see <https://pyresample.readthedocs.io/en/latest/>, accessed, 05 July 2019).

Sea Ice Type

The retrieval uses a different set of regression coefficients for FYI and MYI. Over MYI, snow depth is only retrieved in March and April. During the rest of the winter season (November to February), the retrieval is only applied if the MYI concentration in a pixel is $\leq 20\%$. In March and April, if the MYI concentration is between 0% and 100%, a linear interpolation between the FYI and MYI retrieval is applied. First the FYI and MYI snow depths are derived assuming 100% FYI and 100% MYI concentration, respectively and then averaged by weighting them with the actual MYI concentration. In principal, a similar technique as used for the correction of the SIC could be applied to correct for the influence of MYI. However, the tiepoints for the different ice types at the microwave frequencies used here have high uncertainties and this leads to large uncertainties in the retrieved snow depth. The interpolation method, however, might not be the most accurate. But given the fact that the differences in the retrieval coefficients over FYI and MYI are small, the error by assuming a linear scaling with the MYI concentration is acceptable.

Melt Filter

The retrieval can only be applied for dry snow conditions. ERA5 reanalysis 2 m air temperature data are used to detect possible melt in the snow. The threshold value is set to 2°C since liquid water is already found in the snow at temperatures above the freezing point (see e.g., figure 5.22). Another possibility could be using a snow melt onset algorithm based on satellite observations as developed by Arndt and Haas (2019) for snow on Antarctic sea ice, which is not implemented yet.

Appendix E

Satellite Data

The satellite data used in for this work are the resampled and regridded passive microwave satellite observations from the AMSR-E and AMSR2 sensors (Cavalieri et al., 2014; Maeda et al., 2016) deployed at the satellite missions Aqua (AMSR-E) and GCOM-W1 (AMSR2). The AMSR-E dataset used in this study is the AMSR-E/2 brightness temperatures, resampled to a polar grid are used (Cavalieri and Comiso., 2014a,b). The instrument descriptions of AMSR-E and AMSR2 sensor are given in Table E.1 and Table E.2. Both instruments are conical scanning systems rotating with 40 rpm. The AMSR-E scanner measures at 6 frequencies from 6.925 GHz to 89 GHz at horizontal and vertical polarisation. The AMSR2 scanner measures in addition at 7.3 GHz. Although both sensors are using the same setup, their observations have to be inter-calibrated to guarantee consistent timeseries. In this study, the AMSR2 observations are inter-calibrated using the coefficients derived by Du et al. (2014). However, the inter-calibrations was performed in tropical regions over rain forest and ocean (Du et al., 2014) and therefore might not be suited for Arctic regions, especially for sea ice with its very high emissivity.

Table E.1: AMSR-E instrument description.

Polarization	Horizontal and Vertical					
Incidence angle	55°					
Swath (km)	1445					
Dynamic Range (K)	2.7 to 340					
Precision (1 σ)	1 K					
Center (GHz)	6.925	10.65	18.7	23.8	36.6	89
Bandwidth (MHz)	350	100	200	400	1000	3000
Sensitivity (K)	0.3	0.6	0.6	0.6	0.6	1.1
IFOV (km)	74 * 43	51 * 30	27 * 16	31 * 18	14 * 8	6 * 4

Table E.2: AMSR2 instrument description.

Polarization	Horizontal and Vertical					
Incidence angle	55°					
Swath (km)	1450					
Dynamic Range (K)	2.7 to 340					
Precision (1 σ)	1 K					
Frequency (GHz)	6.925/7.3	10.65	18.7	23.8	36.5	89
Bandwidth (MHz)	350	100	200	400	1000	3000
Sensitivity (K)	0.3	0.3	0.6	0.6	0.6	1.1
IFOV (km)	35 * 62	35 * 62	24 * 42	15 * 26	7 * 12	3 * 5